



저작자표시-비영리-변경금지 2.0 대한민국

이용자는 아래의 조건을 따르는 경우에 한하여 자유롭게

- 이 저작물을 복제, 배포, 전송, 전시, 공연 및 방송할 수 있습니다.

다음과 같은 조건을 따라야 합니다:



저작자표시. 귀하는 원저작자를 표시하여야 합니다.



비영리. 귀하는 이 저작물을 영리 목적으로 이용할 수 없습니다.



변경금지. 귀하는 이 저작물을 개작, 변형 또는 가공할 수 없습니다.

- 귀하는, 이 저작물의 재이용이나 배포의 경우, 이 저작물에 적용된 이용허락조건을 명확하게 나타내어야 합니다.
- 저작권자로부터 별도의 허가를 받으면 이러한 조건들은 적용되지 않습니다.

저작권법에 따른 이용자의 권리는 위의 내용에 의하여 영향을 받지 않습니다.

이것은 [이용허락규약\(Legal Code\)](#)을 이해하기 쉽게 요약한 것입니다.

[Disclaimer](#)

Doctoral Thesis

Computational Study on  
Polymorphism and Charge Storage Mechanism of  
Battery Materials via Multiscale Simulation

Se Hun Joo

School of Energy and Chemical Engineering  
(Chemical Engineering)

Ulsan National Institute of Science and Technology

2021

Computational Study on  
Polymorphism and Charge Storage Mechanism of  
Battery Materials via Multiscale Simulation

Se Hun Joo

School of Energy and Chemical Engineering  
(Chemical Engineering)

Ulsan National Institute of Science and Technology

# Computational Study on Polymorphism and Charge Storage Mechanism of Battery Materials via Multiscale Simulation

A thesis/dissertation submitted to  
Ulsan National Institute of Science and Technology  
in partial fulfillment of the  
requirements for the degree of  
Doctor of Philosophy

Se Hun Joo

12/10/2020 of submission

Approved by



Advisor

Sang Kyu Kwak




Computational Study on  
Polymorphism and Charge Storage Mechanism of  
Battery Materials via Multiscale Simulation

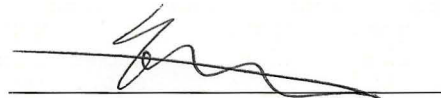
Se Hun Joo

This certifies that the thesis/dissertation of Se Hun Joo is approved.

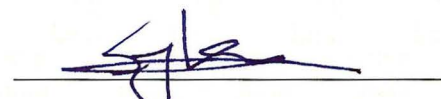
12/10/2020 of submission



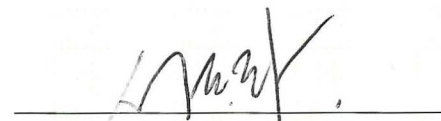
Advisor: Sang Kyu Kwak



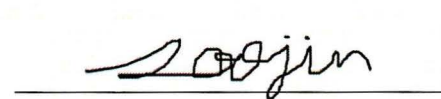
Hyun-Kon Song: Thesis Committee Member #1



Seok Ju Kang: Thesis Committee Member #2



Dong-Hwa Seo: Thesis Committee Member #3



Soojin Park: Thesis Committee Member #4

## Abstract

Rechargeable batteries have attracted a lot of attention owing to their wide applicability, such as portable/consumer electronics, electric vehicles, and grid-scale applications. Over the past two decades, significant advances have been made in battery technologies. However, advancement in various technologies necessitates batteries that are more efficient because the current levels of performance are inadequate. This has encouraged researchers to design and discover new battery materials to meet future demands. In this context, a fundamental understanding of the polymorphism and charge storage mechanism of battery materials can provide design principles and promote the discovery of novel materials. To achieve this, the multiscale simulation method has been used to study physicochemical phenomena or properties of different time and space scales. In this dissertation, we introduced theoretical studies on polymorphism and charge storage mechanism of battery materials. Specifically, we discussed three newly designed electrode materials, a conventional binder material, and a separator material.

In Chapter 1, we provide an overview and the challenges of rechargeable batteries. We then present a general background of the charge storage mechanism and polymorphism phenomenon and their importance in the study and design of rechargeable battery materials. Finally, we describe the modern multiscale computational techniques for rechargeable battery materials such as the density functional theory calculation, density functional tight binding calculation, molecular dynamics simulation, and Monte Carlo simulation.

In Chapter 2, we present a theoretical study on the polymorphism and charge storage mechanism of contorted hexabenzocoronene (c-HBC) as a new type of anode material for Li-ion batteries. In this study, the packing polymorphism was demonstrated by disclosing the crystal structure of polymorph II', which is the metastable  $R\bar{3}$  crystal phase, using computational polymorph prediction. It was also revealed that polymorph II was not a polymorph of c-HBC; instead, it is the  $P3_1$  (or  $P3_2$ ) crystal phase of c-HBC with Pd atoms. Moreover, our investigation on the lithium storage mechanism showed that the c-HBC anode exhibited a single-stage Li-ion insertion behavior without voltage penalty, which was attributed to the 3D-ordered empty pores originating from the contorted structure of c-HBC.

In Chapter 3, we present a theoretical study on the polymorphism and charge storage mechanism of fluorinated-contorted hexabenzocoronene (F-cHBC) as a potential electrochemical organic electrode material. Based on Monte Carlo computational study, it was revealed that the crystal structure of polymorph I was the energetically stable  $P2_1/c$  crystal phase. Furthermore, theoretical investigation on

lithium/sodium storage mechanism showed that Li- and Na-ions could be stored in two distinct sites surrounded by electronegative fluorine atoms and a negatively charged bent edge aromatic ring.

In Chapter 4, we present a theoretical study on the polymorphism and charge storage mechanism of the redox-active covalent triazine framework (rCTF) as a promising organic anode material for Li-ion batteries. The potential energy analysis suggested that the rCTF can potentially exhibit packing polymorphism for two energy-minimum packing modes, namely, AB and slipped-parallel packing modes. The most stable was the slipped-packing mode. Furthermore, we revealed that the rCTF provided a theoretical capacity of up to 1200 mAh g<sup>-1</sup> using quinone, triazine, and benzene rings as the redox-active sites. The structural deformation of rCTF during activation allowed more redox-active sites to be accessible, especially the benzene rings.

In Chapter 5, we present a theoretical study on poly(vinylidene fluoride) (PVDF), which is a conventional polymeric binder material for rechargeable batteries. Although it is rarely considered in the battery field, PVDF is a semicrystalline polymer with various polymorphs that have different polarization characteristics. In this study, the effect of the crystal phases of PVDF, specifically  $\alpha$ - and  $\beta$ -PVDFs, on battery performance was investigated. We showed that compared to negligible polarization of the paraelectric  $\alpha$ -PVDF, the strong polarization generated by the ferroelectric  $\beta$ -PVDF can effectively transport electrons and Li-ions, leading to reduction in the charge transfer resistance and mitigation of the concentration polarization in the Li-ion battery system.

In Chapter 6, we present a theoretical study on polymorphism of chitin separator material and its interaction with electrolyte. As a semicrystalline biopolymer, chitin can exist in two polymorphs,  $\alpha$ - and  $\beta$ -phase. These crystals have different molecular conformation and arrangement, resulting in different polarization characteristics. Based on density functional theory calculations and molecular dynamics simulations, we revealed that both polymorphs of chitin had excellent electrolyte-uptaking property and high physicochemical affinity to Li-ions with binding reversibility.



## Contents

<b>Abstract.....</b>	<b>i</b>
<b>Contents .....</b>	<b>iii</b>
<b>List of Figures.....</b>	<b>vi</b>
<b>List of Tables.....</b>	<b>xix</b>
<b>Chapter 1. Introduction.....</b>	<b>1</b>
1.1 Introduction of Rechargeable Batteries.....	1
1.2 Introduction of Charge Storage Mechanism .....	2
1.2.1 Intercalation Mechanism.....	3
1.2.2 Alloying Mechanism.....	3
1.2.3 Conversion Mechanism.....	4
1.3 Introduction of Polymorphism .....	5
1.3.1 General Introduction of Polymorphism .....	5
1.3.2 Classification of Polymorphism.....	8
1.3.3 Polymorphism in Battery Materials .....	10
1.4 Introduction of Computer Simulation.....	11
1.4.1 Importance of Computer Simulation.....	11
1.4.2 Multiscale Computational Approach.....	12
1.5 References.....	15
<b>Chapter 2. Polymorphism and Lithium Storage Mechanism of Contorted Hexabenzocoronene</b>	
<b>Electrode Material .....</b>	<b>20</b>
2.1 Introduction.....	20
2.2 Computational Methods.....	22
2.2.1 Crystal Structure Prediction.....	22
2.2.2 Monte Carlo Simulation.....	22
2.2.3 Density Functional Theory Calculation .....	23
2.3 Results and Discussion.....	24
2.3.1 Polymorphism of c-HBC .....	24
2.3.2 Lithium Storage Mechanism of c-HBC .....	31
2.4 Conclusion .....	36
2.5 References.....	37
<b>Chapter 3. Polymorphism and Lithium/Sodium Storage Mechanism of Fluorinated-</b>	
<b>Contorted Hexabenzocoronene Electrode Material.....</b>	<b>42</b>

3.1 Introduction.....	42
3.2 Computational Methods.....	44
3.2.1 Crystal Structure Prediction .....	44
3.2.2 Monte Carlo Simulation.....	44
3.2.3 Density Functional Theory Calculation .....	45
3.3 Results and Discussion.....	47
3.3.1 Polymorphism of F-cHBC .....	47
3.3.2 Lithium Storage Mechanism of F-cHBC .....	50
3.3.3 Sodium Storage Mechanism of F-cHBC.....	54
3.4 Conclusion .....	56
3.5 References.....	57
<b>Chapter 4. Polymorphism and Lithium Storage Mechanism of Redox-Active Covalent Triazine Framework Electrode Material .....</b>	<b>61</b>
4.1 Introduction.....	61
4.2 Computational Methods.....	64
4.2.1 Density Functional Tight Binding Calculation .....	64
4.2.2 Density Functional Theory Calculation .....	64
4.2.3 Monte Carlo Simulation.....	65
4.2.4 Lithiation Simulation .....	65
4.3 Results and Discussion.....	66
4.3.1 Packing Polymorphism of rCTF .....	66
4.3.2 Lithium Storage Mechanism of rCTF .....	70
4.3.3 Electronic Structure of rCTF.....	78
4.4 Conclusion .....	80
4.5 References.....	81
<b>Chapter 5. Polymorphism of Poly(vinylidene fluoride) Binder Material .....</b>	<b>88</b>
5.1 Introduction.....	88
5.2 Computational Methods.....	91
5.2.1 Density Functional Theory Calculations.....	91
5.2.2 Molecular Dynamics Simulation.....	92
5.3 Results and Discussion.....	93
5.3.1 Crystal Structure of $\alpha$ - and $\beta$ -PVDF .....	93
5.3.2 Electronic Structure of $\alpha$ - and $\beta$ -PVDF.....	94
5.3.3 Internal Electron Transfer of $\alpha$ - and $\beta$ -PVDF .....	97

5.3.4 Work Function of $\alpha$ - and $\beta$ -PVDF.....	99
5.3.5 Li Binding Affinity of $\alpha$ - and $\beta$ -PVDF.....	100
5.3.6 Polarization Direction of $\beta$ -PVDF on LFP.....	102
5.4 Conclusion .....	104
5.5 References.....	105
<b>Chapter 6. Polymorphism of Chitin Separator Material .....</b>	<b>109</b>
6.1 Introduction.....	109
6.2 Computational Methods.....	111
6.2.1 Density Functional Theory Calculation .....	111
6.2.2 Molecular Dynamics Simulation.....	111
6.3 Results and Discussion.....	113
6.3.1 Polymorphism of Chitin.....	113
6.3.2 Chitin-Electrolyte Interaction.....	116
6.4 Conclusion .....	120
6.5 References.....	121
<b>Chapter 7. Summary and Future Perspectives .....</b>	<b>125</b>
7.1 Summary .....	125
7.2 Future Perspectives .....	127
7.3 References.....	128
<b>Acknowledgements .....</b>	<b>129</b>
<b>List of Publications .....</b>	<b>131</b>

## List of Figures

### Chapter 1

- Figure 1.1** Various applications of rechargeable batteries.
- Figure 1.2** A schematic representation of three typical reaction mechanisms between lithium ion and electrode materials. Reproduced from ref. 17 with permission from The Royal Society of Chemistry, copyright 2015.
- Figure 1.3** Supramolecular assembly evolution of p-aminobenzoic acid (pABA) from a single molecule into crystallites of two different polymorphs. The assembly occurs via two different routes (pink and blue) as a consequence of two different types of crystallisation conditions (X and Y), which leads to different early assembly, polymorphic structure, crystal shapes and material properties. Reproduced from ref. 35 with permission from Springer Nature, copyright 2020.
- Figure 1.4** Number of publications, citations to those and patents related to polymorphism. Landmark contributions are indicated and commented further in the text. Inner graph corresponds to the citations history of the McCrone & Haleblan, *J. Pharm. Sci.*, 1969 review. Reproduced from ref. 36 with permission from The Royal Society of Chemistry, copyright 2015.
- Figure 1.5** Packing polymorphism of benzamide. Form I (top left) with the parallel stacking of hydrogen-bonded dimers, form III (top right) with a herringbone stacking motif and the hypothetical form from the crystal structure prediction (bottom). All structures are composed of identical layers stacked horizontally. The layers highlighted with green carbon atoms have identical orientation, and the layers with purple carbon atoms are rotated by 180°. The two types of layer interfaces are annotated A and B. Reproduced from ref. 41 with permission from American Chemical Society, <https://doi.org/10.1021/acs.cgd.5b01495>, copyright 2016.
- Figure 1.6** Two conformational polymeric forms of the crystalline cadmium(II) coordination trimer with pyridine-4-propanamide (4-propy),  $[\text{Cd}_3\text{Cl}_4(\text{H}_2\text{O})_4(4\text{-propy})_6](\text{CH}_3\text{CH}_2\text{COO})_2$ . A view of the crystal packings of two polymorphic forms with identical building units in Polymorph-I (blue) and differently colored building units of alternating handedness in



Polymorph-II (blue and yellow). Reproduced from ref. 43 with permission from American Chemical Society, copyright 2019.

**Figure 1.7** Various polymorphs of  $\text{MnO}_2$ . Reproduced from ref. 45 with permission from Elsevier Inc., copyright 2019.

**Figure 1.8** Complementary relationship of theory, experiment, and simulation.

**Figure 1.9** Multiscale computational approach for different time and length scales; density functional theory (DFT) calculation, density functional tight binding (DFTB) calculation, molecular dynamics (MD) simulation, Monte Carlo (MC) simulation.

## Chapter 2

- Figure 2.1** (a) Face-on (left) and edge-on (right) chemical structure of c-HBC. The structure of c-HBC exhibits two concave surfaces. (b) Digital photograph of synthesized c-HBC powder. (c) Schematic of proposed Li-ion insertion mechanism in c-HBC. Reproduced from ref. 1 with permission from The Royal Society of Chemistry, copyright 2018.
- Figure 2.2** 1D diffraction traces for the sample series with as-prepared (black line), THF-annealed (red line), and THF-330 °C annealed (blue line) c-HBC films. Significantly decreased peaks at both  $q_1 = 1.04$  and  $q_2 = 1.15 \text{ \AA}^{-1}$  indicate the phase transformation of c-HBC from polymorph II to polymorph II'. Reproduced from ref. 1 with permission from The Royal Society of Chemistry, copyright 2018.
- Figure 2.3** XRD patterns of c-HBC: experimental as-prepared (gray line), THF-330 °C annealed (black line), Rietveld refined (red line), their difference (green line), and the  $R\bar{3}$  crystal phase (blue line). Reproduced from ref. 1 with permission from The Royal Society of Chemistry, copyright 2018.
- Figure 2.4** Projection views of the  $R\bar{3}$  crystal phase along [001] and [100] directions, respectively. For clarity, the c-HBC molecules in different layers are represented by yellow, light gray, and dark gray colors. Reproduced from ref. 1 with permission from The Royal Society of Chemistry, copyright 2018.
- Figure 2.5** XRD patterns of polymorph II, P3<sub>1</sub>, and P3<sub>2</sub> crystal phases. Reproduced from ref. 1 with permission from The Royal Society of Chemistry, copyright 2018.
- Figure 2.6** Projection views of P3<sub>1</sub> and P3<sub>2</sub> crystal phases along [100] directions. Reproduced from ref. 1 with permission from The Royal Society of Chemistry, copyright 2018.
- Figure 2.7** XRD patterns of polymorph II: experimental (black line), Rietveld refined (red line), their difference (green line), and (a) P3<sub>1</sub> and (b) P3<sub>2</sub> crystal phases with Pd atoms (blue line). Reproduced from ref. 1 with permission from The Royal Society of Chemistry, copyright 2018.
- Figure 2.8** Projection views of (a) P3<sub>1</sub> and (b) P3<sub>2</sub> crystal phases with Pd atoms along [001] and [100] directions. Carbon, hydrogen, and palladium are colored yellow, white, and dark

cyan, respectively. Reproduced from ref. 1 with permission from The Royal Society of Chemistry, copyright 2018.

**Figure 2.9** Projection views of (a)  $R\bar{3}$  crystal phase and (b) graphite with Connolly surface along [001] and [100] directions. Carbon and hydrogen are colored yellow and white, respectively. Reproduced from ref. 1 with permission from The Royal Society of Chemistry, copyright 2018.

**Figure 2.10** The optimized structure of Li-inserted c-HBC and the electrostatic potential maps of c-HBC without Li-ion. The electrostatic potential is mapped onto the Connolly surface (top) and (001) and (010) planes across the center of Li-ion (bottom left and right). Carbon, hydrogen, and lithium are colored yellow, white, and purple, respectively. Reproduced from ref. 1 with permission from The Royal Society of Chemistry, copyright 2018.

**Figure 2.11** Projection views of the optimized stable structures of 3, 6, 9, and 18 Li-inserted  $R\bar{3}$  crystal phase. Carbon, hydrogen, and lithium are colored yellow, white, and purple, respectively. Reproduced from ref. 1 with permission from The Royal Society of Chemistry, copyright 2018.

**Figure 2.12** Formation energies of Li-inserted c-HBC as a function of the number of Li-ions. The calculated convex hull is shown as a red line. Reproduced from ref. 1 with permission from The Royal Society of Chemistry, copyright 2018.

**Figure 2.13** The experimental (black line) and calculated (red and blue lines) voltage profiles. Reproduced from ref. 1 with permission from The Royal Society of Chemistry, copyright 2018.

## Chapter 3

- Figure 3.1** (a) Chemical structures and (b) DFT-calculated energy diagrams of the molecular orbitals of contorted hexabenzocoronene (cHBC) and fluorinated cHBC (F-cHBC). Reproduced from ref. 1 with permission from WILEY-VCH Verlag GmbH & Co. KGaA, Weinheim, copyright 2018.
- Figure 3.2** 1D GIWAX diffraction traces from in situ GIWAXS as a function of the annealing temperature. Reproduced from ref. 1 with permission from WILEY-VCH Verlag GmbH & Co. KGaA, Weinheim, copyright 2018.
- Figure 3.3** XRD patterns of F-cHBC (left): experimental (black line), Rietveld refined (red line), their difference (green line), and the  $P2_1/c$  crystal phase (blue line) ( $R_{wp} = 13.21\%$ ,  $R_p = 9.74\%$ ). Projection views of the  $P2_1/c$  crystal structure along the [100] (right top) and [010] (right bottom) directions. Gray: carbon, red: fluorine, white: hydrogen. Reproduced from ref. 1 with permission from WILEY-VCH Verlag GmbH & Co. KGaA, Weinheim, copyright 2018.
- Figure 3.4** The optimized structure and electrostatic potential maps of F-cHBC. The electrostatic potential is mapped onto the Connolly surface. Carbon, hydrogen, and fluorine are colored grey, white, and red, respectively. Reproduced from ref. 1 with permission from WILEY-VCH Verlag GmbH & Co. KGaA, Weinheim, copyright 2018.
- Figure 3.5** (a) Projection views of the optimized  $P2_1/c$  crystal structure of Li-adsorbed F-cHBC along the [100] (top) and [010] (bottom) directions. Gray: carbon, red: fluorine, white: hydrogen, yellow: lithium at site I, purple: lithium at site II. (b) Magnified view of Li-ion at site I (top) and site II (bottom). Black dotted arrow: distance between Li ion and fluorine or between Li ion and the centroid of the bent edge aromatic ring. Orange line: interaction of adsorbed Li ion with negatively charged atoms. Reproduced from ref. 1 with permission from WILEY-VCH Verlag GmbH & Co. KGaA, Weinheim, copyright 2018.
- Figure 3.6** Formation energies of Li-adsorbed F-cHBC as a function of Li-ion content. Red line: convex hull. Reproduced from ref. 1 with permission from WILEY-VCH Verlag GmbH & Co. KGaA, Weinheim, copyright 2018.

- Figure 3.7** Projection views of the optimized  $P2_1/c$  crystal phase and 4, 8 Li-adsorbed F-cHBC stable structures along the [100] and [010] directions. Carbon, hydrogen, fluorine, and lithium are colored grey, white, red and purple, respectively. Reproduced from ref. 1 with permission from WILEY-VCH Verlag GmbH & Co. KGaA, Weinheim, copyright 2018.
- Figure 3.8** Experimental (black line) and calculated (red line) voltage profiles. Reproduced from ref. 1 with permission from WILEY-VCH Verlag GmbH & Co. KGaA, Weinheim, copyright 2018.
- Figure 3.9** Projection views along the [100] and [010] directions of the F-cHBC structures with 4 and 8 Na-ions adsorbed and their corresponding formation energies. Carbon, hydrogen, fluorine and sodium are colored grey, white, red and orange, respectively. Reproduced from ref. 1 with permission from WILEY-VCH Verlag GmbH & Co. KGaA, Weinheim, copyright 2018.
- Figure 3.10** Experimental (black line) and the calculated (red line) voltage profiles. Reproduced from ref. 1 with permission from WILEY-VCH Verlag GmbH & Co. KGaA, Weinheim, copyright 2018.

## Chapter 4

**Figure 4.1** Structure of the redox-active covalent triazine framework (rCTF). Reproduced from ref. 1 with permission from WILEY-VCH Verlag GmbH & Co. KGaA, Weinheim, copyright 2020.

**Figure 4.2** The experimentally observed and theoretically calculated (simulated) XRD pattern of rCTF from the optimized structure with slipped-parallel stacking. Optimized rCTF structure with slipped-parallel stacking. Carbon, hydrogen, nitrogen, and oxygen are light gray, white, dark blue, and red, respectively. Reproduced from ref. 1 with permission from WILEY-VCH Verlag GmbH & Co. KGaA, Weinheim, copyright 2020.

**Figure 4.3** Two grids were used to sample structures with different *ab*-plane displacements between top and bottom layers for generating potential energy surface. The grid is represented in fractional coordinates. The top layer is colored by blue. Reproduced from ref. 1 with permission from WILEY-VCH Verlag GmbH & Co. KGaA, Weinheim, copyright 2020.

**Figure 4.4** The potential energy surface generated by interpolating the DFTB total energies. Reproduced from ref. 1 with permission from WILEY-VCH Verlag GmbH & Co. KGaA, Weinheim, copyright 2020.

**Figure 4.5** Optimized rCTF structure with slipped-parallel stacking. Carbon, hydrogen, nitrogen, and oxygen are light gray, white, dark blue, and red, respectively. Reproduced from ref. 1 with permission from WILEY-VCH Verlag GmbH & Co. KGaA, Weinheim, copyright 2020.

**Figure 4.6** The lithium storage mechanism of rCTF. Top view of the lithium-inserted rCTF structures during the three-stages of the lithiation of rCTF. Carbon, hydrogen, nitrogen, and oxygen are light gray, white, blue, and red, respectively. The atoms in the bottom layer are shown in darker colors for clarity. The magenta-colored sphere represents lithium interacting with at least more than one C=O group of anthraquinone (AQ) including the lithium interacting simultaneously with the AQ and triazine (T), or simultaneously with the AQ and benzene (B). The orange-colored sphere represents lithium interacting with T or interacting simultaneously with T and B. The lithium interacting with benzene only is represented by the green-colored sphere. Reproduced

from ref. 1 with permission from WILEY-VCH Verlag GmbH & Co. KGaA, Weinheim, copyright 2020.

- Figure 4.7** Magnified views of the lithium-inserted rCTF structures at stage 1. The black arrows indicate rCTF layer translation. The magenta spheres represent lithium interacting with at least more than one C=O group of anthraquinone (AQ). Reproduced from ref. 1 with permission from WILEY-VCH Verlag GmbH & Co. KGaA, Weinheim, copyright 2020.
- Figure 4.8** Magnified views of the lithium-inserted rCTF structures at stage 2. The magenta spheres represent lithium interacting with at least more than one C=O group of anthraquinone (AQ) including the lithium interacting simultaneously with AQ and triazine (T). The orange spheres represent lithium interacting with T or interacting simultaneously with T and benzene (B). Reproduced from ref. 1 with permission from WILEY-VCH Verlag GmbH & Co. KGaA, Weinheim, copyright 2020.
- Figure 4.9** Magnified views of the lithium-inserted rCTF structures at stage 3. The magenta spheres represent lithium interacting with at least more than one C=O group of anthraquinone (AQ) including the lithium interacting simultaneously with AQ and triazine (T), or simultaneously with AQ and benzene (B). The orange spheres represent lithium interacting with T or interacting simultaneously with T and B. The lithium interacting with only benzene is represented by green spheres. Reproduced from ref. 1 with permission from WILEY-VCH Verlag GmbH & Co. KGaA, Weinheim, copyright 2020.
- Figure 4.10** Averaged bond length profile of the functional groups in rCTF. Reproduced from ref. 1 with permission from WILEY-VCH Verlag GmbH & Co. KGaA, Weinheim, copyright 2020.
- Figure 4.11** Top and front views of the fully lithiated rCTF structures (specific capacity = 1198 mAh g<sup>-1</sup>). Carbon, hydrogen, nitrogen, and oxygen are light gray, white, blue, and red, respectively. Lithium is represented in different colors depending on the number of functional groups in close contact with the lithium. The criterion distance for close contact between two atoms was set to 89% of the sum of their van der Waals radii. Reproduced from ref. 1 with permission from WILEY-VCH Verlag GmbH & Co. KGaA, Weinheim, copyright 2020.

- Figure 4.12** The number of lithium atoms stored in each functional group per rCTF unit, per the model used here. Reproduced from ref. 1 with permission from WILEY-VCH Verlag GmbH & Co. KGaA, Weinheim, copyright 2020.
- Figure 4.13** Calculated voltage profile of the rCTF lithiation process. Reproduced from ref. 1 with permission from WILEY-VCH Verlag GmbH & Co. KGaA, Weinheim, copyright 2020.
- Figure 4.14** Schematic of the rCTF lithiation process. The gray arrows indicate the rCTF layer translation. Carbon, hydrogen, nitrogen, and oxygen are light gray, white, blue, and red, respectively. Reproduced from ref. 1 with permission from WILEY-VCH Verlag GmbH & Co. KGaA, Weinheim, copyright 2020.
- Figure 4.15** Relaxed structure of rCTF after lithiation and delithiation. Reproduced from ref. 1 with permission from WILEY-VCH Verlag GmbH & Co. KGaA, Weinheim, copyright 2020.
- Figure 4.16** PDOS plots of lithiated rCTF in initial state, the end of stage 1, the end of stage 2 and the end of stage 3. Benzene in the plots refers to the 6 carbon ring located between the two triazine rings in rCTF. Reproduced from ref. 1 with permission from WILEY-VCH Verlag GmbH & Co. KGaA, Weinheim, copyright 2020.



## Chapter 5

- Figure 5.1** Schematic representation of a full-cell LIB containing semicrystalline PVDF binder that can form various polymorphs depending on chain conformation and chain packing mode. Reproduced from ref. 1 with permission from Elsevier Ltd., copyright 2016.
- Figure 5.2** Crystal structure, chain conformation, chain packing, and polarization characteristic of  $\alpha$ - and  $\beta$ -PVDF. Carbon, fluorine, and hydrogen are grey, green, and white, respectively. The brown arrows indicate the dipole direction of each chain.
- Figure 5.3** The electrostatic potential map (left panel) and the total and layer-projected DOS (right panel) of (a)  $\alpha$ -PVDF and (b)  $\beta$ -PVDF slab models with F-terminated surfaces, respectively. Reproduced from ref. 1 with permission from Elsevier Ltd., copyright 2016.
- Figure 5.4** The electrostatic potential map (left panel), the total and layer-projected DOS (right panel) of (a)  $\alpha$ -PVDF and (b)  $\beta$ -PVDF slab models with H-terminated surfaces, respectively. Reproduced from ref. 1 with permission from Elsevier Ltd., copyright 2016.
- Figure 5.5** (a) The slab models of  $\beta$ -PVDF with different number of molecular layers (ML) from 1 to 16. Blue and red dashed circles depict F-terminated surface and H-terminated surfaces, respectively. Carbon, fluorine, hydrogen, and fixed atoms are grey, cyan, white, and dark grey colors, respectively. (b) Total DOS for all layers. Layer-projected DOS for (c) F-terminated and (d) H-terminated surfaces, respectively. Reproduced from ref. 1 with permission from Elsevier Ltd., copyright 2016.
- Figure 5.6** Charge transfer in the slab models for (a) F-terminated  $\alpha$ -PVDF surface, (b) F-terminated  $\beta$ -PVDF surface, (c) H-terminated  $\alpha$ -PVDF surface, and (d) H-terminated  $\beta$ -PVDF surface. Carbon, fluorine, hydrogen, and fixed atoms are grey, cyan, white, and dark grey, respectively. Reproduced from ref. 1 with permission from Elsevier Ltd., copyright 2016.
- Figure 5.7** Schematic diagram of charge transfer in (a)  $\alpha$ -PVDF and (b)  $\beta$ -PVDF. Reproduced from ref. 1 with permission from Elsevier Ltd., copyright 2016.
- Figure 5.8** Profiles of  $xy$ -plane averaged electrostatic potential along the  $z$ -axis of slab models for (a) F-terminated  $\alpha$ -PVDF surface, (b) F-terminated  $\beta$ -PVDF surface, (c) H-terminated  $\alpha$ -PVDF surface, and (d) H-terminated  $\beta$ -PVDF surface.  $W$  denotes the work function of

each surface. Reproduced from ref. 1 with permission from Elsevier Ltd., copyright 2016.

**Figure 5.9** (a) Adsorption energy of Li-ion on F-terminated  $\alpha$ - and  $\beta$ -PVDF surfaces. (b) Adsorption energy of Li-ion on H-terminated  $\alpha$ - and  $\beta$ -PVDF surfaces. Carbon, fluorine, hydrogen, lithium and fixed atoms are grey, cyan, white, purple and dark grey, respectively. Reproduced from ref. 1 with permission from Elsevier Ltd., copyright 2016.

**Figure 5.10** Schematic illustration of a LIB electrode using ferroelectric and paraelectric PVDF binder. Reproduced from ref. 1 with permission from Elsevier Ltd., copyright 2016.

**Figure 5.11** MD simulation snapshots of a 35-mer PVDF chain on LFP (010) surface. Two different polarization directions, which were vertical to the surface, were considered (upward (left) and downward (right) directions). Purple arrow represents the direction of net dipole moment of PVDF. Carbon, fluorine, hydrogen, lithium, iron, and oxygen atoms are grey, cyan, white, dark blue, light pink, and red, respectively. Reproduced from ref. 1 with permission from Elsevier Ltd., copyright 2016.

**Figure 5.12** Interaction energy profile with respect to the rotation angle of a 5-mer PVDF chain on the LFP (010) surface. Carbon, fluorine, hydrogen, lithium, iron, oxygen and fixed atoms are grey, cyan, white, dark blue, light pink, red, and dark grey, respectively. Reproduced from ref. 1 with permission from Elsevier Ltd., copyright 2016.

## Chapter 6

- Figure 6.1** Projection views along the [100] and [001] directions of the optimized crystal structures of (a)  $\alpha$ -chitin with O6A conformation, (b)  $\alpha$ -chitin with O6B conformation, and (c)  $\beta$ -chitin. Magnified images show the molecular structure of  $\beta$ -(1,4)-N-acetyl-D-glucosamine in each crystal structure. Orange and purple arrows indicate the polarization direction of each chitin molecule along [001] and  $[00\bar{1}]$ , respectively. The C, H, N, and O atoms are colored gray, white, blue, and red, respectively. Reproduced from ref. 2 with permission from Elsevier Ltd., copyright 2018.
- Figure 6.2** Spontaneous polarization of  $\beta$ -chitin nanofibers. The arrow pointing from red to blue represents the polarization direction. The positively and negatively charged atoms are blue and red, respectively. Reproduced from ref. 2 with permission from Elsevier Ltd., copyright 2018.
- Figure 6.3** MD snapshots showing the degree of physicochemical affinity to Li cation with PP(Celgard),  $\alpha$ -chitin, and  $\beta$ -chitin. Reproduced from ref. 1 with permission from American Chemical Society, copyright 2017.
- Figure 6.4** The atomic configuration of (a) (100) and (b) (010) planes of  $\alpha$ -chitin fibers. The blue dotted lines represent the hydrogen bonds inside the alpha chitin fibers and the red dotted lines represent the dangling hydrogen bonds of the polar amid and hydroxyl groups exposed on the chitin fiber surface. Carbon, hydrogen, nitrogen, and oxygen are gray, white, blue, and red colors, respectively. Reproduced from ref. 1 with permission from American Chemical Society, copyright 2017.
- Figure 6.5** The RDFs of  $\alpha$ -chitin,  $\beta$ -chitin, and PP with Li-ions. Reproduced from ref. 1 with permission from American Chemical Society, copyright 2017.
- Figure 6.6** The optimized geometries of (a)  $[\text{Li}(\text{DME})_2(\text{PP})]^+$ , (b)  $[\text{Li}(\text{DME})_2(\text{chitin})]^+$ , and (c)  $[\text{Li}(\text{DME})_3]^+$  complexes with the calculated binding energies of  $\text{Li}^+$  to surrounding molecules. The polymer, DME molecule, and oxygen atom are dark gray, light gray and red colors, respectively. Reproduced from ref. 1 with permission from American Chemical Society, copyright 2017.

**Figure 6.7** The normalized adhesion energy of  $\alpha$ -chitin and  $\beta$ -chitin to PP in the electrolyte solution. Reproduced from ref. 1 with permission from American Chemical Society, copyright 2017.

## List of Tables

**Table 1.1** Multiscale simulation methods and simulation programs.

**Table 6.1** The information of the model systems.  $N_{\text{chains}}$ ,  $N_{\text{DME}}$ ,  $N_{\text{Li}^+}$ , and  $N_{\text{TFSI}^-}$  are the number of chains constituting the nanofiber, DME molecules, Li ions, and TFSI ions contained in each model system, respectively.

## Chapter 1. Introduction

### 1.1 Introduction of Rechargeable Batteries

With an ever-growing demand for electrical power sources, electrochemical energy storage systems play an indispensable role in our society. The most representative electrochemical energy storage device is a rechargeable battery (or a secondary battery), which can be designed with various chemistries and materials. Particularly, rechargeable lithium-ion batteries have demonstrated considerable potential owing to their high round-trip efficiency and long cycle life. They are widely used for powering portable/consumer electronics, the electrification of the transportation sector, and the integration of renewable energy sources into the electrical grid (**Figure 1.1**).<sup>1-5</sup>

Innovative advances have been made in rechargeable battery technologies over the past two decades.<sup>6-8</sup> However, there is still a strong demand for improving battery performance to meet the requirements of future electronics or electric vehicles, such as high energy density, high power density, long lifetime, safety, and lower cost.<sup>9-12</sup> Most of them are usually determined by the performance of the constituting battery materials, such as cathode, anode, electrolyte, and separator. It is, therefore, essential to discover or design new battery materials for next-generation rechargeable batteries, which will outperform conventional materials.

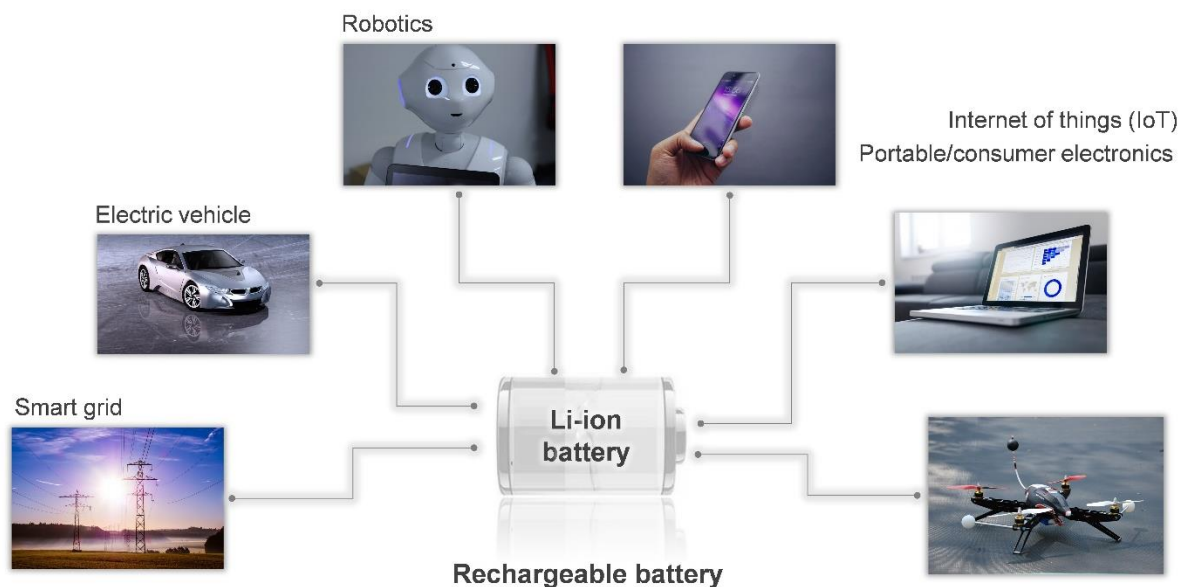


**Figure 1.1** Various applications of rechargeable batteries.

## 1.2 Introduction of Charge Storage Mechanism

Understanding the underlying mechanisms of the electrochemical processes that occurs upon charge storage is critical to design new battery materials required for the further development of high-performance rechargeable batteries. For the Li-ion rechargeable battery, three typical charge storage mechanisms, or more precisely, the reaction mechanism between electrode materials and Li-ion, are well-known: the intercalation mechanism, conversion mechanism, and alloying mechanism (**Figure 1.2**).<sup>13-17</sup>

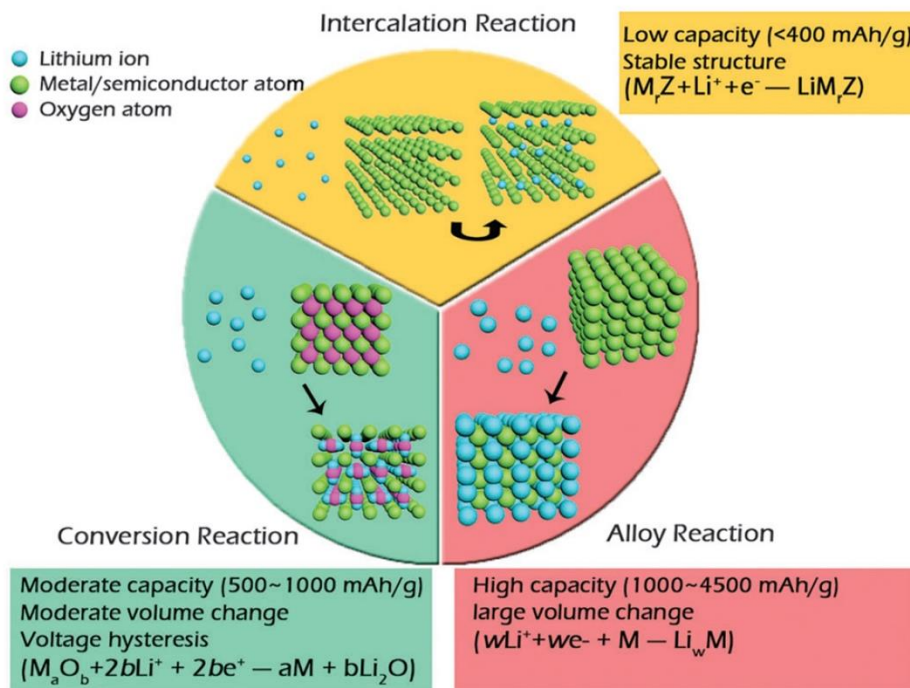


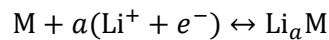
**Figure 1.2** A schematic representation of three typical reaction mechanisms between lithium ion and electrode materials.<sup>17</sup> Reproduced from ref. 17 with permission from The Royal Society of Chemistry, copyright 2015.

### 1.2.1 Intercalation Mechanism

The intercalation mechanism is defined as the electrochemical process where Li-ions are reversibly inserted into and removed from a crystalline host lattice during charging and discharging. Representative intercalation materials are metal chalcogenides, layered transition metal oxides, spinel transition metal oxides, olivine polyanions, and tavorite polyanions for the cathode,<sup>16</sup> and carbon-based materials (graphite, graphene, and carbon nanotube),<sup>18, 19</sup> titanium oxide-based materials (TiO<sub>2</sub> and Li<sub>4</sub>Ti<sub>5</sub>O<sub>12</sub>),<sup>20-22</sup> and orthorhombic Nb<sub>2</sub>O<sub>5</sub> (T-Nb<sub>2</sub>O<sub>5</sub>) for the anode.<sup>23</sup> The intercalation and deintercalation processes are generally accompanied by minimal structural changes, such as an increase in the interlayer distance or in-plane movement of the layers, which results in a small volume change of less than 25%. Moreover, intercalation materials provide fast reaction kinetics with an open framework (Li-ion conductive 1D, 2D, or 3D channels) and a small difference between charging and discharging voltage. However, the major drawback is that most intercalation materials have relatively low volumetric and gravimetric capacities owing to finite accommodation sites for Li-ions per host atom.

### 1.2.2 Alloying Mechanism

Alloying materials react with lithium to form binary compounds via a reversible electrochemical reaction during charging and discharging, as follows:<sup>24-26</sup>

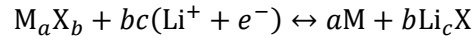


Most alloying materials are metals and metalloids (semi-metals), such as Si,<sup>27</sup> Ge,<sup>28</sup> Sn, Al, and Ga. Alloying materials can accommodate multiple lithium atoms per unit, thus delivering the highest volumetric and gravimetric energy densities. However, because of densely packed structures, alloying materials undergo significant structural changes, and thus, severe volume variations occur upon a reaction with lithium, leading to the pulverization and amorphization of electrode materials with the loss of electrical contact and capacity fading.



### 1.2.3 Conversion Mechanism

Conversion materials reversibly react with lithium during charging and discharging, according to the following general equation:<sup>29</sup>



where M is transition metal, X denotes the anion, such as O, P, N, and F, and  $c$  is the formal oxidation state of X. For example, metal oxides are converted to their metallic state along with the formation of  $\text{Li}_2\text{O}$  and reversibly returned to their initial state after delithiation. Representative conversion materials are metal oxides,<sup>30</sup> fluorides,<sup>31, 32</sup> chlorides, sulfides,<sup>33</sup> phosphides, and nitrides. Conversion materials exhibit relatively high theoretical capacities owing to the ability to transfer more than one electron per metal atom during a redox reaction with lithium. However, a major concern of these materials is a remarkably large voltage hysteresis of  $\sim 1$  V, which is likely caused by the interconversion of multiple solid phases and breaking of strong chemical bonds. Another issue is caused by the large volume expansion during lithium uptake, as in the alloying materials.

## 1.3 Introduction of Polymorphism

### 1.3.1 General Introduction of Polymorphism

The term “polymorphism”, derived from the Greek words “poly” (many) and “morphe” (form), has been used with different meanings in various scientific disciplines. In chemistry and materials science, which are the focus of this thesis, polymorphism refers to the phenomenon in which a solid compound with the same stoichiometry and chemical composition exists in various forms and/or crystal structures (**Figure 1.3**).<sup>34</sup> Polymorphism is an interesting phenomenon common to both organic, inorganic, and organometallic compounds in the crystalline solid state. It is still challenging to predict whether a compound will be polymorphic or not; however, according to the various crystallographic databases, 37–66% of compounds exhibit polymorphism.<sup>35, 36</sup> Most polymorphic compounds are reported to have two polymorphs (89%), while some polymorphic compounds have three (9%), four, or more (2%) polymorphs.

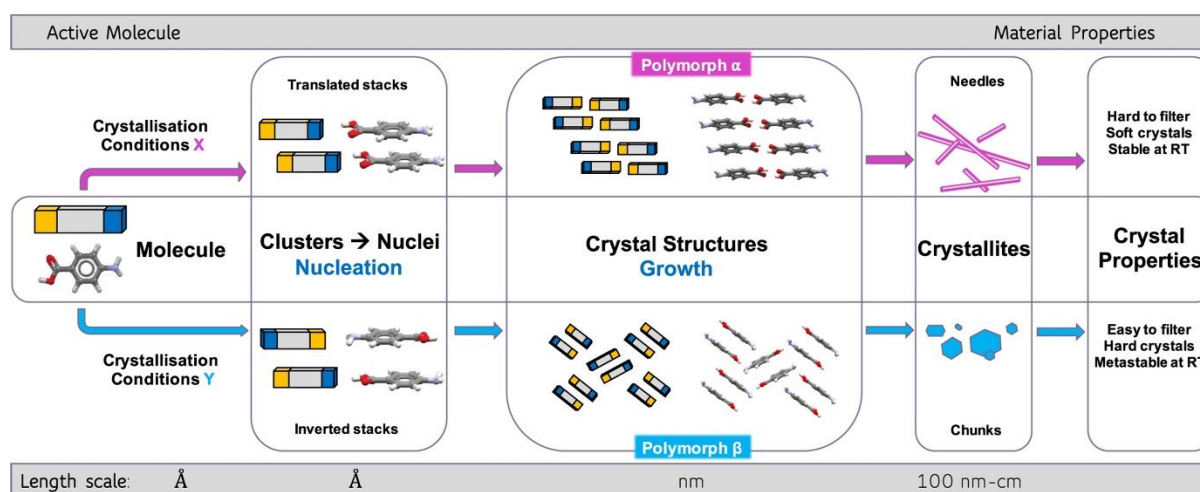


**Figure 1.3** Supramolecular assembly evolution of p-aminobenzoic acid (pABA) from a single molecule into crystallites of two different polymorphs. The assembly occurs via two different routes (pink and blue) as a consequence of two different types of crystallisation conditions (X and Y), which leads to different early assembly, polymorphic structure, crystal shapes and material properties.<sup>35</sup> Reproduced from ref. 35 with permission from Springer Nature, copyright 2020.

The polymorphism was first recognized more than 200 years ago in history. In 1788, Klaproth discovered the first compound with different crystal forms. He identified three different crystal forms of calcium carbonate (CaCO<sub>3</sub>): calcite, vaterite, and aragonite.<sup>37</sup> The formal recognition of polymorphism in inorganic compounds is generally attributed to the work of Mitscherlich in 1822, in which differences in physical and chemical properties were observed in different crystals of arsenates and phosphates.<sup>38</sup> Polymorphism in organic compounds was first observed for benzamide by Liebig and Wohler in 1832.<sup>39</sup> Until the middle of the 20th century, polymorphism was rarely investigated because of major difficulties regarding crystal structure determination at that time. Owing to the recognition of its importance to the development of drugs and other products, its relevance to the high-profile patent litigation, and the advances in structural analysis techniques, the renewed interest in polymorphism and proliferation of studies have occurred since the 1990s (**Figure 1.4**).<sup>36</sup>

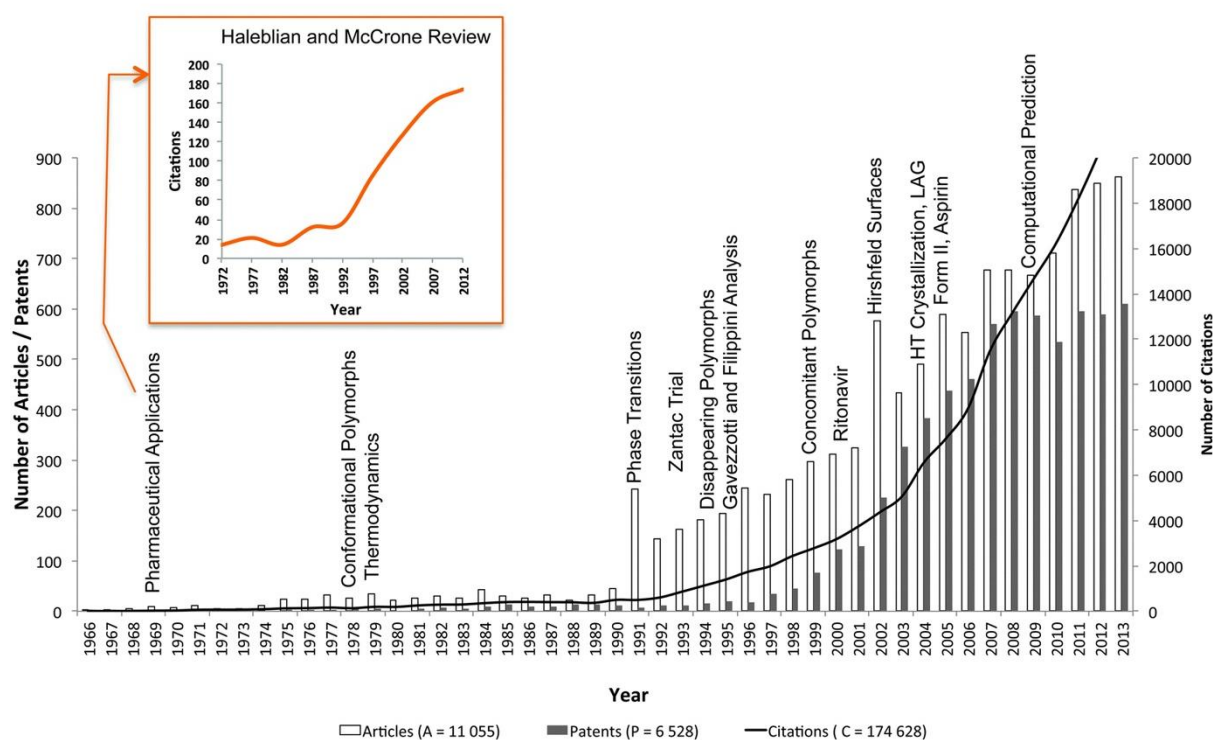


**Figure 1.4** Number of publications, citations to those and patents related to polymorphism. Landmark contributions are indicated and commented further in the text. Inner graph corresponds to the citations history of the McCrone & Haleblian, *J. Pharm. Sci.*, 1969 review.<sup>36</sup> Reproduced from ref. 36 with permission from The Royal Society of Chemistry, copyright 2015.

Polymorphism is an important phenomenon that inspires the design of numerous functional materials. The reason is that different polymorphs can have considerably different chemical, physical, and biological properties. Specifically, polymorphism can lead to differences in chemical reactivity, hardness, compression, thermal expansion, melting temperature, solubility, density, thermal/kinetic stability, vibrational/electronic transitions, electronic conductivity, refractive index, and magnetism. Moreover, polymorphism results in new functional properties such as magnetoelectricity and multiferroicity. Therefore, different polymorphs can exhibit distinct inherent properties, although they are still the same compound. In this context, polymorphism has significant implications in a wide range of fields, including medical research, materials science, catalysis, electronics, pharmaceuticals, agrochemical, pigments, dyestuffs, foods, and explosives. Controlling and exploiting polymorphism provides an opportunity to obtain novel functional materials and access a much wider range of properties without synthesizing new materials.<sup>40</sup>

### 1.3.2 Classification of Polymorphism

Packing polymorphism refers to the polymorphism resulting from the differences in crystal packing (**Figure 1.5**). For example, when molecules with the same chemical composition and conformation are crystallized into different arrangements to form various polymorphs, the type of polymorphism is named packing polymorphism. In this type of polymorphism, intermolecular interactions play a vital role in determining different crystallographic structures. The intermolecular interactions include van der Waals interactions, hydrogen bonding, halogen bonding, charge transfer forces, and coulombic interactions, whose energy range is between 4 and 42 kJ mol<sup>-1</sup> or even wider.

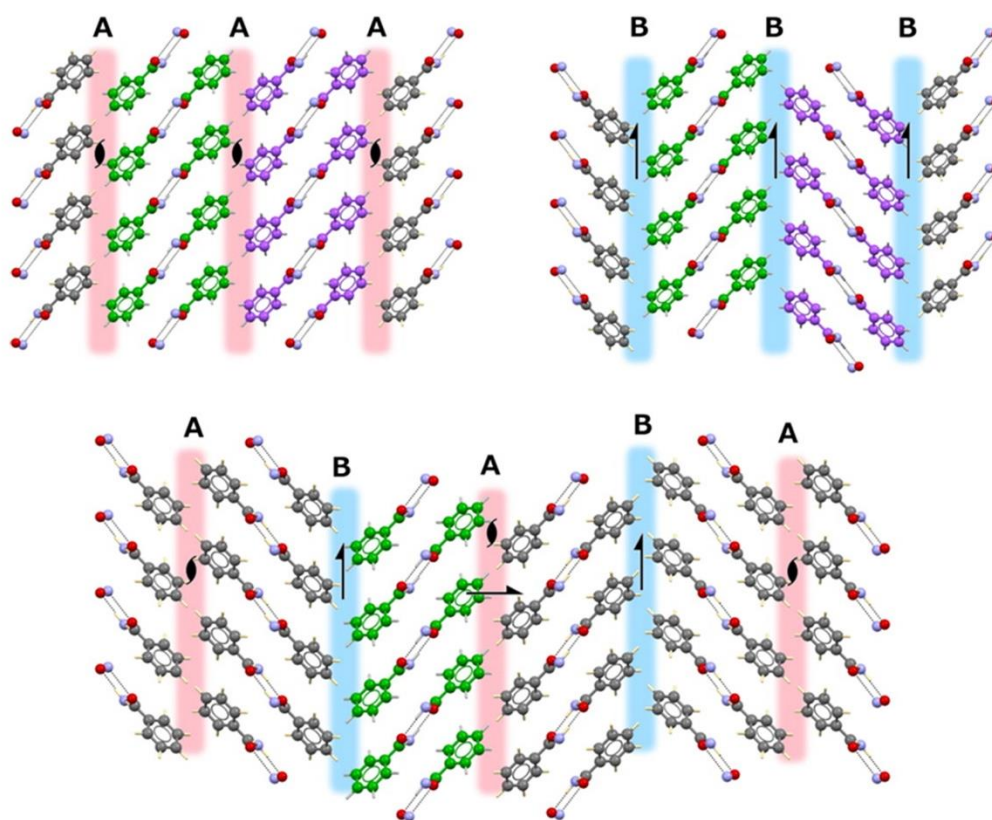


**Figure 1.5** Packing polymorphism of benzamide. Form I (top left) with the parallel stacking of hydrogen-bonded dimers, form III (top right) with a herringbone stacking motif and the hypothetical form from the crystal structure prediction (bottom). All structures are composed of identical layers stacked horizontally. The layers highlighted with green carbon atoms have identical orientation, and the layers with purple carbon atoms are rotated by 180°. The two types of layer interfaces are annotated A and B.<sup>41</sup> Reproduced from ref. 41 with permission from American Chemical Society, <https://doi.org/10.1021/acs.cgd.5b01495>, copyright 2016.

The conformation polymorphism denotes the polymorphism resulting from the existence of different conformers of the same molecule (**Figure 1.6**).<sup>42</sup> It is worth distinguishing definitions of conformation and conformers. Conformations refer to the structures generated through a variation in any torsion angle in a molecule. Conformers only indicate the conformations in a potential energy well.

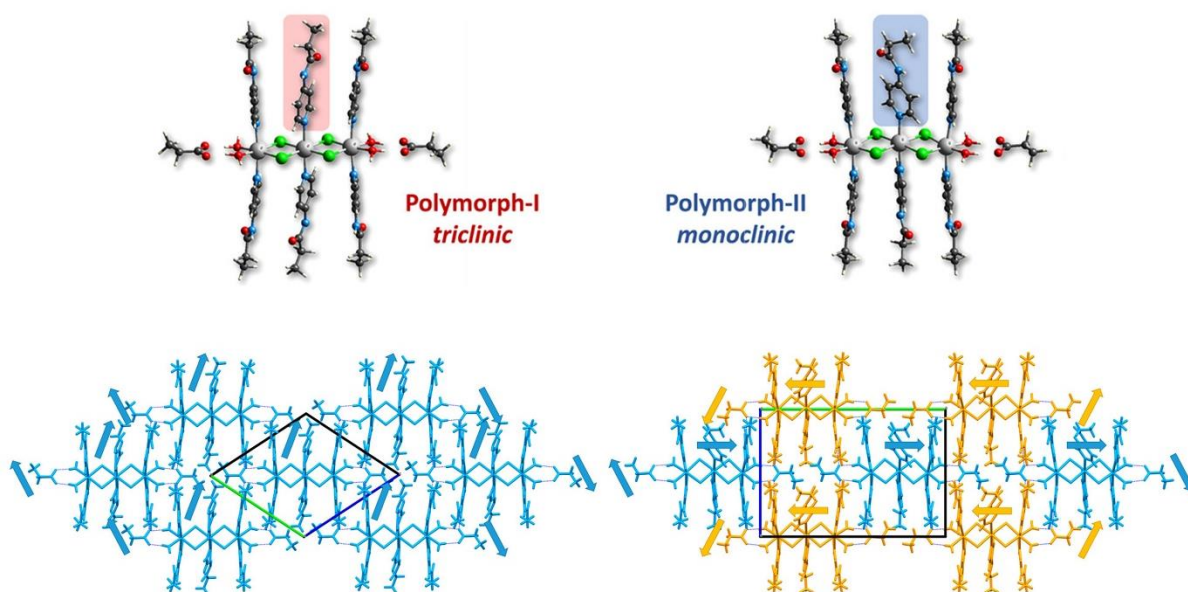


**Figure 1.6** Two conformational polymeric forms of the crystalline cadmium(II) coordination trimer with pyridine-4-propanamide (4-propy),  $[\text{Cd}_3\text{Cl}_4(\text{H}_2\text{O})_4(4\text{-propy})_6](\text{CH}_3\text{CH}_2\text{COO})_2$ . A view of the crystal packings of two polymorphic forms with identical building units in Polymorph-I (blue) and differently colored building units of alternating handedness in Polymorph-II (blue and yellow).<sup>43</sup> Reproduced from ref. 43 with permission from American Chemical Society, copyright 2019.



### 1.3.3 Polymorphism in Battery Materials

Polymorphism can also be found in solid-state battery materials such as electrode active materials, separators, binders, solid-state electrolytes. For example,  $\text{MnO}_2$ , which has been widely used as a cathode material owing to its low cost, eco-friendliness, and excellent safety features, can form various polymorphs, such as hollandite ( $\alpha$ ), pyrolusite ( $\beta$ ), intergrowth ( $\gamma$ ), birnessite (or layered) ( $\delta$ ), spinel ( $\lambda$ ), and ramsdellite (R) phases (**Figure 1.7**).<sup>44-48</sup>  $\text{TiO}_2$  anode material also exists in different polymorphic structures, such as rutile, anatase, brookite, bronze (B), Columbite (II), Hollandite (H), and Ramsdellite (R).<sup>20, 21, 49, 50</sup> Other examples of polymorphic transition metal oxides include  $\text{Fe}_2\text{O}_3$ ,  $\text{CoO}$ , and  $\text{VO}_2$ .<sup>51</sup> In addition, polymorphic behaviors have been observed in organic electrode materials and semi-crystalline polymeric materials for binder or separator.<sup>52-54</sup> Different polymorphs have different channel structures for lithium diffusion, structural stability, lithium accommodation sites, and free energy, directly related to the performance of the battery, including capacity, cyclability, and fast charging. In this context, polymorphism is of particular importance for its potential application as the rechargeable Li-ion battery, providing a library of plentiful attractive structures as the host for the insertion of cations.

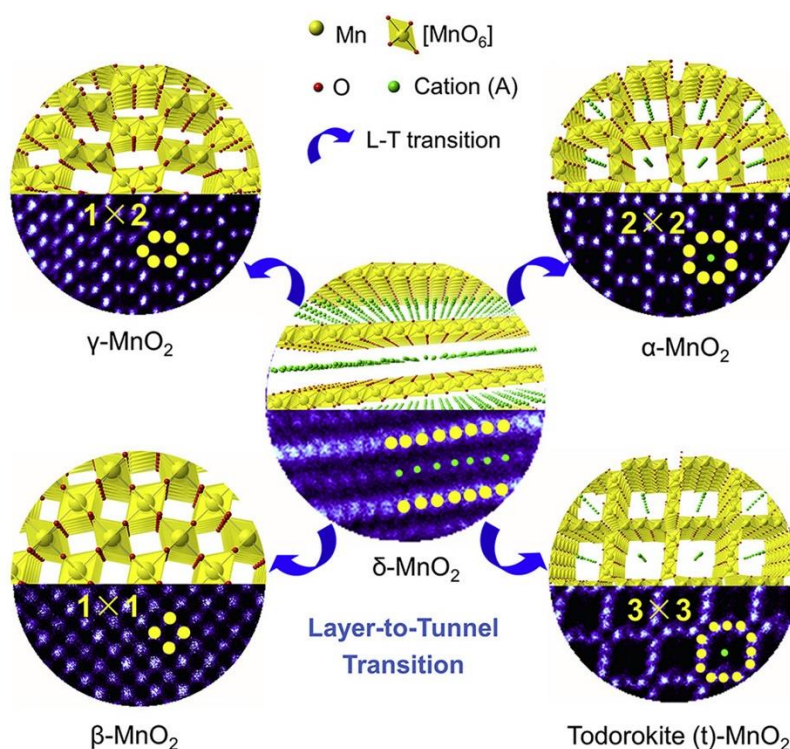


**Figure 1.7** Various polymorphs of  $\text{MnO}_2$ .<sup>45</sup> Reproduced from ref. 45 with permission from Elsevier Inc., copyright 2019.

## 1.4 Introduction of Computer Simulation

### 1.4.1 Importance of Computer Simulation

With the extraordinary advances in computing power, parallel computation, algorithm, and software, computer simulation has attracted considerable attention in various scientific disciplines. The enhanced compatibilities of computational techniques and the development of various theories have enabled the simulation of increasingly complex and realistic systems. Currently, as a virtual experiment, computer simulation plays a central role in the scientific discovery and understanding of observed phenomena or properties of materials. Moreover, it progressively plays an important active role in predicting new functional materials with targeted properties and providing guidance for experiments in different applications. In this context, computer simulation has been considered as a necessary bridge between experiments and theory (**Figure 1.8**). In this dissertation, we investigated the charge storage mechanism and polymorphism using computer simulation to provide information that is challenging to obtain experimentally.

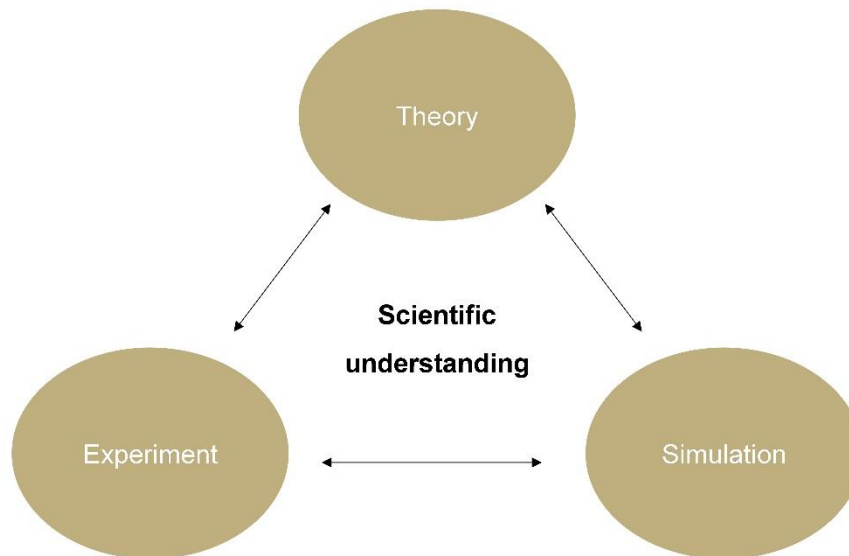


**Figure 1.8** Complementary relationship of theory, experiment, and simulation.



### 1.4.2 Multiscale Computational Approach

Multiscale simulation is an effective computational approach that uses computational methods to observe important features at different scales of time and space. Therefore, multi-scale simulations play a central role in understanding and interpreting complex physicochemical phenomena or properties from the atomic level to the nano level (**Figure 1.9**). Various computational methods relevant for this dissertation are density functional theory calculation, density functional tight binding calculation, molecular dynamics simulation, and Monte Carlo simulation (**Table 1.1**).

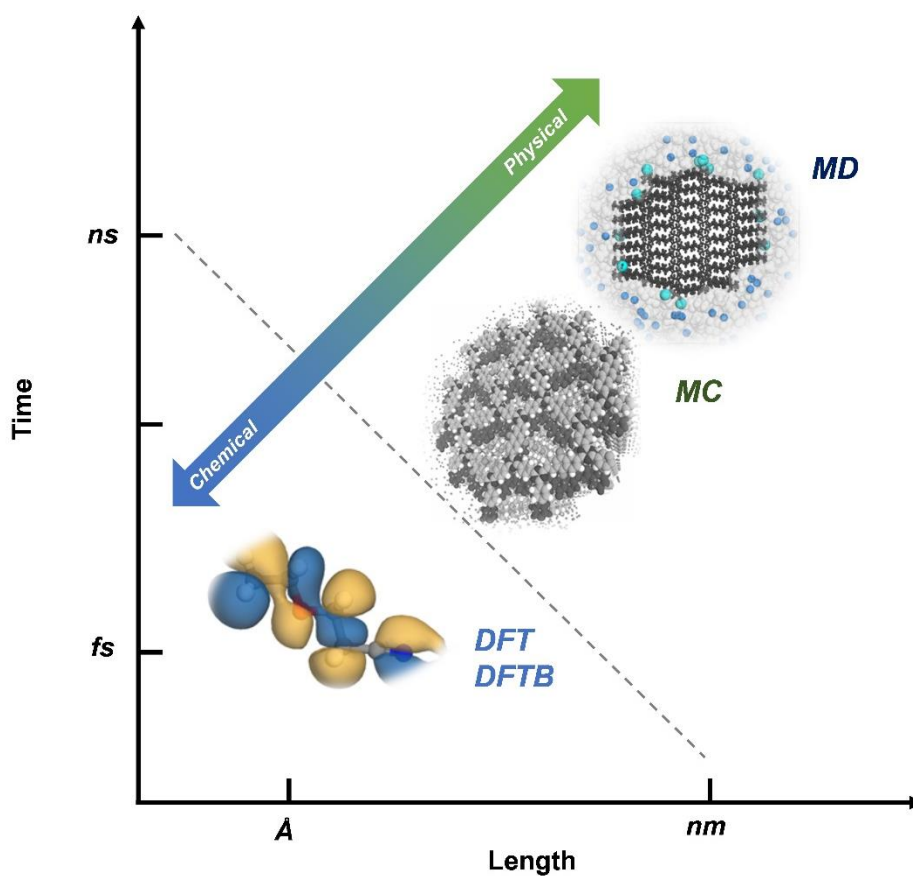


**Figure 1.9** Multiscale computational approach for different time and length scales; density functional theory (DFT) calculation, density functional tight binding (DFTB) calculation, molecular dynamics (MD) simulation, Monte Carlo (MC) simulation.

**Table 1.1** Multiscale simulation methods and simulation programs.

Computational methods	Simulation program
Density functional theory	DMol <sup>3</sup> , CASTEP, VASP, Gaussian, Quantum Espresso
Density functional tight binding	DFTB+
Molecular dynamics	FORCITE, LAMMPS, GROMACS
Monte Carlo	Adsorption Locator, Sorption, RASPA

Density functional theory is a quantum mechanics-based computational method developed by Hohenberg, Kohn, and Sham.<sup>55, 56</sup> In this theory, the ground-state solution to the Schrodinger equation is reformulated as a problem of minimizing energy as a functional of the electron density, which is expressed as the Kohn-Sham equation:

$$E[\rho] = T[\rho] + V_{\text{ext}}[\rho] + V_{\text{H}}[\rho] + V_{\text{xc}}[\rho]$$

where  $T[\rho]$  is the kinetic energy,  $V_{\text{ext}}[\rho]$  is the nucleus electron potential energy,  $V_{\text{H}}[\rho]$  is the classical electron-electron repulsion energy, and  $E_{\text{xc}}[\rho]$  is the exchange and correlation energy. This method has been widely used in chemistry, physics, and materials science to investigate ground-state properties of many-body systems (e.g., atoms, molecules, and condensed matters). It has been commonly utilized in energy storage applications in particular to provide or predict material properties, such as electronic structure, equilibrium cell voltage, voltage profile, ionic mobility, diffusion barrier, and thermal/electrochemical stability. However, because of the high computational cost that increases significantly with the number of electrons, this method is generally used to investigate systems on the time scale of fs ~ ps and length scale of Å ~ nm.

Density functional tight binding method is based on a second-order expansion of the Kohn-Sham total energy in density functional theory with respect to charge density and spin density fluctuations.<sup>57</sup> This method is a useful technique to investigate structural, electronic, and dynamic properties of relatively large and complex materials (more than hundreds of atoms), compared to density functional theory.

Molecular dynamics is a useful method to investigate the physical behaviors of atoms or molecules. In this method, trajectories of atoms are traced by integrating Newton's equations of motion for a system of interacting particles. For a given time step, forces and potentials between atoms are calculated based on interatomic potential, commonly referred to as a forcefield. The representative classical forcefield includes the COMPASS,<sup>58, 59</sup> OPLS-AA,<sup>60</sup> AMBER,<sup>61</sup> and CHARMM.<sup>62</sup> Generally, the potential energy of a system is expressed as a sum of valence term ( $E_{\text{valence}}$ ), cross-coupling term ( $E_{\text{cross-coupling}}$ ), and nonbond interaction term ( $E_{\text{nonbond}}$ ),

$$E_{\text{total}} = E_{\text{valence}} + E_{\text{cross-coupling}} + E_{\text{nonbond}}$$

The valence term is expressed as a sum of energy terms for internal coordinates of bond ( $E_{\text{bond}}$ ), angle ( $E_{\text{angle}}$ ), torsion angle ( $E_{\text{torsion}}$ ), and out-of-plane ( $E_{\text{oop}}$ ),

$$E_{\text{valence}} = E_{\text{bond}} + E_{\text{angle}} + E_{\text{torsion}} + E_{\text{oop}}$$

The cross-coupling term is expressed as a sum of energy terms, including combinations of two or more internal coordinates, which is important for predicting vibrational frequencies or conformational changes. The nonbond term is expressed as a sum of energy terms for van der Waals ( $E_{\text{vdw}}$ ) and electrostatic ( $E_{\text{Coulomb}}$ ) interactions,

$$E_{\text{nonbond}} = E_{\text{vdw}} + E_{\text{Coulomb}}$$

The specific functional forms for each energy term depend on the forcefield. Molecular dynamics simulations can reach a time scale of microsecond and a length scale of a micrometer.

Monte Carlo is a statistical-mechanical method that randomly samples configurations in an ensemble by generating a chain of configurations. Two well-known methods are the Metropolis Monte Carlo method and Configurational bias Monte Carlo method. The latter allows the consideration of a torsional degree of freedom. The Monte Carlo method with the canonical ensemble or simulated annealing algorithm is widely used to simulate the insertion of guest ions or molecules into a host material, to identify possible adsorption configurations and to determine low energy adsorption sites. In addition, this method is also used to predict potential stable or metastable crystal structures of a given compound by generating possible packing arrangements in all reasonable space groups to determine low-lying minima in the lattice energy surface.

## 1.5 References

1. Zeng, X.; Li, M.; Abd El-Hady, D.; Alshitari, W.; Al-Bogami, A. S.; Lu, J.; Amine, K., Commercialization of Lithium Battery Technologies for Electric Vehicles. *Advanced Energy Materials* **2019**, *9* (27), 1900161.
2. Dunn, B.; Kamath, H.; Tarascon, J.-M., Electrical Energy Storage for the Grid: A Battery of Choices. *Science* **2011**, *334* (6058), 928-935.
3. Yang, Z.; Zhang, J.; Kintner-Meyer, M. C. W.; Lu, X.; Choi, D.; Lemmon, J. P.; Liu, J., Electrochemical Energy Storage for Green Grid. *Chemical Reviews* **2011**, *111* (5), 3577-3613.
4. Chu, S.; Majumdar, A., Opportunities and challenges for a sustainable energy future. *Nature* **2012**, *488* (7411), 294-303.
5. Thackeray, M. M.; Wolverton, C.; Isaacs, E. D., Electrical energy storage for transportation—approaching the limits of, and going beyond, lithium-ion batteries. *Energy & Environmental Science* **2012**, *5* (7), 7854-7863.
6. Li, M.; Lu, J.; Chen, Z.; Amine, K., 30 Years of Lithium-Ion Batteries. *Advanced Materials* **2018**, *30* (33), 1800561.
7. Goodenough, J. B.; Park, K.-S., The Li-Ion Rechargeable Battery: A Perspective. *Journal of the American Chemical Society* **2013**, *135* (4), 1167-1176.
8. Armand, M.; Tarascon, J. M., Building better batteries. *Nature* **2008**, *451* (7179), 652-657.
9. Liu, Y.; Zhu, Y.; Cui, Y., Challenges and opportunities towards fast-charging battery materials. *Nature Energy* **2019**, *4* (7), 540-550.
10. Etacheri, V.; Marom, R.; Elazari, R.; Salitra, G.; Aurbach, D., Challenges in the development of advanced Li-ion batteries: a review. *Energy & Environmental Science* **2011**, *4* (9), 3243-3262.
11. Kang, B.; Ceder, G., Battery materials for ultrafast charging and discharging. *Nature* **2009**, *458* (7235), 190-193.
12. Choi, N.-S.; Chen, Z.; Freunberger, S. A.; Ji, X.; Sun, Y.-K.; Amine, K.; Yushin, G.; Nazar, L. F.; Cho, J.; Bruce, P. G., Challenges Facing Lithium Batteries and Electrical Double-Layer Capacitors. *Angewandte Chemie International Edition* **2012**, *51* (40), 9994-10024.
13. Lu, J.; Chen, Z.; Pan, F.; Cui, Y.; Amine, K., High-Performance Anode Materials for Rechargeable Lithium-Ion Batteries. *Electrochemical Energy Reviews* **2018**, *1* (1), 35-53.
14. Chen, R.; Luo, R.; Huang, Y.; Wu, F.; Li, L., Advanced High Energy Density Secondary Batteries with Multi-Electron Reaction Materials. *Advanced Science* **2016**, *3* (10), 1600051.
15. Andre, D.; Hain, H.; Lamp, P.; Maglia, F.; Stiaszny, B., Future high-energy density anode

- materials from an automotive application perspective. *Journal of Materials Chemistry A* **2017**, *5* (33), 17174-17198.
16. Nitta, N.; Wu, F.; Lee, J. T.; Yushin, G., Li-ion battery materials: present and future. *Materials Today* **2015**, *18* (5), 252-264.
  17. Tang, Y.; Zhang, Y.; Li, W.; Ma, B.; Chen, X., Rational material design for ultrafast rechargeable lithium-ion batteries. *Chemical Society Reviews* **2015**, *44* (17), 5926-5940.
  18. Dahn, J. R.; Zheng, T.; Liu, Y.; Xue, J. S., Mechanisms for Lithium Insertion in Carbonaceous Materials. *Science* **1995**, *270* (5236), 590-593.
  19. Kaskhedikar, N. A.; Maier, J., Lithium Storage in Carbon Nanostructures. *Advanced Materials* **2009**, *21* (25-26), 2664-2680.
  20. Dylla, A. G.; Henkelman, G.; Stevenson, K. J., Lithium Insertion in Nanostructured TiO<sub>2</sub>(B) Architectures. *Accounts of Chemical Research* **2013**, *46* (5), 1104-1112.
  21. Deng, D.; Kim, M. G.; Lee, J. Y.; Cho, J., Green energy storage materials: Nanostructured TiO<sub>2</sub> and Sn-based anodes for lithium-ion batteries. *Energy & Environmental Science* **2009**, *2* (8), 818-837.
  22. Yuan, T.; Tan, Z.; Ma, C.; Yang, J.; Ma, Z.-F.; Zheng, S., Challenges of Spinel Li<sub>4</sub>Ti<sub>5</sub>O<sub>12</sub> for Lithium-Ion Battery Industrial Applications. *Advanced Energy Materials* **2017**, *7* (12), 1601625.
  23. Augustyn, V.; Come, J.; Lowe, M. A.; Kim, J. W.; Taberna, P.-L.; Tolbert, S. H.; Abruña, H. D.; Simon, P.; Dunn, B., High-rate electrochemical energy storage through Li<sup>+</sup> intercalation pseudocapacitance. *Nature Materials* **2013**, *12* (6), 518-522.
  24. Obrovac, M. N.; Chevrier, V. L., Alloy Negative Electrodes for Li-Ion Batteries. *Chemical Reviews* **2014**, *114* (23), 11444-11502.
  25. McDowell, M. T.; Lee, S. W.; Nix, W. D.; Cui, Y., 25th Anniversary Article: Understanding the Lithiation of Silicon and Other Alloying Anodes for Lithium-Ion Batteries. *Advanced Materials* **2013**, *25* (36), 4966-4985.
  26. Park, C.-M.; Kim, J.-H.; Kim, H.; Sohn, H.-J., Li-alloy based anode materials for Li secondary batteries. *Chemical Society Reviews* **2010**, *39* (8), 3115-3141.
  27. Chan, C. K.; Peng, H.; Liu, G.; McIlwrath, K.; Zhang, X. F.; Huggins, R. A.; Cui, Y., High-performance lithium battery anodes using silicon nanowires. *Nature Nanotechnology* **2008**, *3* (1), 31-35.
  28. Seo, M.-H.; Park, M.; Lee, K. T.; Kim, K.; Kim, J.; Cho, J., High performance Ge nanowire anode sheathed with carbon for lithium rechargeable batteries. *Energy & Environmental Science* **2011**, *4* (2), 425-428.

29. Cabana, J.; Monconduit, L.; Larcher, D.; Palacín, M. R., Beyond Intercalation-Based Li-Ion Batteries: The State of the Art and Challenges of Electrode Materials Reacting Through Conversion Reactions. *Advanced Materials* **2010**, *22* (35), E170-E192.
30. Yu, S.-H.; Lee, S. H.; Lee, D. J.; Sung, Y.-E.; Hyeon, T., Conversion Reaction-Based Oxide Nanomaterials for Lithium Ion Battery Anodes. *Small* **2016**, *12* (16), 2146-2172.
31. Wang, F.; Robert, R.; Chernova, N. A.; Pereira, N.; Omenya, F.; Badway, F.; Hua, X.; Ruotolo, M.; Zhang, R.; Wu, L.; Volkov, V.; Su, D.; Key, B.; Whittingham, M. S.; Grey, C. P.; Amatucci, G. G.; Zhu, Y.; Graetz, J., Conversion Reaction Mechanisms in Lithium Ion Batteries: Study of the Binary Metal Fluoride Electrodes. *Journal of the American Chemical Society* **2011**, *133* (46), 18828-18836.
32. Li, L.; Meng, F.; Jin, S., High-Capacity Lithium-Ion Battery Conversion Cathodes Based on Iron Fluoride Nanowires and Insights into the Conversion Mechanism. *Nano Letters* **2012**, *12* (11), 6030-6037.
33. Yu, D. Y. W.; Hoster, H. E.; Batabyal, S. K., Bulk antimony sulfide with excellent cycle stability as next-generation anode for lithium-ion batteries. *Scientific Reports* **2014**, *4* (1), 4562.
34. Brog, J.-P.; Chanez, C.-L.; Crochet, A.; Fromm, K. M., Polymorphism, what it is and how to identify it: a systematic review. *RSC Advances* **2013**, *3* (38), 16905-16931.
35. Cruz-Cabeza, A. J.; Feeder, N.; Davey, R. J., Open questions in organic crystal polymorphism. *Communications Chemistry* **2020**, *3* (1), 142.
36. Cruz-Cabeza, A. J.; Reutzel-Edens, S. M.; Bernstein, J., Facts and fictions about polymorphism. *Chemical Society Reviews* **2015**, *44* (23), 8619-8635.
37. Hosseini, M. W., *Molecular networks*. Springer Science & Business Media: 2009; Vol. 132.
38. Mitscherlich, E., On the relationship between crystalline form and chemical composition. I. Note on arsenates and phosphates. *Ann. Chim. Phys* **1822**, *19*, 350-419.
39. Liebig, J.; Wohler, F., Untersuchungen iiber das Radical der Benzoesaure. *Pharm Anntiinflam* **1832**, *249*, 514.
40. Gentili, D.; Gazzano, M.; Melucci, M.; Jones, D.; Cavallini, M., Polymorphism as an additional functionality of materials for technological applications at surfaces and interfaces. *Chemical Society Reviews* **2019**, *48* (9), 2502-2517.
41. Johansson, K. E.; van de Streek, J., Revision of the Crystal Structure of the First Molecular Polymorph in History. *Crystal Growth & Design* **2016**, *16* (3), 1366-1370.
42. Nangia, A., Conformational Polymorphism in Organic Crystals. *Accounts of Chemical Research* **2008**, *41* (5), 595-604.
43. PISAČIĆ, M.; Kodrin, I.; Matijaković, N.; Chatterjee, N.; Oliver, C. L.; Kukovec, B.-M.;

- Đaković, M., Reversible Temperature-Stimulated Single-Crystal-to-Single-Crystal Conformational Polymorph Transformation in Cadmium(II) Coordination Trimer with a Water Vapor Sorption/Desorption Potential. *Crystal Growth & Design* **2020**, *20* (1), 401-413.
44. Devaraj, S.; Munichandraiah, N., Effect of Crystallographic Structure of MnO<sub>2</sub> on Its Electrochemical Capacitance Properties. *The Journal of Physical Chemistry C* **2008**, *112* (11), 4406-4417.
45. Yuan, Y.; He, K.; Byles, B. W.; Liu, C.; Amine, K.; Lu, J.; Pomerantseva, E.; Shahbazian-Yassar, R., Deciphering the Atomic Patterns Leading to MnO<sub>2</sub> Polymorphism. *Chem* **2019**, *5* (7), 1793-1805.
46. Kitchaev, D. A.; Dacek, S. T.; Sun, W.; Ceder, G., Thermodynamics of Phase Selection in MnO<sub>2</sub> Framework Structures through Alkali Intercalation and Hydration. *Journal of the American Chemical Society* **2017**, *139* (7), 2672-2681.
47. Thackeray, M. M., Manganese oxides for lithium batteries. *Progress in Solid State Chemistry* **1997**, *25* (1), 1-71.
48. Gupta, P. K.; Bhandari, A.; Bhattacharya, J.; Pala, R. G. S., Correlating Voltage Profile to Molecular Transformations in Ramsdellite MnO<sub>2</sub> and Its Implication for Polymorph Engineering of Lithium Ion Battery Cathodes. *The Journal of Physical Chemistry C* **2018**, *122* (22), 11689-11700.
49. Aravindan, V.; Lee, Y.-S.; Yazami, R.; Madhavi, S., TiO<sub>2</sub> polymorphs in 'rocking-chair' Li-ion batteries. *Materials Today* **2015**, *18* (6), 345-351.
50. Zachau-Christiansen, B.; West, K.; Jacobsen, T.; Atlung, S., Lithium insertion in different TiO<sub>2</sub> modifications. *Solid State Ionics* **1988**, *28-30*, 1176-1182.
51. Saha, S.; Gupta, P. K.; Pala, R. G. S., Stabilization of non-native polymorphs for electrocatalysis and energy storage systems. *WIREs Energy and Environment* *n/a* (n/a), e389.
52. Park, J.; Lee, C. W.; Joo, S. H.; Park, J. H.; Hwang, C.; Song, H.-K.; Park, Y. S.; Kwak, S. K.; Ahn, S.; Kang, S. J., Contorted polycyclic aromatic hydrocarbon: promising Li insertion organic anode. *Journal of Materials Chemistry A* **2018**, *6* (26), 12589-12597.
53. Song, W.-J.; Joo, S. H.; Kim, D. H.; Hwang, C.; Jung, G. Y.; Bae, S.; Son, Y.; Cho, J.; Song, H.-K.; Kwak, S. K.; Park, S.; Kang, S. J., Significance of ferroelectric polarization in poly(vinylidene difluoride) binder for high-rate Li-ion diffusion. *Nano Energy* **2017**, *32*, 255-262.
54. Kim, J.-K.; Kim, D. H.; Joo, S. H.; Choi, B.; Cha, A.; Kim, K. M.; Kwon, T.-H.; Kwak, S. K.; Kang, S. J.; Jin, J., Hierarchical Chitin Fibers with Aligned Nanofibrillar Architectures: A Nonwoven-Mat Separator for Lithium Metal Batteries. *ACS Nano* **2017**, *11* (6),



- 6114-6121.
55. Hohenberg, P.; Kohn, W., Inhomogeneous Electron Gas. *Physical Review* **1964**, *136* (3B), B864-B871.
  56. Kohn, W.; Sham, L. J., Self-Consistent Equations Including Exchange and Correlation Effects. *Physical Review* **1965**, *140* (4A), A1133-A1138.
  57. Frauenheim, T.; Seifert, G.; Elstner, M.; Niehaus, T.; Köhler, C.; Amkreutz, M.; Sternberg, M.; Hajnal, Z.; Carlo, A. D.; Suhai, S., Atomistic simulations of complex materials: ground-state and excited-state properties. *Journal of Physics: Condensed Matter* **2002**, *14* (11), 3015-3047.
  58. Sun, H.; Jin, Z.; Yang, C.; Akkermans, R. L.; Robertson, S. H.; Spenley, N. A.; Miller, S.; Todd, S. M., COMPASS II: extended coverage for polymer and drug-like molecule databases. *Journal of molecular modeling* **2016**, *22* (2), 47.
  59. Sun, H., COMPASS: An ab Initio Force-Field Optimized for Condensed-Phase Applications Overview with Details on Alkane and Benzene Compounds. *The Journal of Physical Chemistry B* **1998**, *102* (38), 7338-7364.
  60. Jorgensen, W. L.; Maxwell, D. S.; Tirado-Rives, J., Development and Testing of the OPLS All-Atom Force Field on Conformational Energetics and Properties of Organic Liquids. *Journal of the American Chemical Society* **1996**, *118* (45), 11225-11236.
  61. Cornell, W. D.; Cieplak, P.; Bayly, C. I.; Gould, I. R.; Merz, K. M.; Ferguson, D. M.; Spellmeyer, D. C.; Fox, T.; Caldwell, J. W.; Kollman, P. A., A Second Generation Force Field for the Simulation of Proteins, Nucleic Acids, and Organic Molecules. *Journal of the American Chemical Society* **1995**, *117* (19), 5179-5197.
  62. MacKerell, A. D.; Bashford, D.; Bellott, M.; Dunbrack, R. L.; Evanseck, J. D.; Field, M. J.; Fischer, S.; Gao, J.; Guo, H.; Ha, S.; Joseph-McCarthy, D.; Kuchnir, L.; Kuczera, K.; Lau, F. T. K.; Mattos, C.; Michnick, S.; Ngo, T.; Nguyen, D. T.; Prodhom, B.; Reiher, W. E.; Roux, B.; Schlenkrich, M.; Smith, J. C.; Stote, R.; Straub, J.; Watanabe, M.; Wiórkiewicz-Kuczera, J.; Yin, D.; Karplus, M., All-Atom Empirical Potential for Molecular Modeling and Dynamics Studies of Proteins. *The Journal of Physical Chemistry B* **1998**, *102* (18), 3586-3616.



## Chapter 2. Polymorphism and Lithium Storage Mechanism of Contorted Hexabenzocoronene Electrode Material

*This chapter includes the following contents:*

Park, J.<sup>†</sup>; Lee, C. W.<sup>†</sup>; Joo, S. H.<sup>†</sup>; Park, J. H.; Hwang, C.; Song, H.-K.; Park, Y. S.; Kwak, S. K.\*; Ahn, S.\*; Kang, S. J.\*, Contorted polycyclic aromatic hydrocarbon: promising Li insertion organic anode. *Journal of Materials Chemistry A* **2018**, 6 (26), 12589-12597. (†: **equally contributed**).  
Reproduced with permission from The Royal Society of Chemistry, copyright 2018.<sup>1</sup>

---

### 2.1 Introduction

Graphite anode materials are of considerable interest in the field of Li-ion battery (LIB) research, not only because of their highly reversible discharge–charge performance based on intercalation and de-intercalation processes, but also because of their compatibility with conventional carbonate aprotic electrolytes.<sup>2, 3</sup> Since the first successful demonstration of a graphite anode in an LIB system,<sup>4</sup> considerable effort has been devoted to improving anode performance in terms of its energy density, cycle life, and rate capability with high-voltage cathode materials. Although previous works have clearly suggested that carbon is an important anode material that can be combined readily with a number of cathode candidates in a LIB, the recognition of its limited theoretical capacity of 372 mA h g<sup>-1</sup> has inspired the search to find alternatives that could satisfy the demands of future high-capacity cathode materials or alkali-metal-based rechargeable batteries.<sup>5-8</sup>

Various possible anode materials have been demonstrated successfully during the past decade with many exhibiting high-capacity characteristics.<sup>9-17</sup> Among the many innovate anode material candidates, inorganic based anodes, including conversion materials (Fe<sub>2</sub>O<sub>3</sub>, Co<sub>3</sub>O<sub>4</sub>, NiO, and Mn<sub>3</sub>O<sub>4</sub>)<sup>10-13</sup> and alloy reaction anodes (Si, Sb, Bi, and Sn)<sup>14-17</sup> have been shown promising as replacements for graphite anodes because of their enormous energy density range of approximately 600–4200 mA h g<sup>-1</sup>. Although a number of papers have discussed the potential of such anodes as next-generation LIB electrodes, certain technological issues such as large potential hysteresis, phase transformation, and huge volume expansion remain to be addressed in order to achieve ideal operational electrochemical performance.<sup>17</sup>  
<sup>18</sup> In addition various new carbon-based anode materials such as low-dimensional carbon allotropes (graphene, CNT, and fullerenes) have been considered candidates for next-generation anodes.<sup>3, 19, 20</sup> Several important features of such materials, including a large surface area, short diffusion length of

alkali ions, and reversible discharge–charge process, offer a unique surface storage mechanism that can enhance capacity to  $740 \text{ mA h g}^{-1}$  which could be increased further by dopant materials.<sup>21-25</sup> However, complicated synthesis procedures and uneconomic mass production techniques prevent practical implementation.<sup>21, 22, 26</sup>

Organic anode materials have been expected and developed to solve the problems in inorganic and carbon-based electrodes. Considering eco-friendly chemical compositions such as carbon, oxygen, nitrogen, and hydrogen, simple redox processes and facile mass production, organic anode materials such as organic salts, conjugated polymers and compounds with carbonyl groups have been extensively studied. The important characteristics of these materials are the flexible structure modification and decent electrochemical performance. The multi-electron redox reaction mechanism makes it possible to satisfy the energy density and the current rate in LIBs.<sup>27-32</sup> However, because insufficient conducting property and poor cycling stability due to dissolvable structures in electrolytes limit the performance, the new type of organic materials are still demands for LIB anode materials.<sup>27</sup>

This article presents a new type of organic anode material designed to achieve stable cycling performance, superior electrochemical performance, and reversible Li insertion/de-insertion by large  $d$ -spacing and storage space of anode materials at molecular level. We used a contorted polycyclic aromatic hydrocarbon molecule, contorted hexabenzocoronene (c-HBC), which is known to form molecular wires through  $\pi$ - $\pi$  interaction providing sufficient charge transport in various electronic devices.<sup>33-36</sup> This molecular wire structure from the doubly concave c-HBC is expected to provide sufficient conductivity and a large  $d$ -spacing with nanopore channels which enable to easily access Li-ions into the anode materials with superior storage stability. In addition, the conjugated aromatic structure serves to render it insoluble in electrolytes. Our electrochemical results and in-depth theoretical studies verified that the large interspacing of the contorted molecule represents a viable structure for an organic-based LIB anode material. The well-developed crystalline trigonal  $R\bar{3}$  phase (previously polymorph II')<sup>34</sup> of c-HBC exhibits a single peak at 0.21 V in the  $dQ/dV^{-1}$  plot suggesting that our c-HBC anode exhibits unique Li insertion mechanism without voltage penalty. Following the fundamental crystalline phase and Li insertion studies based on the electrochemical performance, we finally validate that the contorted aromatic molecules provide the optimized crystalline structure for Li-ion access and storage, potentially providing a new design concept for organic anode materials in LIBs.

## 2.2 Computational Methods

### 2.2.1 Crystal Structure Prediction

A detailed crystallographic and theoretical polymorphism study of c-HBC was undertaken using the Polymorph module of Materials Studio 2017 R2.<sup>37</sup> The molecular structure of c-HBC, optimized by the density functional theory calculation, was used as the starting geometry for the polymorph prediction. The crystal structure prediction was performed sequentially in six steps: packing, clustering, geometry optimization, clustering, geometry optimization, and clustering. The entire procedure was repeated three times. In the packing step, Monte Carlo simulated annealing was performed for sampling of the crystal structures within a specific space group. The crystal structure prediction procedures were performed for 10 space groups including  $P2_1/c$ ,  $P\bar{1}$ ,  $P2_12_12_1$ ,  $C2/c$ ,  $P2_1$ ,  $Pbca$ ,  $Pna2_1$ ,  $Cc$ ,  $Pbcn$ , and  $C2$ . In order to achieve sufficiently wide sampling, we set the maximum temperature to  $1.5 \times 10^5$  K, minimum temperature to 300 K, maximum number of steps to  $5.0 \times 10^5$ , number of steps to accept before cooling to 100, minimum move factor to  $1.0 \times 10^{-50}$ , and heating factor to 0.025. In the geometry optimization step, the lattice parameters and atomic positions were relaxed under crystallographic symmetry. In the first geometry optimization step, the c-HBC molecules were treated as rigid bodies. The maximum number of steps was set to  $1.0 \times 10^4$  and the convergence criteria were set to  $2.0 \times 10^{-5}$  kcal mol<sup>-1</sup> for energy, 0.001 kcal mol<sup>-1</sup> Å<sup>-1</sup> for force, 0.001 GPa for stress, and  $1.0 \times 10^{-5}$  Å for displacement. In the clustering step, the clusters of many similar structures were determined, and the lowest energy structure representing each cluster was filtered. The criterion of crystal similarity measure was set to 0.11, which was calculated based on a comparison of radial distribution functions with a cutoff distance of 7 Å and 140 bins. After the final clustering step, the space group symmetry of the predicted crystal structures was reanalyzed. The interatomic interactions for the energy calculation and the geometry optimization were described by COMPASS II force field.<sup>38</sup> Short-range van der Waals interaction was calculated between pairs of atoms within a cutoff distance of 18.5 Å. Long-range electrostatic interaction was calculated using the Ewald summation method.<sup>39, 40</sup>

### 2.2.2 Monte Carlo Simulation

To explore the Li-ion insertion sites of c-HBC, Monte Carlo (MC) simulations were performed using the Sorption module of Material Studio 2017 R2.<sup>37</sup> Based on the metropolis algorithm, the Monte Carlo simulations were performed independently 10 times with  $1.0 \times 10^5$  maximum loading steps,  $1.0 \times 10^5$  production steps, and 4 annealing cycles. The interatomic interactions were described by

COMPASS II force field with Mulliken charges obtained by density functional theory calculations.<sup>38</sup>  
41-43

### 2.2.3 Density Functional Theory Calculation

Density functional theory (DFT) calculations were performed using the Cambridge Serial Total Energy Package (CASTEP) in Materials Studio 2017 R2.<sup>37, 44</sup> The generalized gradient approximation with the Perdew–Burke–Ernzerhof (GGA-PBE) functional was used to describe the exchange correlation potential of the electrons.<sup>45</sup> The interactions between ions and electrons were described by on-the-fly generated ultrasoft pseudopotentials. The plane-wave basis set with a cutoff energy of 600 eV was employed to expand the wave functions. The van der Waals interactions were corrected by Grimme’s method.<sup>46</sup> The convergence criterion for self-consistent field calculation was set to  $5.0 \times 10^{-7}$  eV atom<sup>-1</sup>. Lattice parameters and atomic positions were fully relaxed. The convergence criteria for geometry optimization were set to  $5.0 \times 10^{-6}$  eV atom<sup>-1</sup> for the maximum energy change, 0.01 eV Å<sup>-1</sup> for the maximum force, 0.02 GPa for the maximum stress, and  $5.0 \times 10^{-4}$  Å for the maximum displacement. The Brillouin zone was integrated using a  $1 \times 1 \times 1$   $k$ -point grid with the Monkhorst–Pack scheme for all calculations.<sup>47</sup> The formation energy ( $E_f$ ) of the Li-ion inserted structure as a function of Li-ion content was calculated as follows:

$$E_f = E_{\text{Li}_n\text{-c-HBC}} - E_{\text{c-HBC}} - nE_{\text{Li}}$$

where  $E_{\text{Li}_n\text{-c-HBC}}$  is the total energy of the c-HBC crystal with inserted Li-ions,  $n$  is the number of inserted Li-ions,  $E_{\text{c-HBC}}$  is the total energy of the  $R\bar{3}$  crystal phase of c-HBC, and  $E_{\text{Li}}$  is the total energy per atom of bcc bulk Li. The voltage profile ( $V$ ) as a function of Li-ion content was calculated as follows:

$$V(n) = -\frac{E_{\text{Li}_{n_2}\text{-c-HBC}} - E_{\text{Li}_{n_1}\text{-c-HBC}} - (n_2 - n_1)E_{\text{Li}}}{q(n_2 - n_1)}$$

where  $E_{\text{Li}_{n_1}\text{-c-HBC}}$  and  $E_{\text{Li}_{n_2}\text{-c-HBC}}$  represent the total energy of the c-HBC crystal with inserted Li-ions,  $n_1$  and  $n_2$  are the numbers of inserted Li-ions ( $n_2 > n_1$ ),  $E_{\text{Li}}$  is the total energy per atom of bcc bulk Li, and  $q$  is the net charge of Li-ions ( $q = +1e$ ). The formation energies and voltage profile were calculated without dispersion correction.

## 2.3 Results and Discussion

### 2.3.1 Polymorphism of c-HBC

A c-HBC molecule, which consists of 13 aromatic rings, was experimentally synthesized using a previously reported three-step method and subsequently purified by conventional column chromatography.<sup>33, 48</sup> The final product of yellow c-HBC exhibited a doubly concave molecular structure with a distorted pentacene core, which produced a unique crystalline structure because of its steric congestion during solidification (**Figure 2.1a,b**).<sup>35</sup> Our strategy was to adopt this semiconducting c-HBC crystal as the Li host material in a LIB, where the contorted molecular structure could potentially benefit Li-ion insertion and lead to improved conductivity. The schematic presented in **Figure 2.1c** shows the proposed Li-ion insertion mechanism in the c-HBC crystal. We hypothesize that the relatively small aromatic molecules of the c-HBC crystal lower the energy barrier of Li-ion insertion at the edge of the c-HBC crystal as well as reduce diffusion in the crystal interspace.

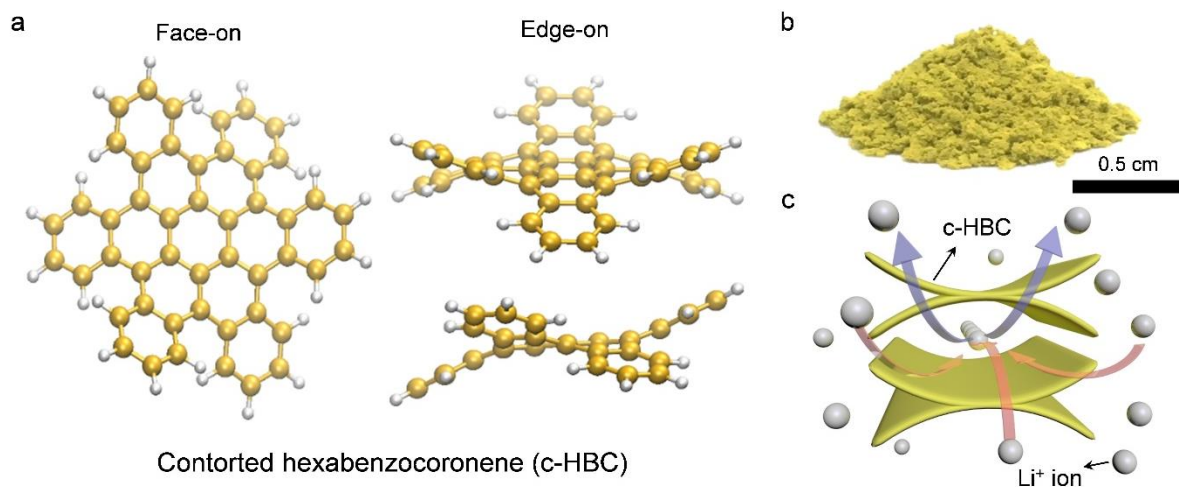


**Figure 2.1** (a) Face-on (left) and edge-on (right) chemical structure of c-HBC. The structure of c-HBC exhibits two concave surfaces. (b) Digital photograph of synthesized c-HBC powder. (c) Schematic of proposed Li-ion insertion mechanism in c-HBC. Reproduced from ref. 1 with permission from The Royal Society of Chemistry, copyright 2018.

Successful development of polymorphic change in c-HBC material has been reported previously by Hiszpanski et al., who found that the  $P2_1/c$  point group of as-prepared c-HBC material could be tuned readily by additional processes such as tetrahydrofuran (THF) solvent and high-temperature ( $\sim 170$  °C) thermal annealing.<sup>34</sup> The key finding behind their research was that the c-HBC crystal could be transformed to new polymorph II and polymorph II' crystal phases by subsequent treatments. Therefore, we employed solvent and thermal annealing treatments to facilitate polymorphic change in our c-HBC anode, which we verified by performing high-flux synchrotron grazing incidence X-ray diffraction (GIXD) measurements. As shown in **Figure 2.2**, the resulting diffraction pattern show the different crystal structures based on the sample preparation procedure. For example, strong reflections at  $q = 1.04$  and  $q = 1.15$   $\text{\AA}^{-1}$  are clearly visible in the samples of as-prepared and THF annealed c-HBC, where the representative peaks are in accord with previously found new c-HBC polymorph II crystals.<sup>34</sup> In contrast, the c-HBC sample subjected to subsequent thermal annealing (at 330 °C) shows the signature of the polymorph II' phase without any observation of chemical structural change of c-HBC. The enhanced reflections at  $q = 0.95$   $\text{\AA}^{-1}$  and decreased peaks at both  $q = 1.04$  and  $q = 1.15$   $\text{\AA}^{-1}$  reveal the transformation of c-HBC from polymorph II and polymorph II'.

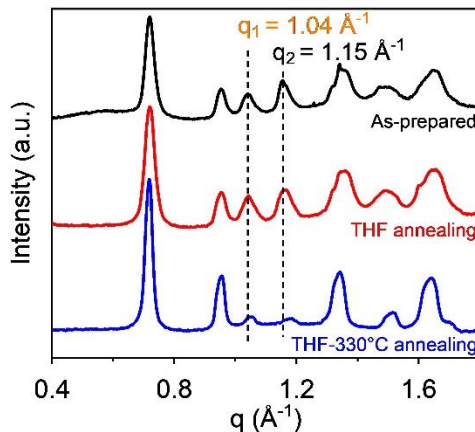


**Figure 2.2** 1D diffraction traces for the sample series with as-prepared (black line), THF-annealed (red line), and THF-330 °C annealed (blue line) c-HBC films. Significantly decreased peaks at both  $q_1 = 1.04$  and  $q_2 = 1.15$   $\text{\AA}^{-1}$  indicate the phase transformation of c-HBC from polymorph II to polymorph II'. Reproduced from ref. 1 with permission from The Royal Society of Chemistry, copyright 2018.

Although we successfully developed polymorph II' in a c-HBC anode via THF and thermal annealing treatments, the exact space group of the polymorph II' phase remains elusive, mainly because of the difficulty of growing single c-HBC crystals for X-ray diffraction (XRD) analysis. In order to trace the space group of the polymorph II' phase, we performed an in-depth computational polymorphism study using Monte Carlo simulated annealing combined with clustering and geometry optimization. The XRD pattern analysis, in combination with in silico polymorph screening, revealed that the experimental powder XRD pattern of the polymorph II' phase of c-HBC (**Figure 2.3**, black line) exactly matched that of the  $R\bar{3}$  space group (**Figure 2.3**, blue line). The main diffraction peaks of the experimental powder XRD pattern, located at  $10.14^\circ$ ,  $13.40^\circ$ ,  $19.08^\circ$ ,  $21.28^\circ$ ,  $23.24^\circ$ ,  $23.98^\circ$ , and  $26.54^\circ$ , corresponding to a scattering vector  $q$  of  $0.72$ ,  $0.95$ ,  $1.35$ ,  $1.51$ ,  $1.64$ ,  $1.69$ , and  $1.87 \text{ \AA}^{-1}$ , were assigned to the (101), (110), (003), (211),  $(11\bar{3})$ ,  $(21\bar{2})$ , and (104) planes, respectively. The Rietveld refinement result (**Figure 2.3**, red line) was found in good agreement with the experimental XRD pattern (**Figure 2.3**, black line), as evidenced by their negligible difference (**Figure 2.3**, green line) and the low final residual factors (4.20% for  $R_p$  and 6.74% for  $R_{wp}$ ). The Rietveld refinement suggests a trigonal crystal system with lattice parameters of  $a = 13.24 \text{ \AA}$ ,  $b = 13.24 \text{ \AA}$ , and  $c = 13.93 \text{ \AA}$  and  $\alpha = 90^\circ$ ,  $\beta = 90^\circ$ , and  $\gamma = 120^\circ$  for the unit cell with the  $R\bar{3}$  space group. The resulting GIXD and computational investigation allowed us to conclude that the polymorph II' phase of the c-HBC anode belongs to the trigonal  $R\bar{3}$  space group, where c-HBC molecules have ABC stacking configuration, an interlayer distance of  $4.64 \text{ \AA}$ , and consistent molecular orientation (**Figure 2.4**).

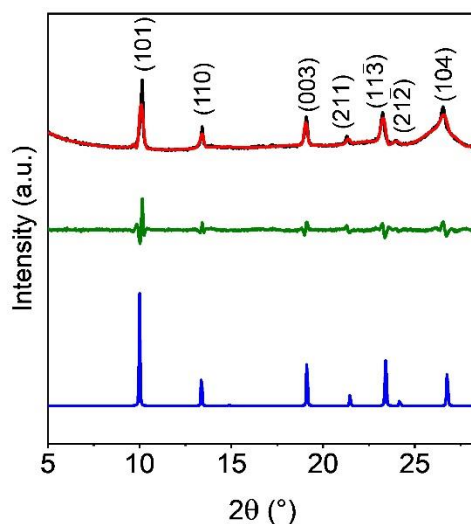


**Figure 2.3** XRD patterns of c-HBC: experimental as-prepared (gray line), THF-330 °C annealed (black line), Rietveld refined (red line), their difference (green line), and the  $R\bar{3}$  crystal phase (blue line). Reproduced from ref. 1 with permission from The Royal Society of Chemistry, copyright 2018.



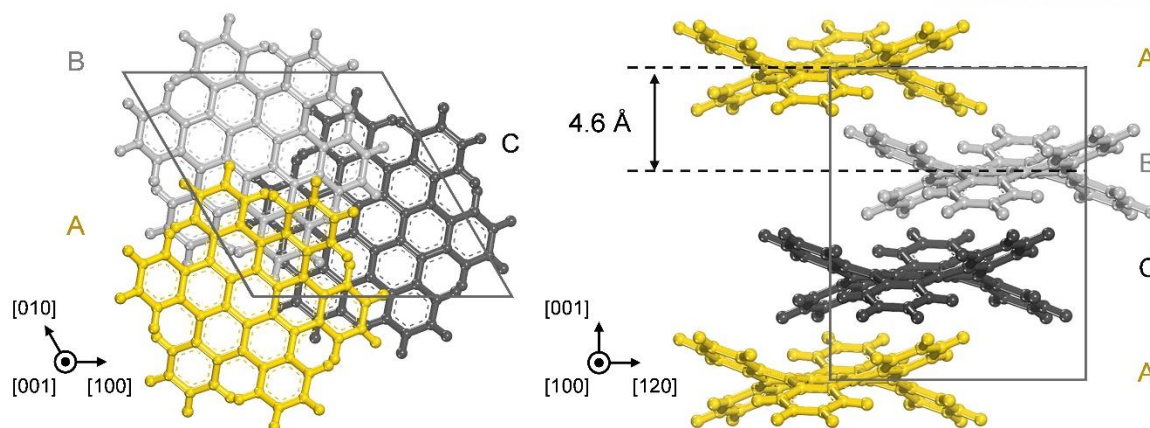


**Figure 2.4** Projection views of the  $R\bar{3}$  crystal phase along  $[001]$  and  $[100]$  directions, respectively. For clarity, the c-HBC molecules in different layers are represented by yellow, light gray, and dark gray colors. Reproduced from ref. 1 with permission from The Royal Society of Chemistry, copyright 2018.

The powder XRD and GIXD patterns of polymorph II showed enhanced reflections at  $q = 1.04 \text{ \AA}^{-1}$  and  $q = 1.15 \text{ \AA}^{-1}$  and a decreased peak at  $q = 0.95 \text{ \AA}^{-1}$ , compared with polymorph II', the  $R\bar{3}$  crystal phase. Except for the differences in the relative intensities of the three peaks, the powder XRD and GIXD patterns between the polymorph II and  $R\bar{3}$  crystal phases were remarkably similar. Therefore, we considered that polymorph II also belongs to the trigonal crystal system but with larger lattice parameters and different intermolecular packing. The polymorph II crystal structure was solved using the Reflex program. The parallel tempering algorithm was used with the close contact penalty. As shown in **Figure 2.5**, the  $P3_1$  and  $P3_2$  crystal phases exhibit the greatest similarities in the XRD patterns, with enhanced reflections at  $q = 1.04 \text{ \AA}^{-1}$  while retaining the remaining major peaks. The crystal structures of  $P3_1$  and  $P3_2$  are similar to  $R\bar{3}$  in that three c-HBC molecules are stacked in a hexagonal lattice according to the ABC sequence and oriented in the same direction (**Figure 2.6**). The only difference is that the c-HBC molecules of the  $P3_1$  and  $P3_2$  crystal phases are slightly shifted and rotated, which makes the crystal structures metastable and transformed into the  $R\bar{3}$  crystal phase after geometry optimization. Even though we confirmed that the different intermolecular stacking enhanced the reflection at  $q = 1.04 \text{ \AA}^{-1}$  the crystal structure, which could accurately represent polymorph II, was not identified among the crystal structures solved by the experimental powder XRD pattern and those obtained by polymorph prediction.



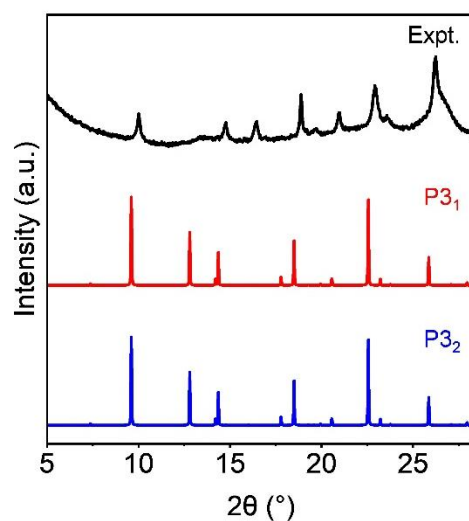


**Figure 2.5** XRD patterns of polymorph II, P3<sub>1</sub>, and P3<sub>2</sub> crystal phases. Reproduced from ref. 1 with permission from The Royal Society of Chemistry, copyright 2018.

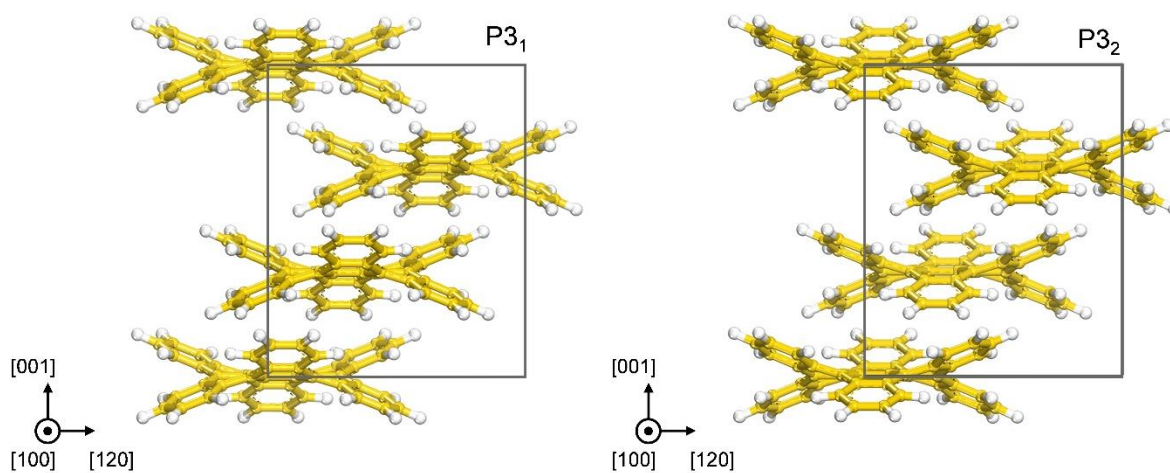


**Figure 2.6** Projection views of P3<sub>1</sub> and P3<sub>2</sub> crystal phases along [100] directions. Reproduced from ref. 1 with permission from The Royal Society of Chemistry, copyright 2018.

In light of the above, we considered the residual Pd impurities, which can be originated from the Pd-catalyzed reactions. Solving the experimental XRD patterns with additional Pd atoms clearly disclosed that the experimental XRD pattern of the polymorph II phase of cHBC (**Figure 2.7**, black line) matched exactly the XRD pattern of P3<sub>1</sub> and P3<sub>2</sub> with inserted Pd atoms (**Figure 2.7**, blue line). The Rietveld refinement result (**Figure 2.7**, red line) was found in good agreement with the experimental XRD pattern (**Figure 2.7**, black line), as reflected by the negligible differences (**Figure 2.7**, green line) and the low final residual factors ( $R_p = 3.17\%$  and  $R_{wp} = 4.57\%$  for P3<sub>1</sub>, and  $R_p = 3.35\%$  and  $R_{wp} = 4.73\%$  for P3<sub>2</sub>). The results showed that the polymorph II crystal structure does not represent pure c-HBC but rather c-HBC with Pd impurities, as shown in **Figure 2.8**.

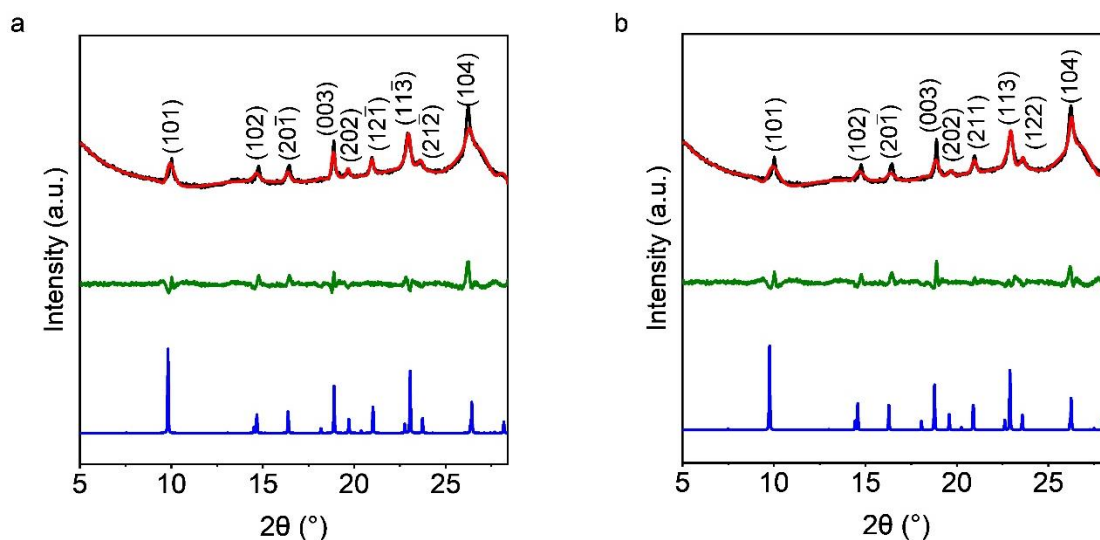


**Figure 2.7** XRD patterns of polymorph II: experimental (black line), Rietveld refined (red line), their difference (green line), and (a) P3<sub>1</sub> and (b) P3<sub>2</sub> crystal phases with Pd atoms (blue line). Reproduced from ref. 1 with permission from The Royal Society of Chemistry, copyright 2018.

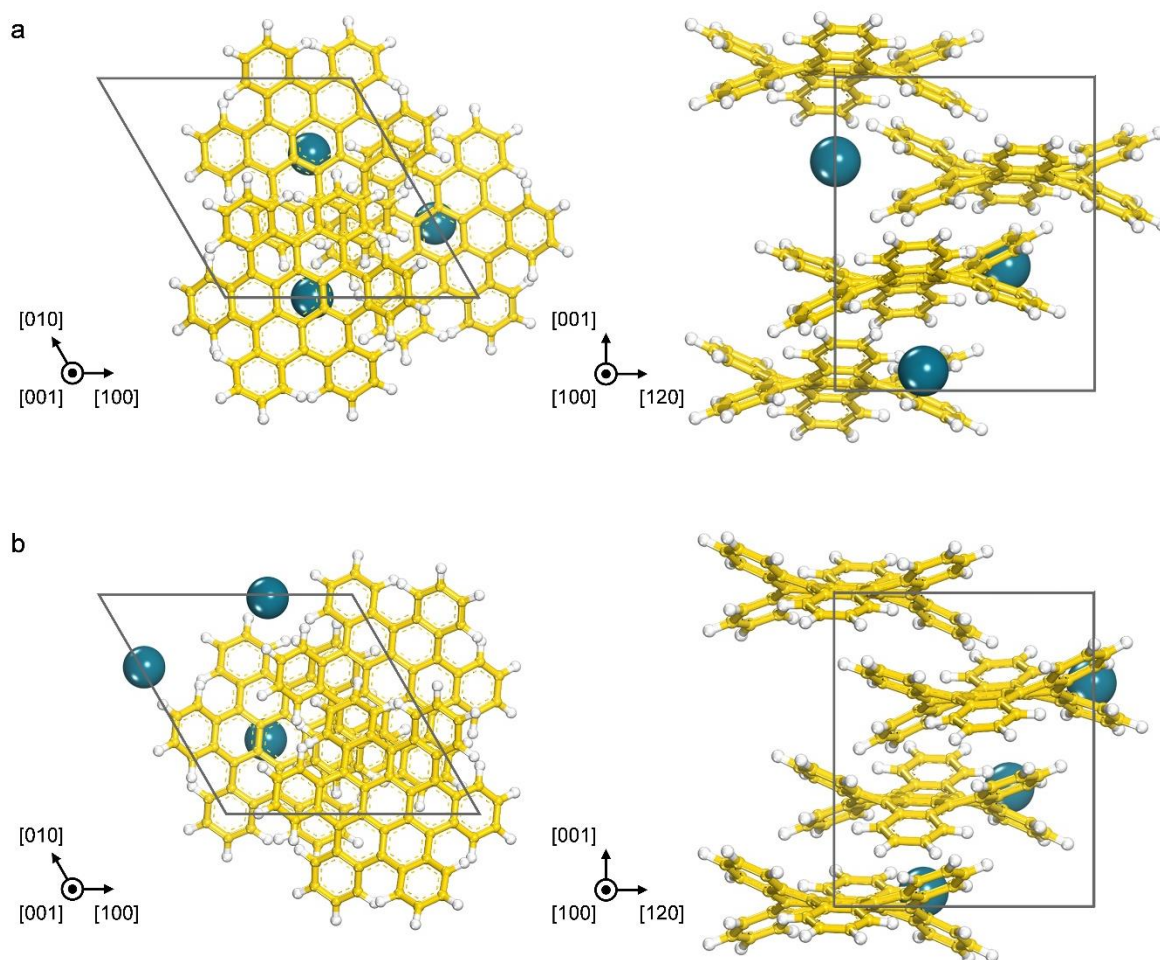


**Figure 2.8** Projection views of (a)  $P3_1$  and (b)  $P3_2$  crystal phases with Pd atoms along  $[001]$  and  $[100]$  directions. Carbon, hydrogen, and palladium are colored yellow, white, and dark cyan, respectively. Reproduced from ref. 1 with permission from The Royal Society of Chemistry, copyright 2018.

### 2.3.2 Lithium Storage Mechanism of c-HBC

The doubly concave molecular structure with bent edge aromatic rings in the stacked c-HBC molecules generates empty pores between the molecules, resulting in the 3D ordering of the pores in the crystal structure (**Figure 2.9**). The free volume of the  $R\bar{3}$  crystal phase of c-HBC, estimated by the Connolly surface using a Li-ion as a probe with a radius of  $0.76 \text{ \AA}$ , was  $0.088 \text{ cm}^3 \text{ g}^{-1}$ , whereas the free volume of graphite was estimated as zero. In addition, the 3D ordered pores of c-HBC enable 3D diffusion of Li-ions, contrary to the 2D diffusion channel of graphite. We hypothesize that the large free volume together with the 3D diffusion channel in c-HBC facilitates the accommodation of Li-ions during insertion.

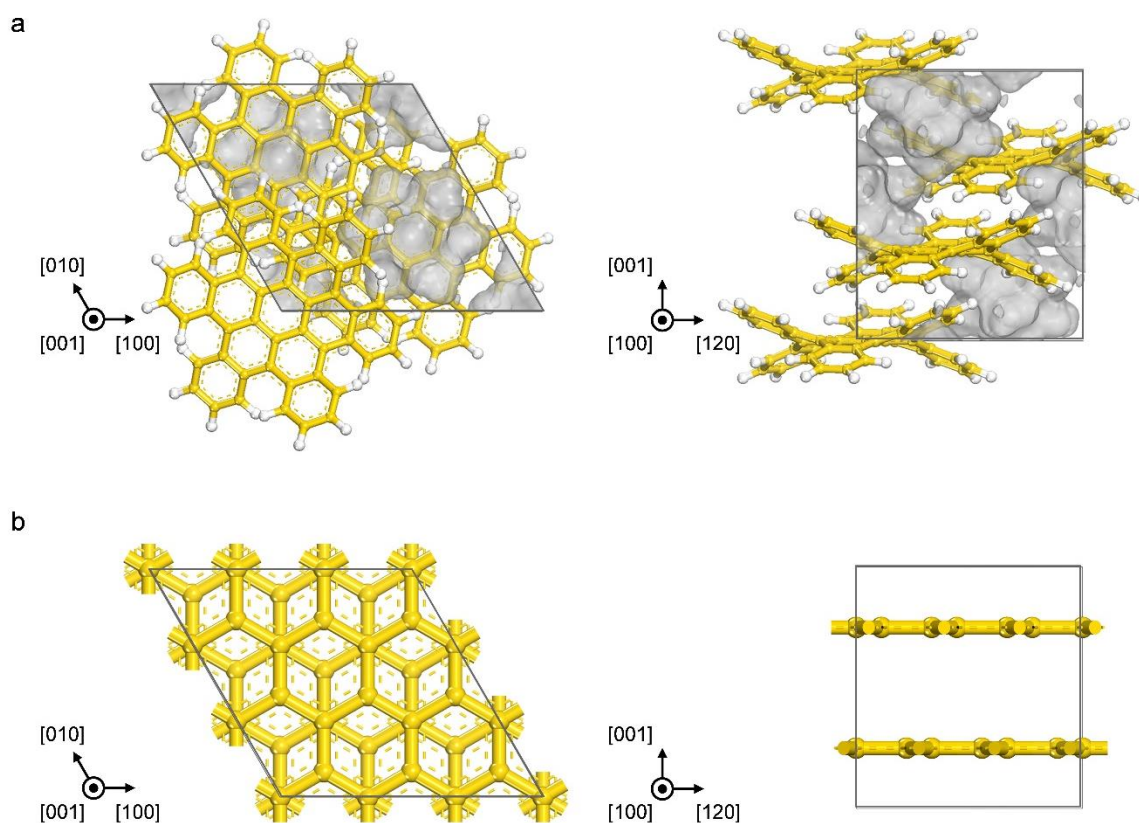


**Figure 2.9** Projection views of (a)  $R\bar{3}$  crystal phase and (b) graphite with Connolly surface along [001] and [100] directions. Carbon and hydrogen are colored yellow and white, respectively. Reproduced from ref. 1 with permission from The Royal Society of Chemistry, copyright 2018.

To explore the Li-ion insertion sites of c-HBC, we performed Monte Carlo simulations in combination with density functional theory calculations. The energetically favorable insertion sites of Li-ions in the  $R\bar{3}$  c-HBC crystal phase was found to be the surface of empty pores. In particular, the Li-inserted c-HBC was found to have the highest stability with the lowest formation energy of  $-5.8$  eV, when a Li-ion was inserted into a pore with a negative electrostatic potential between the bent edge aromatic rings of the c-HBC molecules, as shown in **Figure 2.10**. In addition, we calculated the formation energy of Li-inserted c-HBC and the voltage profile as a function of Li-ion content. Here, Li-ions were inserted into the unit cell of the  $R\bar{3}$  crystal phase in multiples of three (3, 6, 9, and 18 Li-ions), considering the most energetically favorable insertion sites and crystallographic symmetry, as shown in **Figure 2.11**. **Figure 2.12** shows the formation energies of Li-inserted c-HBC as a function of Li-ion content, where the lowest formation energies for each of the contents of Li-ion form an energy convex hull, as shown by the red line. The energy convex hull shows that the Li-inserted c-HBC starts to become unstable when more than 18 Li-ions are inserted, indicating that the  $R\bar{3}$  crystal structure of c-HBC could store up to 6 Li-ions per molecule. This result is in good agreement with the experimental capacity of  $267 \text{ mA h g}^{-1}$ . Furthermore, the calculated voltage profile with an average value of  $0.26 \text{ V}$  matches that observed experimentally in terms of both the single plateau and the energy involved in the Li-ion insertion process, as shown in **Figure 2.13**. The overall simulation results suggest that lithium insertion into c-HBC occurs in the single-stage process without voltage penalty mainly due to Li-ion insertion into 3D ordered angstrom-scale pores generated by the contorted molecular structure of c-HBC. This behavior is strikingly different from that of the typical multiple-staging effects of graphite anodes and flat-HBC molecule.<sup>49-51</sup>



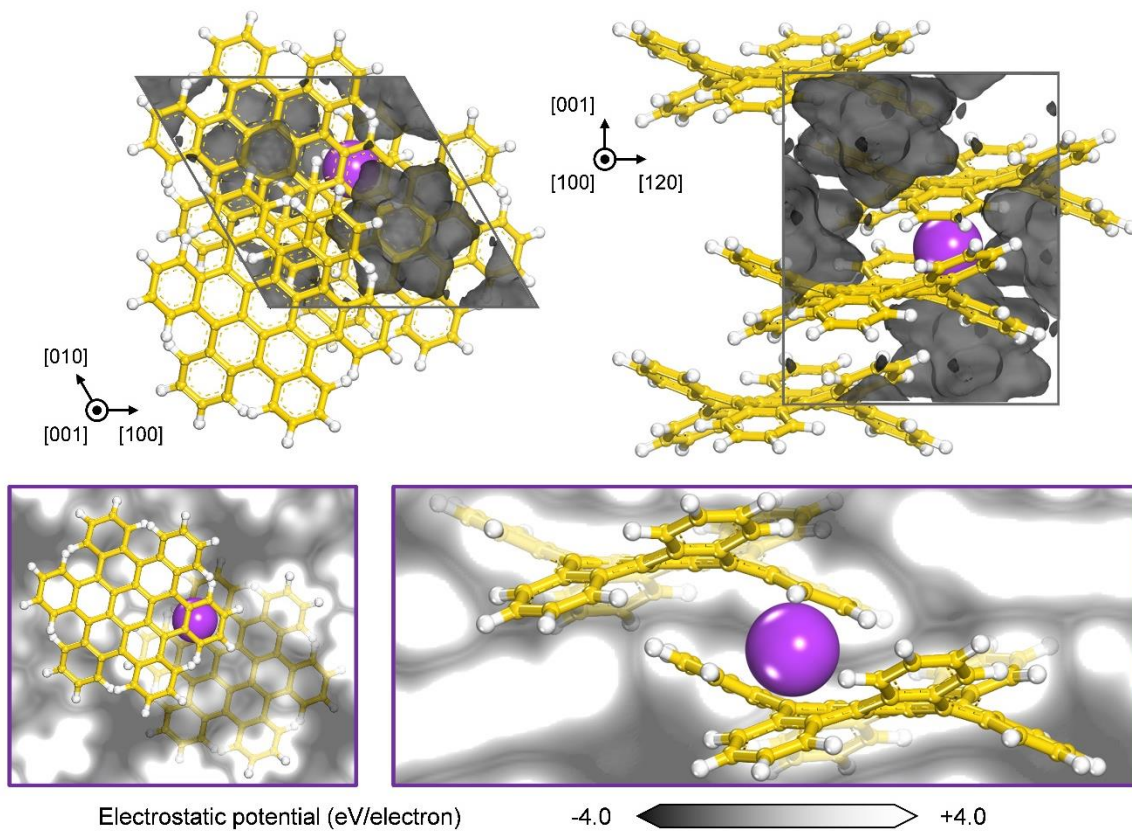


**Figure 2.10** The optimized structure of Li-inserted c-HBC and the electrostatic potential maps of c-HBC without Li-ion. The electrostatic potential is mapped onto the Connolly surface (top) and (001) and (010) planes across the center of Li-ion (bottom left and right). Carbon, hydrogen, and lithium are colored yellow, white, and purple, respectively. Reproduced from ref. 1 with permission from The Royal Society of Chemistry, copyright 2018.

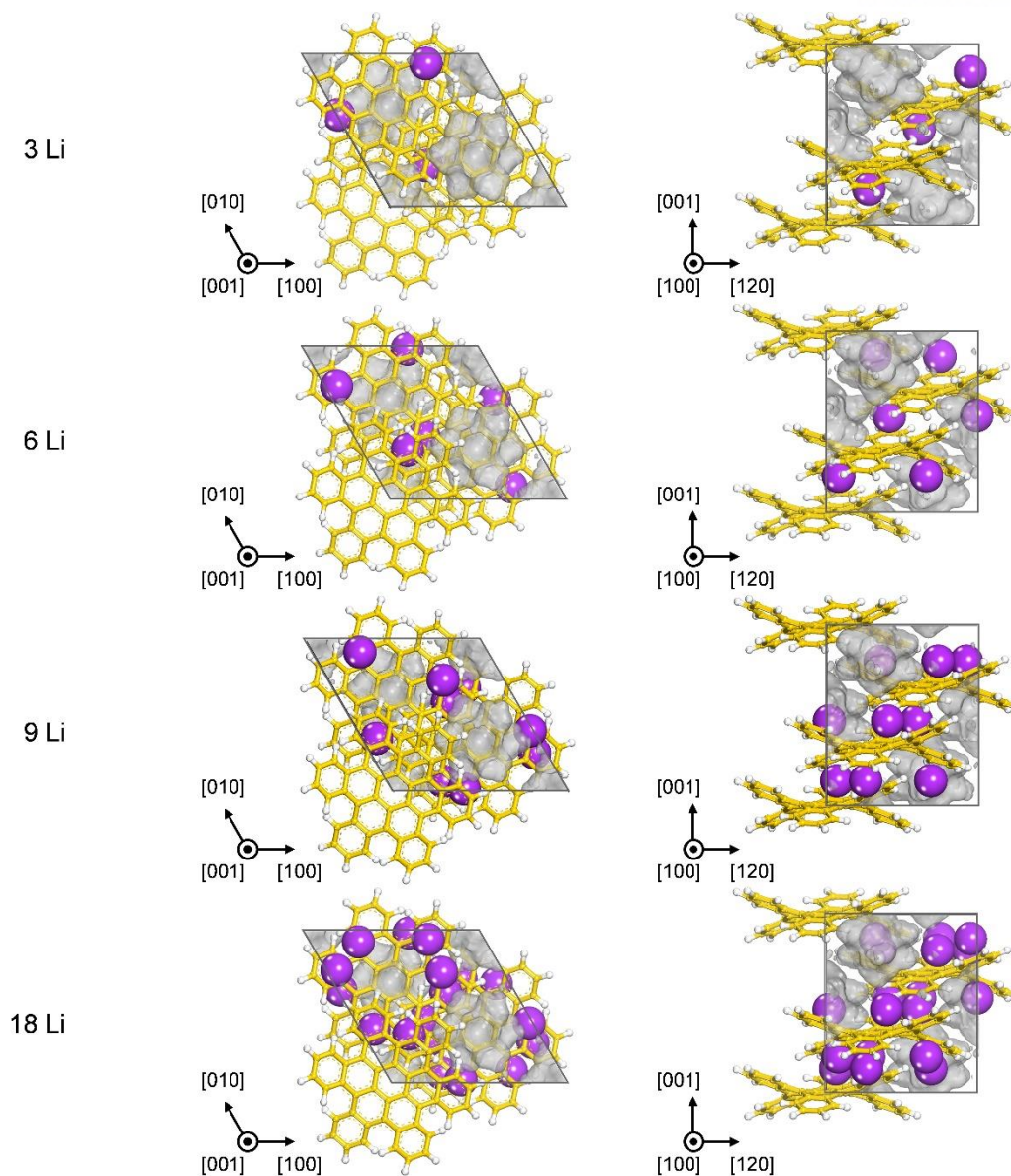


**Figure 2.11** Projection views of the optimized stable structures of 3, 6, 9, and 18 Li-inserted  $R\bar{3}$  crystal phase. Carbon, hydrogen, and lithium are colored yellow, white, and purple, respectively. Reproduced from ref. 1 with permission from The Royal Society of Chemistry, copyright 2018.

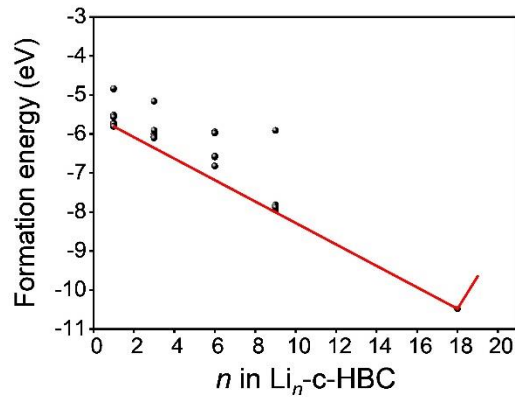


**Figure 2.12** Formation energies of Li-inserted c-HBC as a function of the number of Li-ions. The calculated convex hull is shown as a red line. Reproduced from ref. 1 with permission from The Royal Society of Chemistry, copyright 2018.

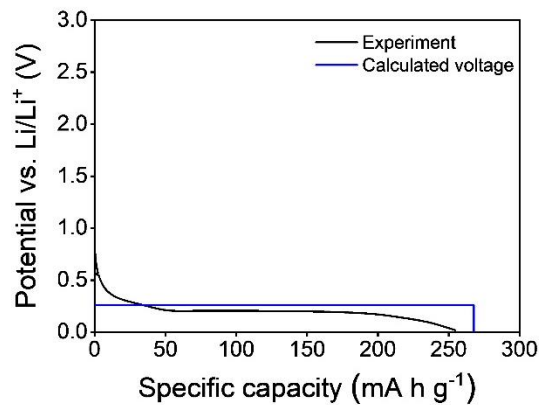


**Figure 2.13** The experimental (black line) and calculated (red and blue lines) voltage profiles. Reproduced from ref. 1 with permission from The Royal Society of Chemistry, copyright 2018.



## 2.4 Conclusion

In summary, the present work demonstrated that a new type of contorted polycyclic aromatic hydrocarbon molecule could find application as an emerging organic anode material for use in LIB systems. The highly crystalline trigonal  $R\bar{3}$  phase of semiconducting c-HBC was confirmed by careful analysis of computational polymorphism study. Moreover, DFT calculations on lithium storage mechanism revealed that c-HBC anode exhibited single-step Li-ion insertion behavior without voltage penalty, primarily because of the unique crystallography of the contorted molecules. These promising results suggest that contorted anode materials could open up new opportunities in the field of next-generation organic anodes.

## 2.5 References

1. Park, J.; Lee, C. W.; Joo, S. H.; Park, J. H.; Hwang, C.; Song, H.-K.; Park, Y. S.; Kwak, S. K.; Ahn, S.; Kang, S. J., Contorted polycyclic aromatic hydrocarbon: promising Li insertion organic anode. *Journal of Materials Chemistry A* **2018**, *6* (26), 12589-12597.
2. Winter, M.; Besenhard, J. O.; Spahr, M. E.; Novák, P., Insertion Electrode Materials for Rechargeable Lithium Batteries. *Advanced Materials* **1998**, *10* (10), 725-763.
3. Kaskhedikar, N. A.; Maier, J., Lithium Storage in Carbon Nanostructures. *Advanced Materials* **2009**, *21* (25-26), 2664-2680.
4. Nishi, Y., The development of lithium ion secondary batteries. *The Chemical Record* **2001**, *1* (5), 406-413.
5. Whittingham, M. S., Lithium Batteries and Cathode Materials. *Chemical Reviews* **2004**, *104* (10), 4271-4302.
6. Nitta, N.; Wu, F.; Lee, J. T.; Yushin, G., Li-ion battery materials: present and future. *Materials Today* **2015**, *18* (5), 252-264.
7. Bruce, P. G.; Freunberger, S. A.; Hardwick, L. J.; Tarascon, J.-M., Li-O<sub>2</sub> and Li-S batteries with high energy storage. *Nature Materials* **2012**, *11* (1), 19-29.
8. Hartmann, P.; Bender, C. L.; Vračar, M.; Dürer, A. K.; Garsuch, A.; Janek, J.; Adelhelm, P., A rechargeable room-temperature sodium superoxide (NaO<sub>2</sub>) battery. *Nature Materials* **2013**, *12* (3), 228-232.
9. Goriparti, S.; Miele, E.; De Angelis, F.; Di Fabrizio, E.; Proietti Zaccaria, R.; Capiglia, C., Review on recent progress of nanostructured anode materials for Li-ion batteries. *Journal of Power Sources* **2014**, *257*, 421-443.
10. Taberna, P. L.; Mitra, S.; Poizot, P.; Simon, P.; Tarascon, J. M., High rate capabilities Fe<sub>3</sub>O<sub>4</sub>-based Cu nano-architected electrodes for lithium-ion battery applications. *Nature Materials* **2006**, *5* (7), 567-573.
11. Poizot, P.; Laruelle, S.; Grugeon, S.; Dupont, L.; Tarascon, J. M., Nano-sized transition-metal oxides as negative-electrode materials for lithium-ion batteries. *Nature* **2000**, *407* (6803), 496-499.
12. Liang, J.; Hu, H.; Park, H.; Xiao, C.; Ding, S.; Paik, U.; Lou, X. W., Construction of hybrid bowl-like structures by anchoring NiO nanosheets on flat carbon hollow particles with enhanced lithium storage properties. *Energy & Environmental Science* **2015**, *8* (6), 1707-1711.
13. Wang, H.; Cui, L.-F.; Yang, Y.; Sanchez Casalongue, H.; Robinson, J. T.; Liang, Y.; Cui, Y.; Dai, H., Mn<sub>3</sub>O<sub>4</sub>-Graphene Hybrid as a High-Capacity Anode Material for Lithium Ion

- Batteries. *Journal of the American Chemical Society* **2010**, *132* (40), 13978-13980.
14. Chan, C. K.; Peng, H.; Liu, G.; McIlwrath, K.; Zhang, X. F.; Huggins, R. A.; Cui, Y., High-performance lithium battery anodes using silicon nanowires. *Nature Nanotechnology* **2008**, *3* (1), 31-35.
  15. He, M.; Kravchyk, K.; Walter, M.; Kovalenko, M. V., Monodisperse Antimony Nanocrystals for High-Rate Li-ion and Na-ion Battery Anodes: Nano versus Bulk. *Nano Letters* **2014**, *14* (3), 1255-1262.
  16. Zhao, Y.; Manthiram, A., High-Capacity, High-Rate Bi-Sb Alloy Anodes for Lithium-Ion and Sodium-Ion Batteries. *Chemistry of Materials* **2015**, *27* (8), 3096-3101.
  17. Idota, Y.; Kubota, T.; Matsufuji, A.; Maekawa, Y.; Miyasaka, T., Tin-Based Amorphous Oxide: A High-Capacity Lithium-Ion-Storage Material. *Science* **1997**, *276* (5317), 1395-1397.
  18. Li, H.; Balaya, P.; Maier, J., Li-Storage via Heterogeneous Reaction in Selected Binary Metal Fluorides and Oxides. *Journal of The Electrochemical Society* **2004**, *151* (11), A1878.
  19. Yoo, E.; Kim, J.; Hosono, E.; Zhou, H.-s.; Kudo, T.; Honma, I., Large Reversible Li Storage of Graphene Nanosheet Families for Use in Rechargeable Lithium Ion Batteries. *Nano Letters* **2008**, *8* (8), 2277-2282.
  20. Masarapu, C.; Subramanian, V.; Zhu, H.; Wei, B., Long-Cycle Electrochemical Behavior of Multiwall Carbon Nanotubes Synthesized on Stainless Steel in Li Ion Batteries. *Advanced Functional Materials* **2009**, *19* (7), 1008-1014.
  21. Dahn, J. R.; Zheng, T.; Liu, Y.; Xue, J. S., Mechanisms for Lithium Insertion in Carbonaceous Materials. *Science* **1995**, *270* (5236), 590-593.
  22. Wu, Z.-S.; Ren, W.; Xu, L.; Li, F.; Cheng, H.-M., Doped Graphene Sheets As Anode Materials with Superhigh Rate and Large Capacity for Lithium Ion Batteries. *ACS Nano* **2011**, *5* (7), 5463-5471.
  23. Zhou, X.; Wan, L.-J.; Guo, Y.-G., Binding SnO<sub>2</sub> Nanocrystals in Nitrogen-Doped Graphene Sheets as Anode Materials for Lithium-Ion Batteries. *Advanced Materials* **2013**, *25* (15), 2152-2157.
  24. Zhang, C.; Mahmood, N.; Yin, H.; Liu, F.; Hou, Y., Synthesis of Phosphorus-Doped Graphene and its Multifunctional Applications for Oxygen Reduction Reaction and Lithium Ion Batteries. *Advanced Materials* **2013**, *25* (35), 4932-4937.
  25. Jeon, I.-Y.; Ju, M. J.; Xu, J.; Choi, H.-J.; Seo, J.-M.; Kim, M.-J.; Choi, I. T.; Kim, H. M.; Kim, J. C.; Lee, J.-J.; Liu, H. K.; Kim, H. K.; Dou, S.; Dai, L.; Baek, J.-B., Edge-Fluorinated Graphene Nanoplatelets as High Performance Electrodes for Dye-Sensitized Solar Cells and Lithium Ion Batteries. *Advanced Functional Materials* **2015**, *25* (8), 1170-1179.

26. Novoselov, K. S.; Fal'ko, V. I.; Colombo, L.; Gellert, P. R.; Schwab, M. G.; Kim, K., A roadmap for graphene. *Nature* **2012**, *490* (7419), 192-200.
27. Xie, J.; Zhang, Q., Recent progress in rechargeable lithium batteries with organic materials as promising electrodes. *Journal of Materials Chemistry A* **2016**, *4* (19), 7091-7106.
28. Nokami, T.; Matsuo, T.; Inatomi, Y.; Hojo, N.; Tsukagoshi, T.; Yoshizawa, H.; Shimizu, A.; Kuramoto, H.; Komae, K.; Tsuyama, H.; Yoshida, J.-i., Polymer-Bound Pyrene-4,5,9,10-tetraone for Fast-Charge and -Discharge Lithium-Ion Batteries with High Capacity. *Journal of the American Chemical Society* **2012**, *134* (48), 19694-19700.
29. Armand, M.; Grugeon, S.; Vezin, H.; Laruelle, S.; Ribière, P.; Poizot, P.; Tarascon, J. M., Conjugated dicarboxylate anodes for Li-ion batteries. *Nature Materials* **2009**, *8* (2), 120-125.
30. Qie, L.; Chen, W.-M.; Wang, Z.-H.; Shao, Q.-G.; Li, X.; Yuan, L.-X.; Hu, X.-L.; Zhang, W.-X.; Huang, Y.-H., Nitrogen-Doped Porous Carbon Nanofiber Webs as Anodes for Lithium Ion Batteries with a Superhigh Capacity and Rate Capability. *Advanced Materials* **2012**, *24* (15), 2047-2050.
31. Lee, H. H.; Park, Y.; Kim, S. H.; Yeon, S.-H.; Kwak, S. K.; Lee, K. T.; Hong, S. Y., Mechanistic Studies of Transition Metal-Terephthalate Coordination Complexes upon Electrochemical Lithiation and Delithiation. *Advanced Functional Materials* **2015**, *25* (30), 4859-4866.
32. Han, X.; Chang, C.; Yuan, L.; Sun, T.; Sun, J., Aromatic Carbonyl Derivative Polymers as High-Performance Li-Ion Storage Materials. *Advanced Materials* **2007**, *19* (12), 1616-1621.
33. Xiao, S.; Myers, M.; Miao, Q.; Sanaur, S.; Pang, K.; Steigerwald, M. L.; Nuckolls, C., Molecular Wires from Contorted Aromatic Compounds. *Angewandte Chemie International Edition* **2005**, *44* (45), 7390-7394.
34. Hiszpanski, A. M.; Baur, R. M.; Kim, B.; Tremblay, N. J.; Nuckolls, C.; Woll, A. R.; Loo, Y.-L., Tuning Polymorphism and Orientation in Organic Semiconductor Thin Films via Post-deposition Processing. *Journal of the American Chemical Society* **2014**, *136* (44), 15749-15756.
35. Ball, M.; Zhong, Y.; Wu, Y.; Schenck, C.; Ng, F.; Steigerwald, M.; Xiao, S.; Nuckolls, C., Contorted Polycyclic Aromatics. *Accounts of Chemical Research* **2015**, *48* (2), 267-276.
36. Tremblay, N. J.; Gorodetsky, A. A.; Cox, M. P.; Schiros, T.; Kim, B.; Steiner, R.; Bullard, Z.; Sattler, A.; So, W.-Y.; Itoh, Y.; Toney, M. F.; Ogasawara, H.; Ramirez, A. P.; Kymissis, I.; Steigerwald, M. L.; Nuckolls, C., Photovoltaic Universal Joints: Ball-and-Socket Interfaces in Molecular Photovoltaic Cells. *ChemPhysChem* **2010**, *11* (4), 799-803.
37. *Materials Studio*.

38. Sun, H.; Jin, Z.; Yang, C.; Akkermans, R. L.; Robertson, S. H.; Spenley, N. A.; Miller, S.; Todd, S. M., COMPASS II: extended coverage for polymer and drug-like molecule databases. *J Mol Model* **2016**, *22* (2), 47.
39. Ewald, P. P., Die Berechnung optischer und elektrostatischer Gitterpotentiale. *Annalen der Physik* **1921**, *369* (3), 253-287.
40. Tosi, M. P., Cohesion of Ionic Solids in the Born Model\*\*Based on work performed under the auspices of the U.S. Atomic Energy Commission. In *Solid State Physics*, Seitz, F.; Turnbull, D., Eds. Academic Press: 1964; Vol. 16, pp 1-120.
41. Mulliken, R. S., Electronic Population Analysis on LCAO–MO Molecular Wave Functions. I. *The Journal of Chemical Physics* **1955**, *23* (10), 1833-1840.
42. Segall, M. D.; Pickard, C. J.; Shah, R.; Payne, M. C., Population analysis in plane wave electronic structure calculations. *Molecular Physics* **1996**, *89* (2), 571-577.
43. Segall, M. D.; Shah, R.; Pickard, C. J.; Payne, M. C., Population analysis of plane-wave electronic structure calculations of bulk materials. *Physical Review B* **1996**, *54* (23), 16317-16320.
44. Clark, S. J.; Segall, M. D.; Pickard, C. J.; Hasnip, P. J.; Probert, M. I. J.; Refson, K.; Payne, M. C., First principles methods using CASTEP. *Zeitschrift für Kristallographie - Crystalline Materials* **2005**, *220* (5-6), 567-570.
45. Perdew, J. P.; Burke, K.; Ernzerhof, M., Generalized Gradient Approximation Made Simple. *Physical Review Letters* **1996**, *77* (18), 3865-3868.
46. Grimme, S., Semiempirical GGA-type density functional constructed with a long-range dispersion correction. *Journal of Computational Chemistry* **2006**, *27* (15), 1787-1799.
47. Monkhorst, H. J.; Pack, J. D., Special points for Brillouin-zone integrations. *Physical Review B* **1976**, *13* (12), 5188-5192.
48. Zhang, Q.; Peng, H.; Zhang, G.; Lu, Q.; Chang, J.; Dong, Y.; Shi, X.; Wei, J., Facile Bottom-Up Synthesis of Coronene-based 3-Fold Symmetrical and Highly Substituted Nanographenes from Simple Aromatics. *Journal of the American Chemical Society* **2014**, *136* (13), 5057-5064.
49. Mukai, K.; Harada, M.; Kikuzawa, Y.; Mori, T.; Sugiyama, J., Electrochemical Properties of Hexa-peri-hexabenzocoronene in Nonaqueous Lithium Cell. *Electrochemical and Solid-State Letters* **2011**, *14* (4), A52.
50. Keil, M.; Samorí, P.; Santos, D. A. d.; Birgerson, J.; Friedlein, R.; Dkhissi, A.; Watson, M.; Müllen, K.; Brédas, J. L.; Rabe, J. P.; Salaneck, W. R., High levels of alkali-metal storage in thin films of hexa-peri- hexabenzocoronene. *The Journal of Chemical Physics* **2002**, *116* (24), 10854-10860.

51. Dahn, J. R., Phase diagram of  $\text{Li}_x\text{C}_6$ . *Physical Review B* **1991**, *44* (17), 9170-9177.

## Chapter 3. Polymorphism and Lithium/Sodium Storage Mechanism of Fluorinated-Contorted Hexabenzocoronene Electrode Material

*This chapter includes the following contents:*

Park, J.<sup>†</sup>; Lee, C. W.<sup>†</sup>; Park, J. H.<sup>†</sup>; Joo, S. H.; Kwak, S. K.\*; Ahn, S.\*; Kang, S. J.\*, Capacitive Organic Anode Based on Fluorinated-Contorted Hexabenzocoronene: Applicable to Lithium-Ion and Sodium-Ion Storage Cells. *Advanced Science* **2018**, 5 (12), 1801365. (†: **equally contributed**). Reproduced with permission from WILEY-VCH Verlag GmbH & Co. KGaA, Weinheim, copyright 2018.<sup>1</sup>

### 3.1 Introduction

With the demand for high-performance electrochemical energy storage, storage cells with high capacities and fast rate capabilities are being studied for next-generation energy-storage systems.<sup>2-6</sup> Although advanced rechargeable batteries have many advantages and are widely used in power applications,<sup>4-6</sup> the classic intercalation mechanism hinders the attainment of high specific capacities during high rate discharge–charge processes, which has led researchers to pursue storage cells with new Li-insertion mechanisms.<sup>7,8</sup> Extreme rate performance has been achieved with supercapacitor-type cells, where the unique electrostatic double-layer capacitor (EDLC) mechanism can fundamentally solve the rate problems and exhibit millisecond discharge–charge times.<sup>3,9-12</sup> Although the positive influence of Helmholtz layers on the electrodes surface can decrease the Li-ion adsorption time, the inherent limited capacities of supercapacitors negate the advantage of their ultrafast discharge–charge times, although much effort have been devoted to alleviating this issue.<sup>10-12</sup>

To satisfy the demand for high energy-storage capacities and discharge–charge rates, pseudocapacitors have attracted interest in the field of electrochemical energy-storage cells.<sup>13-16</sup> Fast redox reactions near the electrode surfaces without bulk phase transformations allow cells to exhibit higher capacitances and rate capabilities than conventional supercapacitors and batteries.<sup>13</sup> After the first observation of pseudocapacitance in RuO<sub>2</sub> anodes,<sup>16</sup> various pseudocapacitive transition metal oxides (e.g., MnO<sub>2</sub>, Fe<sub>2</sub>O<sub>3</sub>, α-MoO<sub>3</sub>, and Nb<sub>2</sub>O<sub>5</sub>) and nanostructured layered metal hydroxides (e.g., Ni(OH)<sub>2</sub> and Co(OH)<sub>2</sub>) have been proposed and meet the requirements for higher specific capacitances.<sup>17-22</sup> However, several major obstacles, such as low conductivities, toxicities of materials, and high weights of metal oxide materials impede their use in pseudocapacitive electrodes.<sup>14,23,24</sup>

As a potential alternative, conjugated polymers are intriguing, as they possess high electrical conductivities and form lightweight electrodes.<sup>25-27</sup> Recently, various organic materials, such as polydopamine-derived electrodes, thiophene-rich conjugated microporous polymers, and conjugated ladder-structured oligomers, have been proposed and revealed their merits in Li- and Na-ion cells.<sup>28-30</sup> In particular, the tunable bandgap between highest occupied molecular orbital (HOMO) and lowest unoccupied molecular orbital (LUMO) accelerates the charge transfer kinetics.<sup>25</sup> Nevertheless, poor cycle ability due to swelling in aprotic solvents is a major limiting factor, requiring an additional process to stabilize the conducting polymers by using recently developed methods, including the deposition of a thin carbonaceous shell of a 3D hierarchical nanostructure of conductive polymer hydrogels (CPHs) or of a Nafion coating.<sup>26, 27, 31, 32</sup> As for the more stable conducting organic materials, our group recently demonstrated that contorted hexabenzocoronene (cHBC) small molecules have potential uses as anode materials for Li-ion batteries (LIBs).<sup>33</sup> A doubly concave conformation of cHBC can increase the *d*-spacing and consequently enhance the discharge and charge rates and achieve superior cycling capabilities in LIBs without significant alterations due to aprotic electrolytes. Furthermore, cHBC shows great potential for achieving control of the HOMO and LUMO levels by doping the heteroatoms in the cHBC.<sup>34</sup> However, capacitive electrodes based on small molecules have been rarely reported for electrochemical energy-storage cells.

Herein, we report the strategic design of fluorinated cHBC (F-cHBC) molecules for possible use as high-capacity and high-rate electrochemical capacitor electrodes. We have chosen the most electronegative fluorine atom to coordinate the exterior aromatic rings to control the HOMO and LUMO energy levels of cHBC. The decreased HOMO–LUMO energy levels of F-cHBC showed a highly crystalline P2<sub>1</sub>/c phase, which permits the development of pseudocapacitor characteristics in half-cell architectures, providing an excellent rate capability. In particular, simulation results indicated that the negative charge of the fluorine atoms in the F-cHBC crystal promotes Li accessibility, which ultimately increases the rate performance during the discharge–charge processes. Furthermore, F-cHBC exhibited superior Na storage performance and long-term stability; these traits suggest that F-cHBC is a potential electrochemical organic electrode for Li<sup>+</sup>- and Na<sup>+</sup>-ion storage cells.



## 3.2 Computational Methods

### 3.2.1 Crystal Structure Prediction

The computational polymorphism study of F-cHBC was carried out using the Polymorph module of the Materials Studio 2018.<sup>35</sup> Using the optimized structure of F-cHBC molecule as input, the ab initio prediction of polymorphs was performed sequentially in six steps (i.e., packing, clustering, geometry optimization, clustering, geometry optimization, and clustering). In the packing step, the crystal structures belonging to a specific space group were sampled using Monte Carlo simulated annealing. The packing procedure was performed for 10 different space groups:  $P2_1/c$ ,  $P\bar{1}$ ,  $P2_12_12_1$ ,  $C2/c$ ,  $P2_1$ ,  $Pbca$ ,  $Pna2_1$ ,  $Cc$ ,  $Pbcn$ , and  $C2$ . To achieve sufficiently wide sampling, we set the maximum temperature to  $1.5 \times 10^5$  K, the minimum temperature to 300 K, the maximum number of steps to  $5.0 \times 10^5$ , the number of steps to accept before cooling to 100, the minimum move factor to  $1.0 \times 10^{-50}$ , and the heating factor to 0.025. In the geometry optimization step, the lattice parameters and atomic positions were relaxed under crystallographic symmetry. The F-cHBC molecule was treated rigid body in the first geometry optimization step, while it was fully relaxed in the second geometry optimization step. The maximum number of steps was set to  $1.0 \times 10^4$  and the convergence criteria were set to  $2.0 \times 10^{-5}$  kcal mol<sup>-1</sup> for the maximum energy change, 0.001 kcal mol<sup>-1</sup> Å<sup>-1</sup> for the maximum force, 0.001 GPa for the maximum stress, and  $1.0 \times 10^{-5}$  Å for the maximum displacement. In the clustering step, many similar structures were grouped into clusters, and the lowest energy structure representing each cluster was filtered. The criterion of crystal similarity measure was set to 0.11, which was calculated based on a comparison of radial distribution functions with a cutoff distance of 7 Å and 140 bins. After the final clustering step, the space group symmetry of the predicted crystal structures was reanalyzed and the in-silico screening was carried out on the basis of XRD comparison. The interatomic interactions were described by COMPASS II force field and calculated using the Ewald summation method.<sup>36-38</sup>

### 3.2.2 Monte Carlo Simulation

To figure out the specific adsorption sites of Li-ions in the crystal structure of F-cHBC, Monte Carlo simulated annealing was performed using the Sorption module of Materials Studio 2018.<sup>35</sup> Based on the metropolis algorithm, the Monte Carlo simulated annealing was carried out with the maximum number of loading steps of  $1.0 \times 10^5$ , the maximum number of production steps of  $1.0 \times 10^8$ , and 40 annealing cycles. All simulations were repeated 5 times independently. The interatomic interactions were described by COMPASS II force field with Mulliken charges obtained by DFT calculations.<sup>36, 39</sup>

### 3.2.3 Density Functional Theory Calculation

To estimate the highest occupied molecular orbital (HOMO) and the lowest unoccupied molecular orbital (LUMO) energy levels of cHBC and F-cHBC molecules, spin-polarized density functional theory (DFT) calculations were conducted using the DMol3 module of the Materials Studio 2018.<sup>35, 40, 41</sup> The Becke's three-parameter hybrid exchange functional combined with the Lee-Yang-Parr correlation functional (B3LYP) was employed for describing the exchange-correlation potential of electrons.<sup>42, 43</sup> The DNP 4.4 basis set was used with a global orbital cutoff of 3.7 Å. The core electrons were explicitly treated as all electrons with relativistic effect. The long-range van der Waals interactions were corrected using the Grimme's method.<sup>44</sup> The self-consistent field calculation was performed with the fixed orbital occupancy, until the convergence criterion of  $1.0 \times 10^{-6}$  was satisfied. The convergence criteria for geometry optimization were set to  $1.0 \times 10^{-5}$  Ha for the maximum energy change, 0.002 Ha Å<sup>-1</sup> for the maximum force, and 0.005 Å for the maximum displacement, respectively.

To study the lithium/sodium storage mechanism, DFT calculations were performed using the CASTEP module of the Materials 2018.<sup>35</sup> The generalized gradient approximation with the Perdew–Burke–Ernzerhof (GGA-PBE) functional was used to describe the exchange correlation potential of the electrons.<sup>45</sup> The interactions between ions and electrons were described by on-the-fly generated ultrasoft pseudopotentials. The plane-wave basis set with a cutoff energy of 840 eV was employed to expand the wave functions. The van der Waals interactions were corrected by Grimme's method.<sup>44</sup> The convergence criterion for self-consistent field calculation was set to  $5.0 \times 10^{-7}$  eV atom<sup>-1</sup>. Lattice parameters and atomic positions were fully relaxed. The convergence criteria for geometry optimization were set to  $5.0 \times 10^{-6}$  eV atom<sup>-1</sup> for the maximum energy change, 0.01 eV Å<sup>-1</sup> for the maximum force, 0.02 GPa for the maximum stress, and  $5.0 \times 10^{-4}$  Å for the maximum displacement. The Brillouin zone was integrated using a  $1 \times 1 \times 1$  *k*-point grid with the Monkhorst–Pack scheme for all calculations.<sup>46</sup> The formation energy ( $E_f$ ) of the Li-ion inserted structure as a function of Li-ion content was calculated as follows:

$$E_f = E_{\text{Li}_n\text{-F-cHBC}} - E_{\text{F-cHBC}} - nE_{\text{Li}}$$

where  $E_{\text{Li}_n\text{-F-cHBC}}$  is the total energy of the F-cHBC crystal with inserted Li-ions,  $n$  is the number of inserted Li-ions,  $E_{\text{F-cHBC}}$  is the total energy of the P2<sub>1</sub>/c crystal phase of F-cHBC, and  $E_{\text{Li}}$  is the total energy per atom of bcc bulk Li. The voltage profile ( $V$ ) as a function of Li-ion content was calculated as follows:

$$V(n) = -\frac{E_{\text{Li}_{n_2}\text{-F-cHBC}} - E_{\text{Li}_{n_1}\text{-F-cHBC}} - (n_2 - n_1)E_{\text{Li}}}{q(n_2 - n_1)}$$

where  $E_{\text{Li}_{n_1}\text{-F-cHBC}}$  and  $E_{\text{Li}_{n_2}\text{-F-cHBC}}$  represent the total energy of the F-cHBC crystal with inserted Li-ions,  $n_1$  and  $n_2$  are the numbers of inserted Li-ions ( $n_2 > n_1$ ),  $E_{\text{Li}}$  is the total energy per atom of bcc bulk Li, and  $q$  is the net charge of Li-ions ( $q = +1e$ ).

### 3.3 Results and Discussion

#### 3.3.1 Polymorphism of F-cHBC

The chemical structures of the cHBC and F-cHBC molecules are shown in **Figure 3.1a**. F-cHBC contains four fluorine atoms at its ends that are thought to change the bandgap of the cHBC molecule.<sup>34, 47</sup> The HOMO and LUMO energy levels of F-cHBC estimated using density functional theory (DFT) calculations confirmed that fluorine substitution causes two degenerate HOMO and LUMO energy levels to split and decrease from  $-5.247$  to  $-5.533$  eV for the HOMO and  $-1.856$  to  $-2.257$  eV for the LUMO (**Figure 3.1b**).

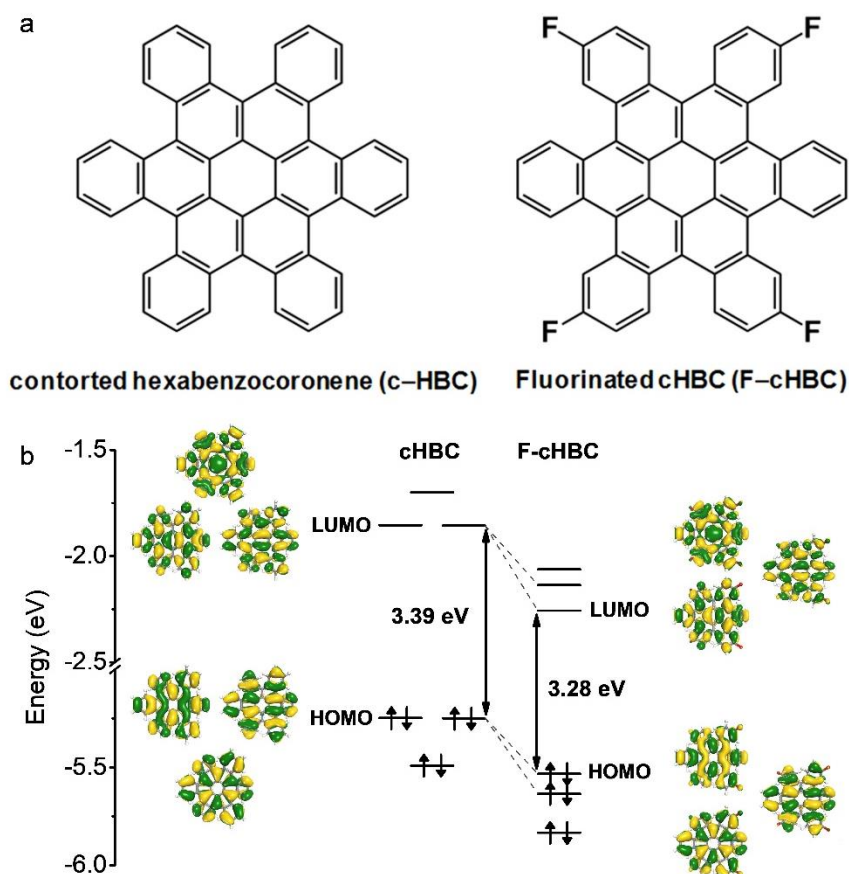


**Figure 3.1** (a) Chemical structures and (b) DFT-calculated energy diagrams of the molecular orbitals of contorted hexabenzocoronene (cHBC) and fluorinated cHBC (F-cHBC). Reproduced from ref. 1 with permission from WILEY-VCH Verlag GmbH & Co. KGaA, Weinheim, copyright 2018.

To examine the crystal phase evolution of the F-cHBC anode on the current collector, in situ grazing incidence wide-angle X-ray scattering (GIWAXS) measurement was experimentally performed on the mixtures of F-cHBC/PVDF (ratio: 90/10 wt%) after the samples had been annealed at temperatures from room temperature to 330 °C. The resulting 1D diffraction traces from the in situ GIWAXS measurements showed a monotonic decrease in the peak at  $q = 0.67 \text{ \AA}^{-1}$  and the formation of a new peak at  $q = 0.49 \text{ \AA}^{-1}$  as the temperature increased (**Figure 3.2**). These trends are attributed to a change in the crystal phase of F-cHBC, because a previous report on fluorinated-cHBC derivatives suggested that a phase change of F-cHBC from polymorph II to polymorph I through thermal treatment is an efficient route for observing the polymorph I phase of polymorphic F-cHBC small molecule.<sup>47</sup>

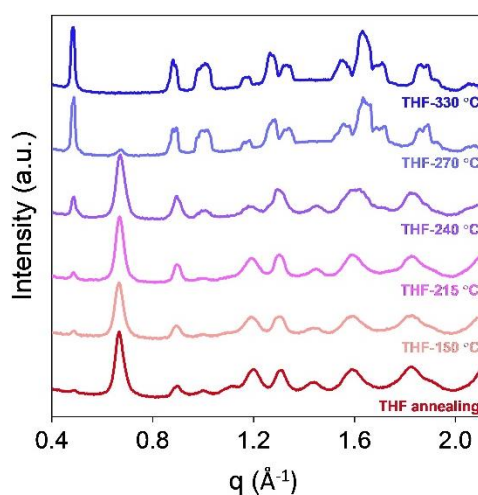


**Figure 3.2** 1D GIWAX diffraction traces from in situ GIWAXS as a function of the annealing temperature. Reproduced from ref. 1 with permission from WILEY-VCH Verlag GmbH & Co. KGaA, Weinheim, copyright 2018.

A Monte Carlo computational study with simulated annealing also suggested that polymorph I of the F-cHBC crystal should develop. The in silico polymorph screening revealed that the experimental X-ray diffraction (XRD) pattern of the polymorph I phase of F-cHBC matched well with the XRD pattern of the  $P2_1/c$  crystal phase (**Figure 3.3**). Prominent peaks at  $7.04^\circ$ ,  $12.68^\circ$ ,  $14.06^\circ$ ,  $14.50^\circ$ ,  $16.66^\circ$ ,  $18.08^\circ$ ,  $18.86^\circ$ ,  $21.84^\circ$ ,  $22.18^\circ$ ,  $23.24^\circ$ , and  $24.10^\circ$  corresponded to the scattering vectors  $q$  of 0.50, 0.90, 1.00, 1.03, 1.18, 1.28, 1.34, 1.55, 1.57, 1.64, and  $1.70 \text{ \AA}^{-1}$  and were assigned to the (100), (011), (200), (111), (012), (112), (211), (212), (020), (120), and  $(12\bar{1})$  planes, respectively. Rietveld refinement results suggested the presence of a  $P2_1/c$  crystal phase with lattice parameters of  $a = 12.62 \text{ \AA}$ ,  $b = 8.04 \text{ \AA}$ ,  $c = 14.22 \text{ \AA}$ ,  $\alpha = 90.00^\circ$ ,  $\beta = 89.89^\circ$ , and  $\gamma = 90.00^\circ$ . From these results, we can determine the phase transformation processing route of F-cHBC. The produced  $P2_1/c$  crystal phase (polymorph I) could be obtained by thermal annealing but could not be reversibly converted to the polymorph II phase. We believe that the obtained crystal phase may be beneficial for facilitating the Li-ion accessibility in aprotic electrolytes because the previously studied cHBC anodes exhibited enhanced electrochemical performances when the crystals had nanopores in the electrolyte.<sup>33</sup>

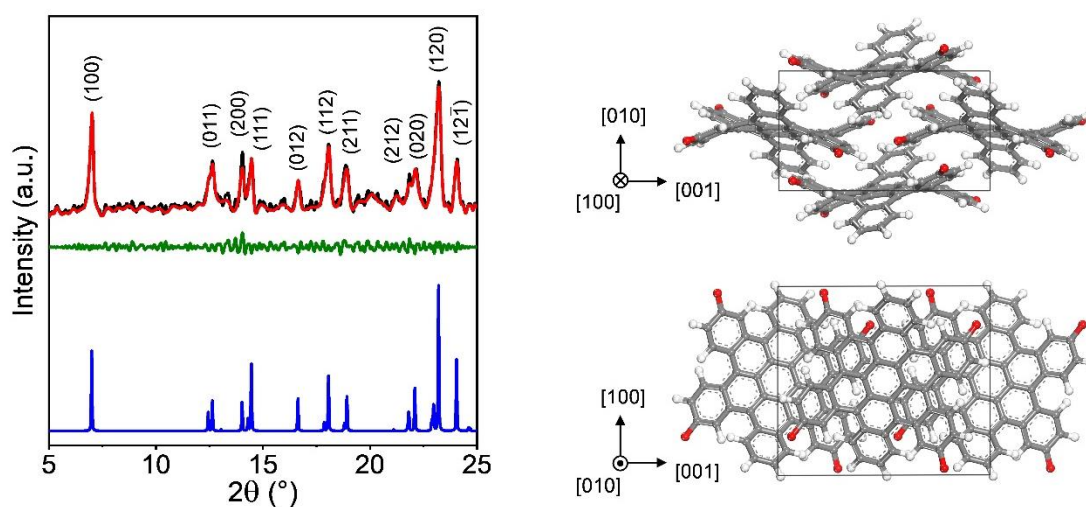


**Figure 3.3** XRD patterns of F-cHBC (left): experimental (black line), Rietveld refined (red line), their difference (green line), and the  $P2_1/c$  crystal phase (blue line) ( $R_{wp} = 13.21 \%$ ,  $R_p = 9.74 \%$ ). Projection views of the  $P2_1/c$  crystal structure along the  $[100]$  (right top) and  $[010]$  (right bottom) directions. Gray: carbon, red: fluorine, white: hydrogen. Reproduced from ref. 1 with permission from WILEY-VCH Verlag GmbH & Co. KGaA, Weinheim, copyright 2018.

### 3.3.2 Lithium Storage Mechanism of F-cHBC

To identify the adsorption sites of Li ions in the  $P2_1/c$  crystal phase of F-cHBC, we examined the 3D space within the crystal structure by using a probe with a radius of 0.76 Å (i.e., the radius of Li ion) to construct the Connolly surface (**Figure 3.4**). The  $P2_1/c$  crystal structure of F-cHBC has empty spaces with a negative electrostatic potential near the fluorine atoms; these spaces may be capable of accommodating and storing Li ions.

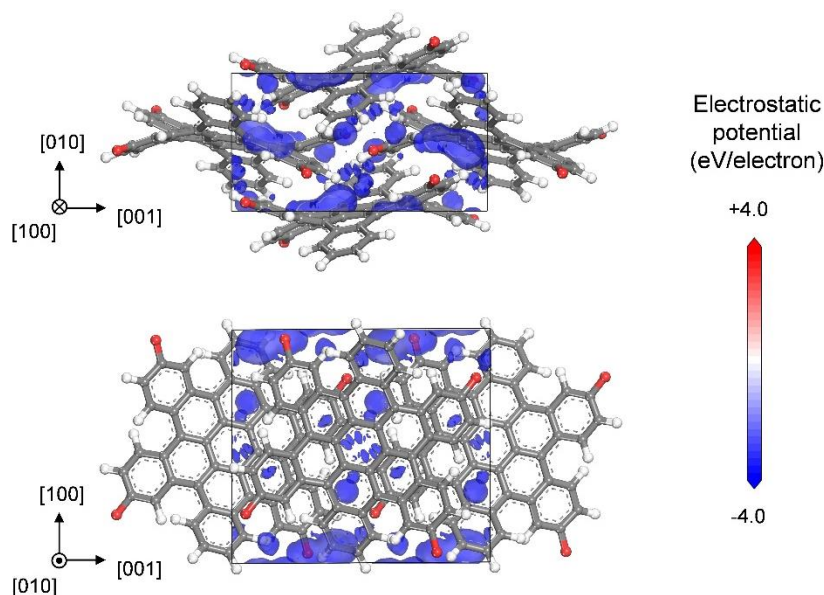


**Figure 3.4** The optimized structure and electrostatic potential maps of F-cHBC. The electrostatic potential is mapped onto the Connolly surface. Carbon, hydrogen, and fluorine are colored grey, white, and red, respectively. Reproduced from ref. 1 with permission from WILEY-VCH Verlag GmbH & Co. KGaA, Weinheim, copyright 2018.

To determine whether the empty spaces are active sites that provide energy-storage capacity, we combined Monte Carlo simulations and DFT calculations. The results suggested that these empty spaces with negative electrostatic potentials are the most stable locations for the Li ions (**Figure 3.5a**). The empty spaces have two distinct sites, denoted as sites I and II. Crystallographic symmetry yields four identical sites of both types in the unit cell of the  $P2_1/c$  crystal phase. All sites I and II are surrounded by electronegative fluorine atoms and a negatively charged bent edge aromatic ring of the F-cHBC molecule (**Figure 3.5b**); the distances between the Li ion and fluorine atom are 2.1 Å at sites I and II, respectively. The distances between the Li ion and the centroid of the bent edge aromatic ring are 2.6 Å at site I and 1.9 Å at site II.



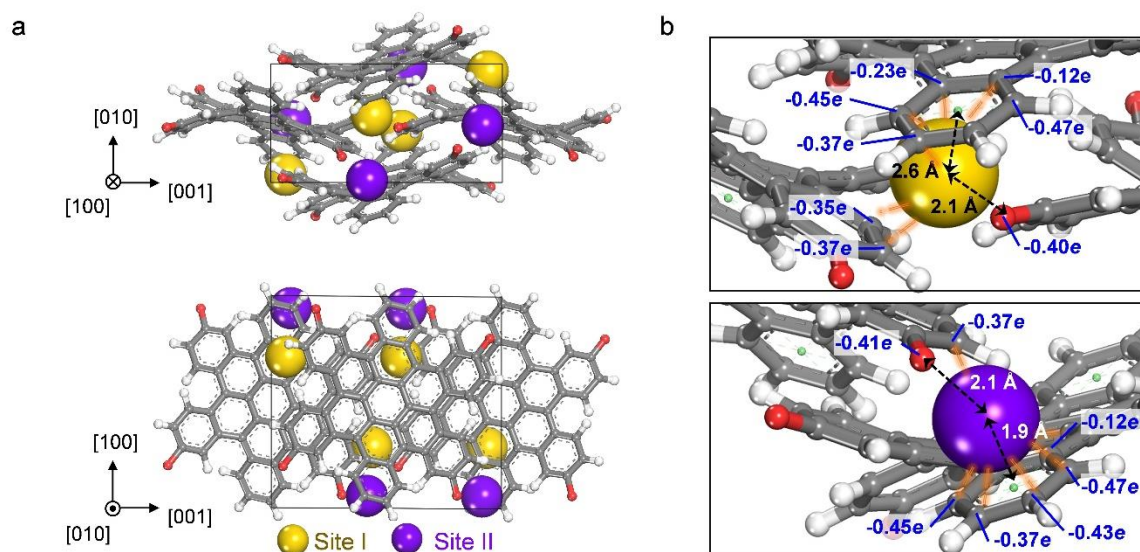


**Figure 3.5** (a) Projection views of the optimized  $P2_1/c$  crystal structure of Li-adsorbed F-cHBC along the [100] (top) and [010] (bottom) directions. Gray: carbon, red: fluorine, white: hydrogen, yellow: lithium at site I, purple: lithium at site II. (b) Magnified view of Li-ion at site I (top) and site II (bottom). Black dotted arrow: distance between Li ion and fluorine or between Li ion and the centroid of the bent edge aromatic ring. Orange line: interaction of adsorbed Li ion with negatively charged atoms. Reproduced from ref. 1 with permission from WILEY-VCH Verlag GmbH & Co. KGaA, Weinheim, copyright 2018.

For the eight total sites identified in the unit cell, we calculated the formation energy ( $E_F$ ) of F-cHBC with  $n$  adsorbed Li ions ( $Li_n$ -F-cHBC) as a function of  $n$  (**Figure 3.6**). The  $E_F$  of  $Li_4$ -F-cHBC was the lowest (i.e.,  $-2.82$  eV) when all the Li ions were located at site I; this result suggests that the Li ions are preferentially located at site I rather than site II (**Figure 3.7**). This may be because Li ions are farther from each other at site I than at site II. Also,  $Li_n$ -F-cHBC was most thermodynamically stable, with the lowest  $E_F$  of  $-4.45$  eV, when sites I and II were fully occupied by eight Li ions (i.e.,  $Li_8$ -F-cHBC). The lowest  $E_F$  for each  $n$  form an energy convex hull (**Figure 3.6**, red line). The  $Li_n$ -F-cHBC begins to become unstable when  $n \geq 9$ ; i.e., each F-cHBC molecule with four fluorine atoms can store up to four Li ions. This result is in good agreement with the experimental capacity (i.e.,  $\approx 160$  mA h  $g^{-1}$  at a current density of 100 mA  $g^{-1}$ ). Furthermore, the calculated voltage profile is consistent with the experimentally observed continuous voltage drop during  $Li^+$  storage (**Figure 3.8**); this similarity supports the hypothesis that Li ions are adsorbed at sites I and II near the fluorine atoms.

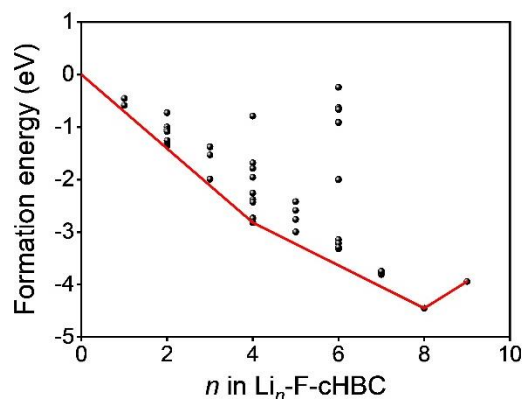


**Figure 3.6** Formation energies of Li-adsorbed F-cHBC as a function of Li-ion content. Red line: convex hull. Reproduced from ref. 1 with permission from WILEY-VCH Verlag GmbH & Co. KGaA, Weinheim, copyright 2018.

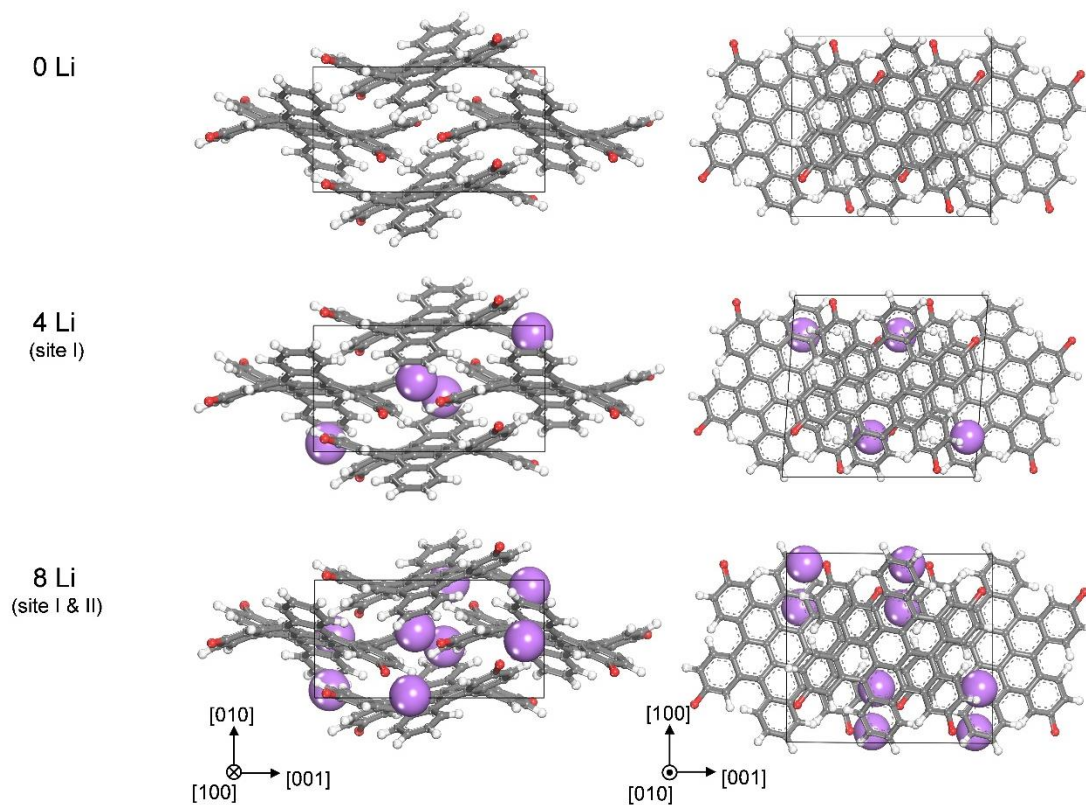


**Figure 3.7** Projection views of the optimized  $P2_1/c$  crystal phase and 4, 8 Li-adsorbed F-cHBC stable structures along the [100] and [010] directions. Carbon, hydrogen, fluorine, and lithium are colored grey, white, red and purple, respectively. Reproduced from ref. 1 with permission from WILEY-VCH Verlag GmbH & Co. KGaA, Weinheim, copyright 2018.

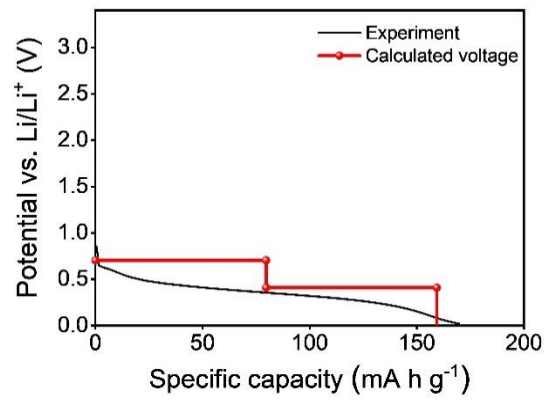


**Figure 3.8** Experimental (black line) and calculated (red line) voltage profiles. Reproduced from ref. 1 with permission from WILEY-VCH Verlag GmbH & Co. KGaA, Weinheim, copyright 2018.

### 3.3.3 Sodium Storage Mechanism of F-cHBC

In addition, the DFT calculation for the Na-ion cell revealed that the adsorption of Na ions at sites I and II is energetically preferred, indicated by the negative EF of F-cHBC with the adsorbed Na ions (**Figure 3.9**). As in the Li-ion case, the Na ions were preferentially located at site I rather than site II. The calculated voltage profile dropped continuously as Na ions were adsorbed; this observation is consistent with the experimental results (**Figure 3.10**).

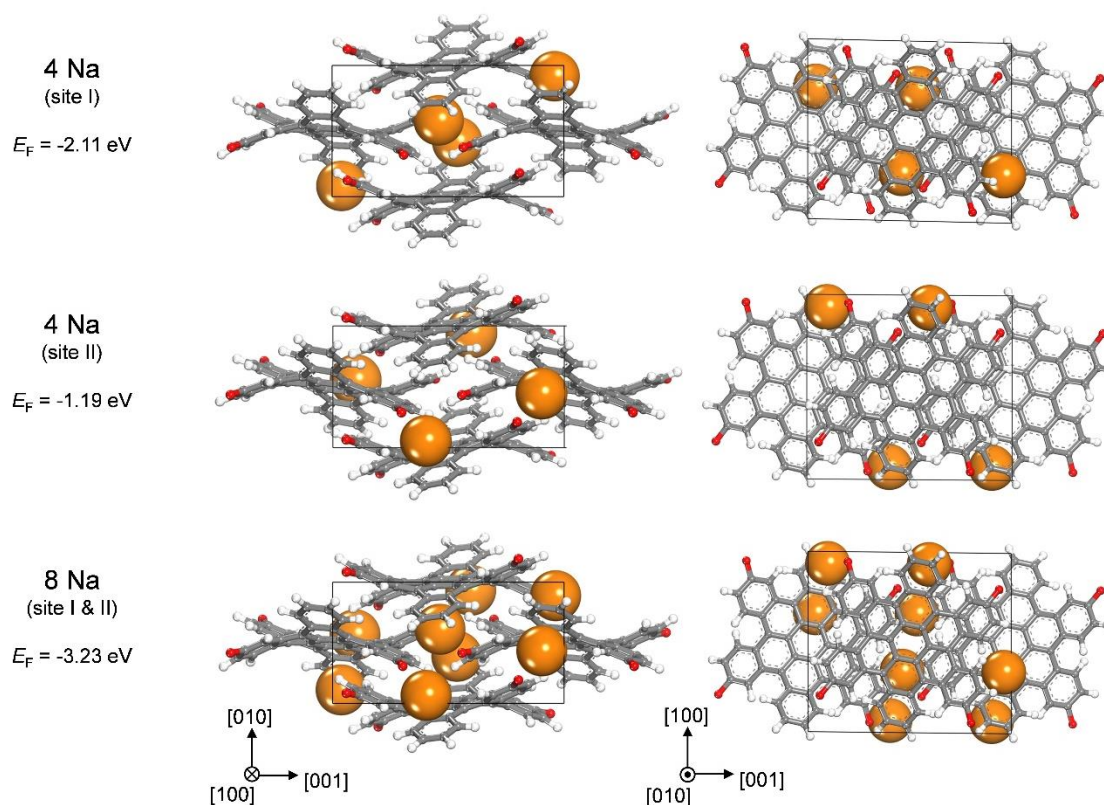


**Figure 3.9** Projection views along the [100] and [010] directions of the F-cHBC structures with 4 and 8 Na-ions adsorbed and their corresponding formation energies. Carbon, hydrogen, fluorine and sodium are colored grey, white, red and orange, respectively. Reproduced from ref. 1 with permission from WILEY-VCH Verlag GmbH & Co. KGaA, Weinheim, copyright 2018.

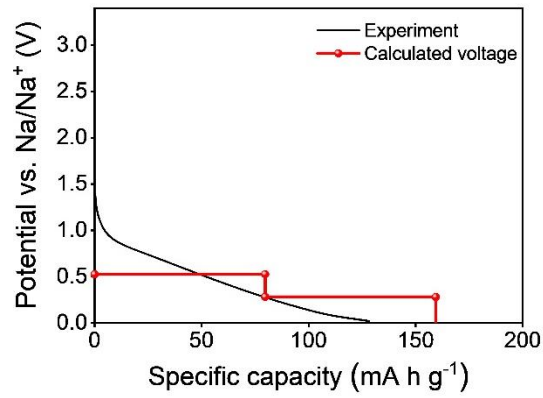


**Figure 3.10** Experimental (black line) and the calculated (red line) voltage profiles. Reproduced from ref. 1 with permission from WILEY-VCH Verlag GmbH & Co. KGaA, Weinheim, copyright 2018.

### 3.4 Conclusion

By fluorinating the cHBC molecule, we achieved capacitive characteristics in a small organic molecule for Li- and Na-ion storage cells. The F-cHBC anode with a controlled crystal phase in the Li-ion cell provided an adequate specific capacity at a high current density. DFT calculations showed that adsorption of Li and Na ions is energetically favorable in the empty space between the fluorine atom of the F-cHBC molecule and the negatively charged bent aromatic ring. Furthermore, F-cHBC electrodes can also be used in Na-ion storage cells. This may result from the capacitive behavior of the F-cHBC anode in the Na-ion cell. More importantly, there are a few materials that can be used in both Li- and Na-ion storage cells. Thus, this unique electrochemical behavior of F-cHBC can provide a new way to develop electrochemical organic capacitive electrodes for alkali-ion storage cells.



### 3.5 References

1. Park, J.; Lee, C. W.; Park, J. H.; Joo, S. H.; Kwak, S. K.; Ahn, S.; Kang, S. J., Capacitive Organic Anode Based on Fluorinated-Contorted Hexabenzocoronene: Applicable to Lithium-Ion and Sodium-Ion Storage Cells. *Advanced Science* **2018**, *5* (12), 1801365.
2. Tarascon, J. M.; Armand, M., Issues and challenges facing rechargeable lithium batteries. *Nature* **2001**, *414* (6861), 359-367.
3. Simon, P.; Gogotsi, Y.; Dunn, B., Where Do Batteries End and Supercapacitors Begin? *Science* **2014**, *343* (6176), 1210-1211.
4. Choi, J. W.; Aurbach, D., Promise and reality of post-lithium-ion batteries with high energy densities. *Nature Reviews Materials* **2016**, *1* (4), 16013.
5. Etacheri, V.; Marom, R.; Elazari, R.; Salitra, G.; Aurbach, D., Challenges in the development of advanced Li-ion batteries: a review. *Energy & Environmental Science* **2011**, *4* (9), 3243-3262.
6. Liu, C.; Li, F.; Ma, L.-P.; Cheng, H.-M., Advanced Materials for Energy Storage. *Advanced Materials* **2010**, *22* (8), E28-E62.
7. Winter, M.; Besenhard, J. O.; Spahr, M. E.; Novák, P., Insertion Electrode Materials for Rechargeable Lithium Batteries. *Advanced Materials* **1998**, *10* (10), 725-763.
8. Dahn, J. R., Phase diagram of  $\text{Li}_x\text{C}_6$ . *Physical Review B* **1991**, *44* (17), 9170-9177.
9. Wang, G.; Zhang, L.; Zhang, J., A review of electrode materials for electrochemical supercapacitors. *Chemical Society Reviews* **2012**, *41* (2), 797-828.
10. Tang, H.; Wang, J.; Yin, H.; Zhao, H.; Wang, D.; Tang, Z., Growth of Polypyrrole Ultrathin Films on  $\text{MoS}_2$  Monolayers as High-Performance Supercapacitor Electrodes. *Advanced Materials* **2015**, *27* (6), 1117-1123.
11. Liu, C.; Yu, Z.; Neff, D.; Zhamu, A.; Jang, B. Z., Graphene-Based Supercapacitor with an Ultrahigh Energy Density. *Nano Letters* **2010**, *10* (12), 4863-4868.
12. Futaba, D. N.; Hata, K.; Yamada, T.; Hiraoka, T.; Hayamizu, Y.; Kakudate, Y.; Tanaike, O.; Hatori, H.; Yumura, M.; Iijima, S., Shape-engineerable and highly densely packed single-walled carbon nanotubes and their application as super-capacitor electrodes. *Nature Materials* **2006**, *5* (12), 987-994.
13. Liu, J.; Wang, J.; Xu, C.; Jiang, H.; Li, C.; Zhang, L.; Lin, J.; Shen, Z. X., Advanced Energy Storage Devices: Basic Principles, Analytical Methods, and Rational Materials Design. *Advanced Science* **2018**, *5* (1), 1700322.
14. Augustyn, V.; Simon, P.; Dunn, B., Pseudocapacitive oxide materials for high-rate



- electrochemical energy storage. *Energy & Environmental Science* **2014**, 7 (5), 1597-1614.
15. Le, Z.; Liu, F.; Nie, P.; Li, X.; Liu, X.; Bian, Z.; Chen, G.; Wu, H. B.; Lu, Y., Pseudocapacitive Sodium Storage in Mesoporous Single-Crystal-like TiO<sub>2</sub>-Graphene Nanocomposite Enables High-Performance Sodium-Ion Capacitors. *ACS Nano* **2017**, 11 (3), 2952-2960.
  16. Trasatti, S.; Buzzanca, G., Ruthenium dioxide: A new interesting electrode material. Solid state structure and electrochemical behaviour. *Journal of Electroanalytical Chemistry and Interfacial Electrochemistry* **1971**, 29 (2), A1-A5.
  17. Toupin, M.; Brousse, T.; Bélanger, D., Charge Storage Mechanism of MnO<sub>2</sub> Electrode Used in Aqueous Electrochemical Capacitor. *Chemistry of Materials* **2004**, 16 (16), 3184-3190.
  18. Sarkar, D.; Khan, G. G.; Singh, A. K.; Mandal, K., High-Performance Pseudocapacitor Electrodes Based on  $\alpha$ -Fe<sub>2</sub>O<sub>3</sub>/MnO<sub>2</sub> Core-Shell Nanowire Heterostructure Arrays. *The Journal of Physical Chemistry C* **2013**, 117 (30), 15523-15531.
  19. Brezesinski, T.; Wang, J.; Tolbert, S. H.; Dunn, B., Ordered mesoporous  $\alpha$ -MoO<sub>3</sub> with iso-oriented nanocrystalline walls for thin-film pseudocapacitors. *Nature Materials* **2010**, 9 (2), 146-151.
  20. Augustyn, V.; Come, J.; Lowe, M. A.; Kim, J. W.; Taberna, P.-L.; Tolbert, S. H.; Abruña, H. D.; Simon, P.; Dunn, B., High-rate electrochemical energy storage through Li<sup>+</sup> intercalation pseudocapacitance. *Nature Materials* **2013**, 12 (6), 518-522.
  21. Wang, H.; Casalongue, H. S.; Liang, Y.; Dai, H., Ni(OH)<sub>2</sub> Nanoplates Grown on Graphene as Advanced Electrochemical Pseudocapacitor Materials. *Journal of the American Chemical Society* **2010**, 132 (21), 7472-7477.
  22. Wang, L.; Dong, Z. H.; Wang, Z. G.; Zhang, F. X.; Jin, J., Layered  $\alpha$ -Co(OH)<sub>2</sub> Nanocones as Electrode Materials for Pseudocapacitors: Understanding the Effect of Interlayer Space on Electrochemical Activity. *Advanced Functional Materials* **2013**, 23 (21), 2758-2764.
  23. Jiang, H.; Ma, J.; Li, C., Mesoporous Carbon Incorporated Metal Oxide Nanomaterials as Supercapacitor Electrodes. *Advanced Materials* **2012**, 24 (30), 4197-4202.
  24. Acerce, M.; Voiry, D.; Chhowalla, M., Metallic 1T phase MoS<sub>2</sub> nanosheets as supercapacitor electrode materials. *Nature Nanotechnology* **2015**, 10 (4), 313-318.
  25. Bryan, A. M.; Santino, L. M.; Lu, Y.; Acharya, S.; D'Arcy, J. M., Conducting Polymers for Pseudocapacitive Energy Storage. *Chemistry of Materials* **2016**, 28 (17), 5989-5998.
  26. Liu, T.; Finn, L.; Yu, M.; Wang, H.; Zhai, T.; Lu, X.; Tong, Y.; Li, Y., Polyaniline and Polypyrrole Pseudocapacitor Electrodes with Excellent Cycling Stability. *Nano Letters* **2014**, 14 (5), 2522-2527.

27. Shi, Y.; Peng, L.; Ding, Y.; Zhao, Y.; Yu, G., Nanostructured conductive polymers for advanced energy storage. *Chemical Society Reviews* **2015**, *44* (19), 6684-6696.
28. Xie, J.; Rui, X.; Gu, P.; Wu, J.; Xu, Z. J.; Yan, Q.; Zhang, Q., Novel Conjugated Ladder-Structured Oligomer Anode with High Lithium Storage and Long Cycling Capability. *ACS Applied Materials & Interfaces* **2016**, *8* (26), 16932-16938.
29. Sun, T.; Li, Z.-j.; Wang, H.-g.; Bao, D.; Meng, F.-l.; Zhang, X.-b., A Biodegradable Polydopamine-Derived Electrode Material for High-Capacity and Long-Life Lithium-Ion and Sodium-Ion Batteries. *Angewandte Chemie International Edition* **2016**, *55* (36), 10662-10666.
30. Wang, X.; Zhang, C.; Xu, Y.; He, Q.; Mu, P.; Chen, Y.; Zeng, J.; Wang, F.; Jiang, J.-X., Conjugated Microporous Polytetra(2-Thienyl)ethylene as High Performance Anode Material for Lithium- and Sodium-Ion Batteries. *Macromolecular Chemistry and Physics* **2018**, *219* (7), 1700524.
31. Pan, L.; Yu, G.; Zhai, D.; Lee, H. R.; Zhao, W.; Liu, N.; Wang, H.; Tee, B. C.-K.; Shi, Y.; Cui, Y.; Bao, Z., Hierarchical nanostructured conducting polymer hydrogel with high electrochemical activity. *Proceedings of the National Academy of Sciences* **2012**, *109* (24), 9287-9292.
32. Kim, B. C.; Kwon, J. S.; Ko, J. M.; Park, J. H.; Too, C. O.; Wallace, G. G., Preparation and enhanced stability of flexible supercapacitor prepared from Nafion/polyaniline nanofiber. *Synthetic Metals* **2010**, *160* (1), 94-98.
33. Park, J.; Lee, C. W.; Joo, S. H.; Park, J. H.; Hwang, C.; Song, H.-K.; Park, Y. S.; Kwak, S. K.; Ahn, S.; Kang, S. J., Contorted polycyclic aromatic hydrocarbon: promising Li insertion organic anode. *Journal of Materials Chemistry A* **2018**, *6* (26), 12589-12597.
34. Hiszpanski, A. M.; Saathoff, J. D.; Shaw, L.; Wang, H.; Kraya, L.; Lüttich, F.; Brady, M. A.; Chabynec, M. L.; Kahn, A.; Clancy, P.; Loo, Y.-L., Halogenation of a Nonplanar Molecular Semiconductor to Tune Energy Levels and Bandgaps for Electron Transport. *Chemistry of Materials* **2015**, *27* (5), 1892-1900.
35. *Materials Studio 2018*.
36. Sun, H.; Jin, Z.; Yang, C.; Akkermans, R. L.; Robertson, S. H.; Spensley, N. A.; Miller, S.; Todd, S. M., COMPASS II: extended coverage for polymer and drug-like molecule databases. *J Mol Model* **2016**, *22* (2), 47.
37. Ewald, P. P., Die Berechnung optischer und elektrostatischer Gitterpotentiale. *Annalen der Physik* **1921**, *369* (3), 253-287.
38. Tosi, M. P., Cohesion of Ionic Solids in the Born Model\*\*Based on work performed under the auspices of the U.S. Atomic Energy Commission. In *Solid State Physics*, Seitz, F.; Turnbull, D.,

- Eds. Academic Press: 1964; Vol. 16, pp 1-120.
39. Mulliken, R. S., Electronic Population Analysis on LCAO–MO Molecular Wave Functions. I. *The Journal of Chemical Physics* **1955**, 23 (10), 1833-1840.
  40. Delley, B., An all-electron numerical method for solving the local density functional for polyatomic molecules. *The Journal of Chemical Physics* **1990**, 92 (1), 508-517.
  41. Delley, B., From molecules to solids with the DMol3 approach. *The Journal of Chemical Physics* **2000**, 113 (18), 7756-7764.
  42. Becke, A. D., Becke's three parameter hybrid method using the LYP correlation functional. *J. Chem. Phys* **1993**, 98 (492), 5648-5652.
  43. Stephens, P.; Devlin, F.; Chabalowski, C.; Frisch, M., Relaxation dynamics in the B (1/2) and C (3/2) charge transfer states of XeF in solid Ar. *J. Chem. Phys* **1994**, 98, 11623-11627.
  44. Grimme, S., Semiempirical GGA-type density functional constructed with a long-range dispersion correction. *Journal of Computational Chemistry* **2006**, 27 (15), 1787-1799.
  45. Perdew, J. P.; Burke, K.; Ernzerhof, M., Generalized Gradient Approximation Made Simple. *Physical Review Letters* **1996**, 77 (18), 3865-3868.
  46. Monkhorst, H. J.; Pack, J. D., Special points for Brillouin-zone integrations. *Physical Review B* **1976**, 13 (12), 5188-5192.
  47. Hiszpanski, A. M.; Woll, A. R.; Kim, B.; Nuckolls, C.; Loo, Y.-L., Altering the Polymorphic Accessibility of Polycyclic Aromatic Hydrocarbons with Fluorination. *Chemistry of Materials* **2017**, 29 (10), 4311-4316.

## Chapter 4. Polymorphism and Lithium Storage Mechanism of Redox-Active Covalent Triazine Framework Electrode Material

*This chapter includes the following contents:*

Buyukcakir, O.\*<sup>†</sup>; Ryu, J.<sup>†</sup>; Joo, S. H.<sup>†</sup>; Kang, J.; Yuksel, R.; Lee, J.; Jiang, Y.; Choi, S.; Lee, S. H.; Kwak, S. K.\*; Park, S.\*; Ruoff, R. S.\*, Lithium Accommodation in a Redox-Active Covalent Triazine Framework for High Areal Capacity and Fast-Charging Lithium-Ion Batteries. *Advanced Functional Materials* **2020**, *30* (36), 2003761. (<sup>†</sup>: **equally contributed**) Reproduced with permission from WILEY-VCH Verlag GmbH & Co. KGaA, Weinheim, copyright 2020.<sup>1</sup>

---

### 4.1 Introduction

Rechargeable lithium-ion batteries (LIBs) are used to power various consumer electronics and electric vehicles (EVs), and have grid-scale applications as efficient energy storage platforms.<sup>2, 3</sup> Although they have already shown significant advances,<sup>4, 5</sup> state-of-the-art LIBs have nearly reached their limit and are unable to meet certain needs for higher energy/power density, faster charging, and longer-cycle life, particularly for the commercialization of cost-effective portable electronics or high-performance EVs.<sup>6, 7</sup> Thus, designing and making new electrode materials that outperform conventional inorganic intercalation or alloying type materials is crucial for next-generation rechargeable batteries.<sup>8-10</sup>

Organic electrode materials with redox-active sites for charge storage have great potential to improve current LIBs by controlling the redox potentials through molecular design, and this has led to the exploration of various types of organic compounds.<sup>11-14</sup> The “active site” for the organic electrode materials can be an atom, molecule, or region that can have a redox-reaction. However, their typical high solubility in common electrolytes, both carbonate and ether-based, and their low electrical conductivity pose a major challenge for use in real battery systems.<sup>15-17</sup> On the other hand, porous organic polymers made by the covalent assembly of functional organic molecules are insoluble 2D or 3D extended structures.<sup>18-20</sup> Such porous polymers have served as functional materials in gas capture,<sup>21, 22</sup> catalysis,<sup>23</sup> molecular separation,<sup>24, 25</sup> and, recently, energy storage systems.<sup>26-31</sup> As a subclass of porous organic polymers, covalent organic frameworks (COFs) have recently emerged as electrode materials in various electrochemical systems.<sup>32-34</sup> Changing the molecular level of these polymeric frameworks by incorporating redox-active functional moieties, together with their regular porosity with

open-pore channels and extended  $\pi$ -conjugated backbones, make them promising electrode materials for LIBs.<sup>35-42</sup>

As an alternative to COFs, covalent triazine frameworks (CTFs) provide increased physicochemical stability because of the rigid triazine ( $C_3N_3$ ) linking units with strong C=C and C=N bonding and have been considered as promising materials for energy storage systems.<sup>43</sup> So far, few CTFs have been reported as electrode materials for rechargeable LIBs and these have shown the moderate specific capacity and rate capability.<sup>44-49</sup> In one of the initial studies, Sakaushi et al. reported an amorphous covalent triazine framework obtained from terephthalonitrile trimerization (amorphous CTF-1) showing a bipolar state that supplied a reversible capacity of about 160 mAh g<sup>-1</sup>.<sup>44</sup> Also, Lotsch et al. have reported a series of CTFs prepared from different linkers at different temperatures to deliver a specific capacity of up to 150 mAh g<sup>-1</sup>.<sup>47</sup> Other triazine containing porous polymers have also been tested as electrode materials in LIBs. Xin and co-workers have recently reported a porous polymer containing anthraquinone and triazine units in its backbone as an anode material, reported to have a specific capacity up to 1770 mAh g<sup>-1</sup> at 200 mA g<sup>-1</sup>.<sup>26</sup> Very recently, the fluorinated CTF and its exfoliated version have been investigated as an anode material in LIBs. While the pristine fluorinated CTF was reported to have a specific capacity of 538 mAh g<sup>-1</sup> at a current density of 100 mA g<sup>-1</sup>, its exfoliated products were stated to have higher lithium storage capacity up to 1035 mAh g<sup>-1</sup> at the same current density.<sup>49</sup> These reports support the promising picture of CTFs as electrode material for the LIBs. It is valuable to study other CTFs to more deeply understand the structure-property relations and also to improve the electrochemical performance of CTFs in terms of specific capacity and rate performance, to see if they can compete with their conventional inorganic analogs.

Most 2D COFs and CTFs adopt a totally eclipsed stacking motif due to the strong  $\pi$ - $\pi$  interaction between neighboring sheets which results in highly densely packed layers, making it difficult for lithium ions to reach the active sites located inside the pore channels. The inefficient utilization of these redox sites results in a low specific capacity and poor rate performance, particularly in fast-charging conditions. In order to increase Li-ion diffusion and boost the electrochemical performance of these polymeric frameworks, two common strategies have been used:<sup>50</sup> i) exfoliation of the sheets into few-layers either chemically or physically,<sup>37-39, 46</sup> ii) the growth of a limited number of polymer nanosheets on conductive surfaces including metal foils, graphene, and carbon nanotubes.<sup>36, 40, 45, 48, 51, 52</sup> The exfoliation of the polymeric frameworks into few-layer sheets results in shortened Li-ion diffusion paths, which enables access to more active sites.<sup>37, 38, 46</sup> However, the extremely low particle density of the active materials reduces the energy density of the batteries and the harsh exfoliation procedures lead to side reactions.<sup>46, 53</sup> In addition to the exfoliation strategy, a bottom-up approach such as exploiting the

limited growth of layer polymers on conductive surfaces not only produces a thin layer of COFs or CTFs which affords more accessible active sites for lithium ions but also provides better electrical conductivity and charge transfer efficiency for the materials compared to the pristine ones.<sup>36, 51</sup> Although this bottom-up strategy improves the specific capacity, the difficulty of controlling the thickness of such films, non-uniform film formation, contamination of the layers with precipitated polymeric particles, and, most importantly, low yields, limit its scalability and practical use.

In order to boost the electrochemical performance of CTFs, the integration of redox-active moieties with the CTF skeleton seems a promising approach, but the harsh reaction conditions typically used for their synthesis have, to date, limited this approach. Ionothermal polymerization, in which zinc chloride is used as both solvent and catalyst for the trimerization of aromatic nitriles at high-temperature (above the melting point of zinc chloride), is the most common approach for the preparation of CTFs.<sup>43, 54, 55</sup> But at this temperature, some carbonization is unavoidable and contaminates the product.<sup>56-58</sup> Compared to reported alternative synthesis methods,<sup>59-61</sup> Tan et al. have recently reported a new synthesis method using a condensation reaction of amidines and aldehydes under mild reaction conditions, which facilitates the incorporation of some redox-active functionalities.<sup>62, 63</sup> Due to these synthesis difficulties, the preparation of CTFs with redox-active units, which may enable the tunability and improvement of electrochemical performance, has not been fully explored.

Here we design a redox-active covalent triazine framework (rCTF) and suggest its use in lithium-ion batteries as an anode material. Redox-active anthraquinone units were incorporated into the framework through triazine linkages. The resultant polymeric framework had a large specific surface area, along with high porosity and physicochemical stability. When used as a redox-active anode material, a fully activated rCTF delivered about 1200 mAh g<sup>-1</sup>. To the best of our knowledge, this rCTF outperforms all COF-based anodes reported to date with such an areal capacity. According to our theoretical calculations of the lithium storage mechanism, the lithiation/delithiation process of the proposed rCTF structure involves up to a 23-electron redox process, which is consistent with the experimental observations. In addition to the highly active quinone units, the efficient binding to triazine and benzene rings in the electrochemical processes provides a large specific capacity for this rCTF. The possible progressive structural deformation with repeated lithiation and delithiation during activation may contribute to the larger number of accessible redox-active sites for lithium ions. In addition to the highly conjugated polymeric skeleton, large porosity and small particle size of the rCTF, the possibly increasing “disorder” contributes to fast charge and ion diffusion, providing outstanding rate performance. These findings demonstrate the potential of this rCTF for electrical energy storage and the importance of rational design to achieve the next-generation of high-performance batteries.

## 4.2 Computational Methods

### 4.2.1 Density Functional Tight Binding Calculation

To predict the most energetically stable packing mode and the crystal structure of rCTF, we performed density functional based tight binding (DFTB) calculations using the DFTB+ program.<sup>64</sup> The 3OB Slater-Koster atomic parameters were adopted for the study of rCTF since 3OB is appropriate for organic molecules consisting of carbon, hydrogen, nitrogen, and oxygen.<sup>65</sup> Spin polarization and the universal forcefield-based Lennard-Jones dispersion correction were taken into account in all calculations. The wave function was integrated using the Monkhorst-Pack  $k$ -point grids:  $1 \times 1 \times 8$   $k$ -point grid for the unit cell of rCTF consisting of one rCTF plane with the AA packing mode and  $1 \times 1 \times 4$   $k$ -point grid for the unit cell consisting of two rCTF planes with the other packing modes.<sup>66</sup> The convergence criterion for the self-consistent charge was set to  $1 \times 10^{-8}$ . The convergence criteria for geometry optimization were set to 0.01 kcal mol<sup>-1</sup> for the maximum energy change, 0.05 kcal mol<sup>-1</sup> Å<sup>-1</sup> for the maximum force, 0.02 GPa for the maximum stress, and  $5 \times 10^{-4}$  Å for the maximum displacement. Periodic boundary condition was applied in three dimensions.

### 4.2.2 Density Functional Theory Calculation

Density functional theory (DFT) calculations were performed using the Vienna Ab initio Simulation Package (VASP).<sup>67, 68</sup> The generalized gradient approximation with the Perdew-Burke-Ernzerhof (GGA-PBE) functional was used to describe the exchange-correlation potential of the electrons.<sup>69</sup> The interactions between ions and electrons were described by projector augmented wave (PAW) method.<sup>70</sup> A plane-wave basis set with a cutoff energy of 650 eV was employed to expand the wave functions. The van der Waals interactions were corrected using the Grimme's DFT-D3 method.<sup>71</sup> The convergence criterion for the self-consistent field calculation was set to  $10^{-6}$  eV atom<sup>-1</sup>. The convergence criterion for geometry optimization was set to 0.01 eV Å<sup>-1</sup> for force. The Brillouin zone was integrated using a  $1 \times 1 \times 2$   $k$ -point grid with the Monkhorst-Pack scheme for all calculations.<sup>66</sup> The voltage profile ( $V$ ) as a function of lithium content was calculated as follows:

$$V(n) = -\frac{E_{\text{Li}_{n_2}\text{-rCTF}} - E_{\text{Li}_{n_1}\text{-rCTF}} - (n_2 - n_1)E_{\text{Li}}}{q(n_2 - n_1)}$$

where  $E_{\text{Li}_{n_1}\text{-rCTF}}$  and  $E_{\text{Li}_{n_2}\text{-rCTF}}$  represent the total energy of the lithium-inserted rCTF structure,  $n_1$



and  $n_2$  are the numbers of lithium atoms inserted ( $n_2 > n_1$ ),  $E_{\text{Li}}$  is the total energy per atom of bcc bulk lithium, and  $q$  is the net charge of a lithium ion ( $q = +1e$ ).<sup>72</sup> The theoretical specific capacity ( $Q_{\text{theoretical}}$ ) of lithiated rCTF was calculated with Faraday's law:

$$Q_{\text{theoretical}} = \frac{nZF}{3600M_w} \times 1000$$

where  $n$  is the number of lithium atoms stored in rCTF,  $Z$  is the valence number ( $Z = 1$  for lithium),  $F$  is the Faraday constant ( $96485.3329 \text{ C mol}^{-1}$ ) and  $M_w$  is the weight of the rCTF ( $3087.02 \text{ g mol}^{-1}$ ). For calculating the maximum capacity of rCTF, we used the maximum number of lithium atoms stored in the rCTF until the calculated voltage decreases to zero.

### 4.2.3 Monte Carlo Simulation

Monte Carlo (MC) simulations were performed using the Sorption program.<sup>64</sup> Based on the Metropolis algorithm, the MC simulated annealing was carried out with the maximum number of  $1.0 \times 10^5$  loading steps, the maximum number of  $1.0 \times 10^7$  production steps, and 40 annealing cycles. The interatomic interactions were described by a COMPASS II force field with Bader charges obtained from DFT calculation at the end of each geometry optimization step.<sup>73,74</sup> The van der Waals interactions were calculated within the cutoff distance of  $18.5 \text{ \AA}$  and the long-range electrostatic interactions were treated by the Ewald summation method.<sup>75,76</sup>

### 4.2.4 Lithiation Simulation

To elucidate the lithium storage mechanism of the rCTF, the lithiation process was investigated following a stepwise lithium insertion procedure by performing DFT calculations together with MC simulations. This procedure consists of a lithium insertion step using an MC simulation and a geometry optimization step using DFT calculations. In the lithium insertion step, MC simulated annealing was performed to determine the stable adsorption sites of lithium in the crystal structure of rCTF. Here, six lithium atoms per step were inserted to account for the effect of the rCTF deformation during lithiation. In the geometry optimization step, the lattice parameters and atomic positions were relaxed. The stepwise lithium insertion procedure was repeated until a total of 138 lithium atoms, corresponding to  $\sim 1200 \text{ mAh g}^{-1}$ , had been inserted.

## 4.3 Results and Discussion

### 4.3.1 Packing Polymorphism of rCTF

The rCTF is a two-dimensionally extended structure (**Figure 4.1**), that is stacked in the out-of-plane direction to form a crystal structure. The experimental powder X-ray diffraction (PXRD) showed two relatively broad but intense distinct diffraction peaks at approximately  $6.3^\circ$  and  $26.1^\circ$  (**Figure 4.2**). This diffraction pattern indicates poor crystallinity of the rCTF. The peak at  $6.3^\circ$  can be interpreted as the in-plane reflection (110) and the peak located at  $26.1^\circ$  can be attributed to the stacking of layers with a spacing of about 3.4 Å. However, the broadness of the diffraction peaks makes it difficult to make conclusions on the structure at the atomistic level.

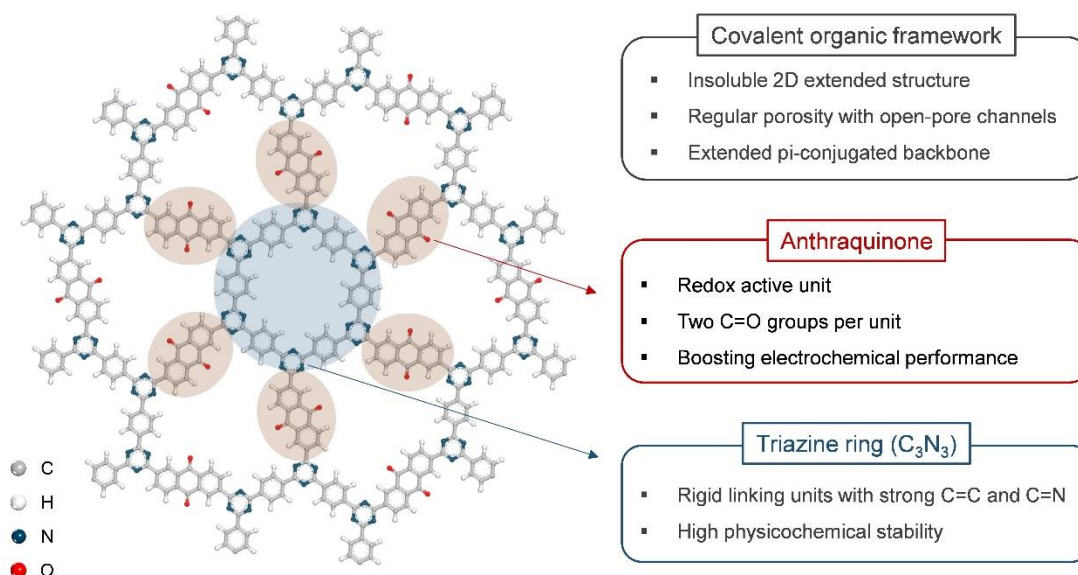


**Figure 4.1** Structure of the redox-active covalent triazine framework (rCTF). Reproduced from ref. 1 with permission from WILEY-VCH Verlag GmbH & Co. KGaA, Weinheim, copyright 2020.

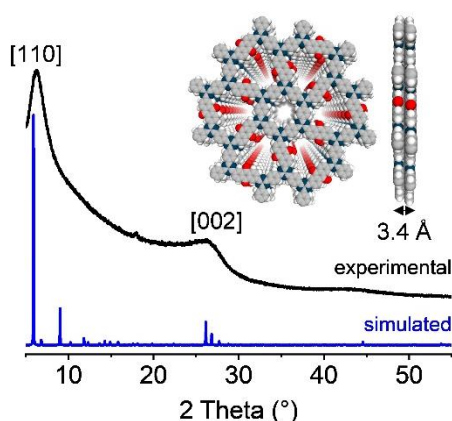


**Figure 4.2** The experimentally observed and theoretically calculated (simulated) XRD pattern of rCTF from the optimized structure with slipped-parallel stacking. Optimized rCTF structure with slipped-parallel stacking. Carbon, hydrogen, nitrogen, and oxygen are light gray, white, dark blue, and red, respectively. Reproduced from ref. 1 with permission from WILEY-VCH Verlag GmbH & Co. KGaA, Weinheim, copyright 2020.

Density-functional tight-binding (DFTB) calculation was carried out to obtain a repeating monolayer structure and determine its crystal structure. To predict the crystal structure of the two-dimensionally extended structure, the most stable packing mode should be explored first. To ascertain the packing mode of the rCTF, we constructed the potential energy surface through single-point energy calculations for structures with different *ab*-plane displacements between the top and bottom layers, starting from the AA packing mode. The two different  $17 \times 17$  grids of *ab*-plane displacements were used for sampling structures, each consisting of 289 different unit cells (**Figure 4.3**). The potential energy surface was then generated by interpolating the DFTB total energies over a  $1000 \times 1000$  fine grid using the bicubic spline method (**Figure 4.4**). The energy at the global minimum of the potential energy surface was set to be zero. The potential energy surface shows two local minima corresponding to AB and slipped-parallel packing modes, suggesting that rCTF can potentially exhibit packing polymorphism. Among possible packing modes, the slipped-parallel packing mode is the energetically favored stacking configuration, where the top layer is shifted by  $\approx 3/32$ th of a cell edge along the *b* direction relative to the bottom layer (**Figure 4.5**). The simulated PXRD pattern from this model is in good agreement with the observed experimental PXRD pattern (**Figure 4.2**). Thus, the PXRD and DFTB data show an extended 2D hexagonal lattice with slipped-parallel packing mode with calculated unit cell parameters of  $a = b = 29.9 \text{ \AA}$ ,  $c = 6.8 \text{ \AA}$ ,  $\alpha = \beta = 90.0^\circ$ , and  $\gamma = 120.0^\circ$ .

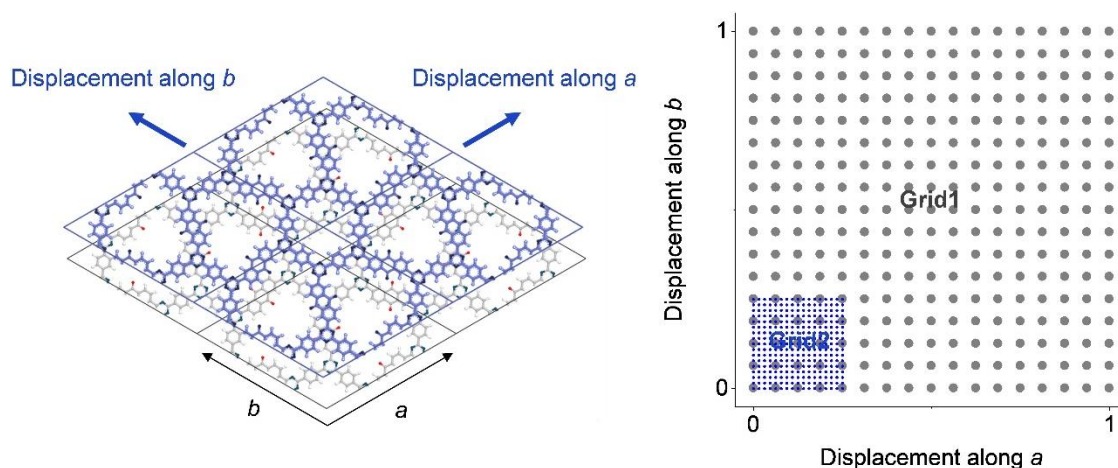


**Figure 4.3** Two grids were used to sample structures with different  $ab$ -plane displacements between top and bottom layers for generating potential energy surface. The grid is represented in fractional coordinates. The top layer is colored by blue. Reproduced from ref. 1 with permission from WILEY-VCH Verlag GmbH & Co. KGaA, Weinheim, copyright 2020.

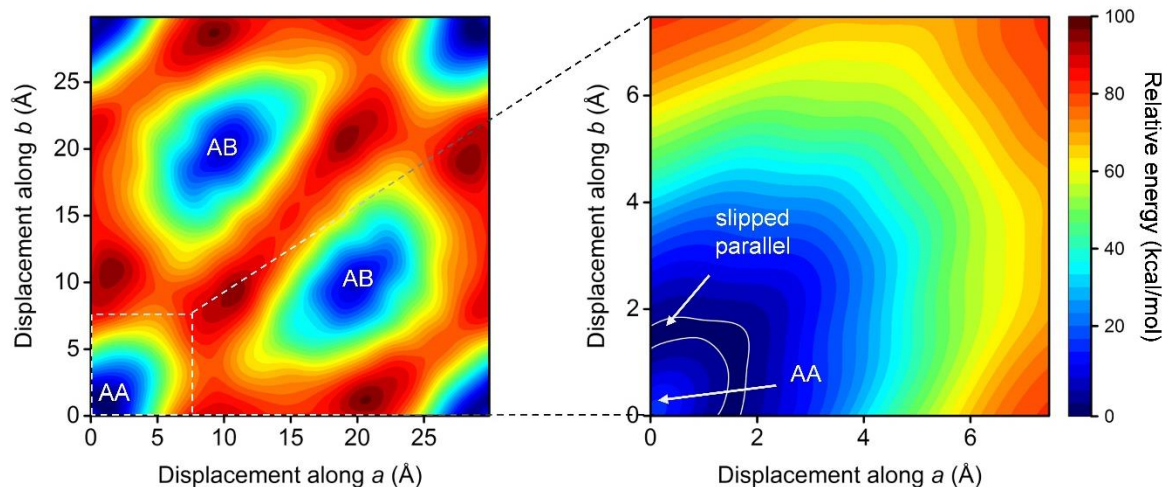


**Figure 4.4** The potential energy surface generated by interpolating the DFTB total energies. Reproduced from ref. 1 with permission from WILEY-VCH Verlag GmbH & Co. KGaA, Weinheim, copyright 2020.

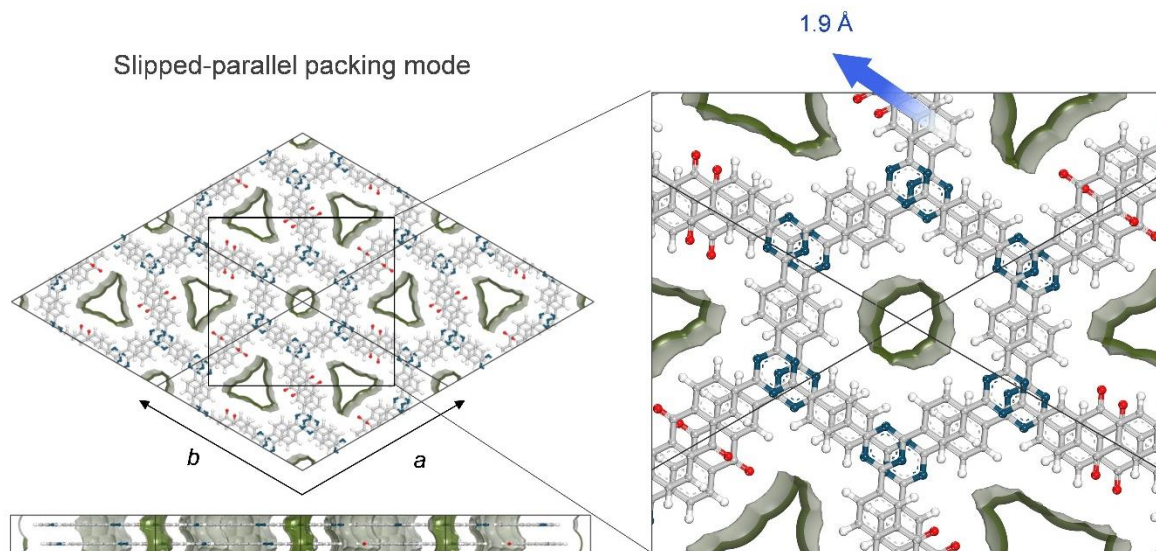


**Figure 4.5** Optimized rCTF structure with slipped-parallel stacking. Carbon, hydrogen, nitrogen, and oxygen are light gray, white, dark blue, and red, respectively. Reproduced from ref. 1 with permission from WILEY-VCH Verlag GmbH & Co. KGaA, Weinheim, copyright 2020.

### 4.3.2 Lithium Storage Mechanism of rCTF

In an attempt to understand the multi-electron redox reaction and the activation of the rCTF at the molecular level, we theoretically studied the lithium storage mechanism by focusing on the redox-active sites and the structural changes by performing density functional theory (DFT) calculations with Monte Carlo (MC) simulations. We predicted that lithiation of the rCTF can be divided into three distinct stages (**Figure 4.6** and **Figures 4.7–4.9** for the magnified views). In stage 1, lithium begins to be stored preferentially adjacent to the C=O of the quinone exposed at the surface of the pore channels (**Figure 4.7**). The redox reaction of the quinone was indicated by an increase in the C=O bond length, while the bond lengths of the other redox-active sites were unchanged (**Figure 4.10**). At this stage, the rCTF layers slip relative to the adjacent layers, providing more accessible sites for lithium. After reaching the theoretical specific capacity of quinone ( $104 \text{ mAh g}^{-1}$ , 1 Li per C=O), lithium started to participate in the redox reaction with the triazine ring in stage 2 (**Figure 4.8**). Lithium was mainly stored in the vicinity of the N atom of the triazine ring, while some of the lithium interacted with the benzene rings at the same time. The redox reactions gradually increased the C=N and C=C bond lengths but not the C=O bond length (**Figure 4.10**). The rCTF lost its original structure due to large deformation, but more redox-active sites were exposed. After the triazine ring had stored more than 1 lithium-ion ( $\approx 260 \text{ mAh g}^{-1}$ ) exceeding the specific capacity based on the quinone and triazine ring (1 Li per C=O and 1 Li per triazine ring), most of the redox-active sites (anthraquinone, triazine rings, and benzene rings) participated in the redox reaction with lithium in stage 3 (**Figure 4.9**). Notably, in stage 3, some of the benzene rings, or fused carbon rings, were transformed into an  $\text{sp}^3$ -like structure interacting with lithium. The reduction of the redox-active sites is indicated by the gradual increases in C=O, C=N, and C=C bond lengths (**Figure 4.10**).



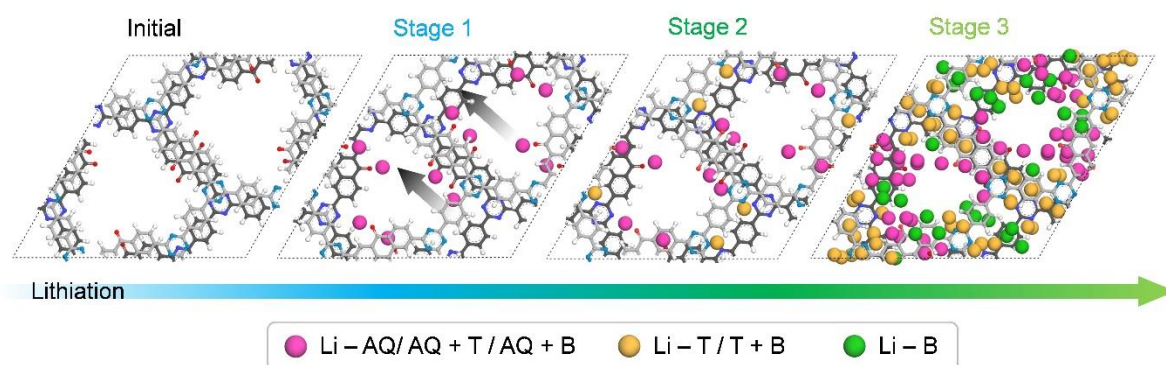


**Figure 4.6** The lithium storage mechanism of rCTF. Top view of the lithium-inserted rCTF structures during the three-stages of the lithiation of rCTF. Carbon, hydrogen, nitrogen, and oxygen are light gray, white, blue, and red, respectively. The atoms in the bottom layer are shown in darker colors for clarity. The magenta-colored sphere represents lithium interacting with at least more than one C=O group of anthraquinone (AQ) including the lithium interacting simultaneously with the AQ and triazine (T), or simultaneously with the AQ and benzene (B). The orange-colored sphere represents lithium interacting with T or interacting simultaneously with T and B. The lithium interacting with benzene only is represented by the green-colored sphere. Reproduced from ref. 1 with permission from WILEY-VCH Verlag GmbH & Co. KGaA, Weinheim, copyright 2020.



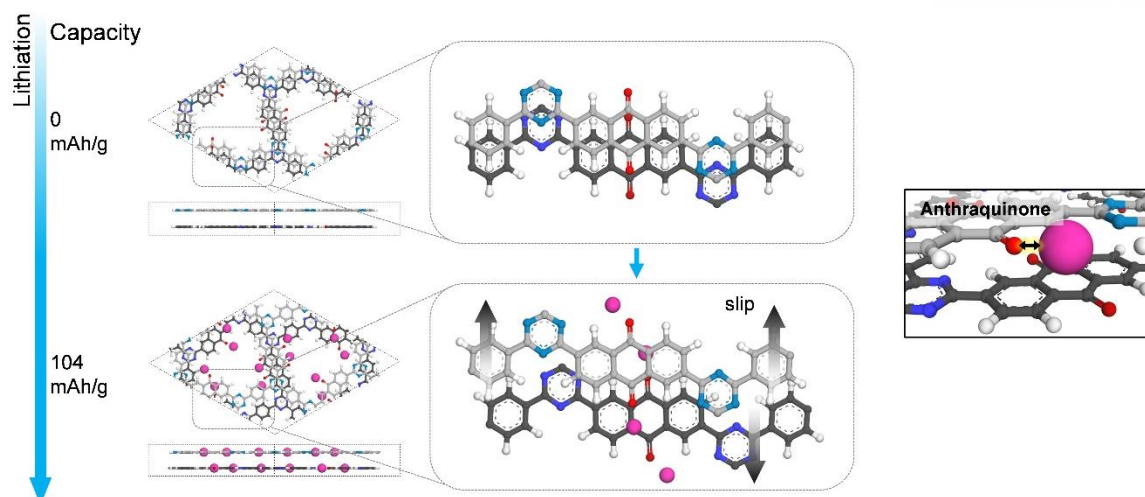


**Figure 4.7** Magnified views of the lithium-inserted rCTF structures at stage 1. The black arrows indicate rCTF layer translation. The magenta spheres represent lithium interacting with at least more than one C=O group of anthraquinone (AQ). Reproduced from ref. 1 with permission from WILEY-VCH Verlag GmbH & Co. KGaA, Weinheim, copyright 2020.

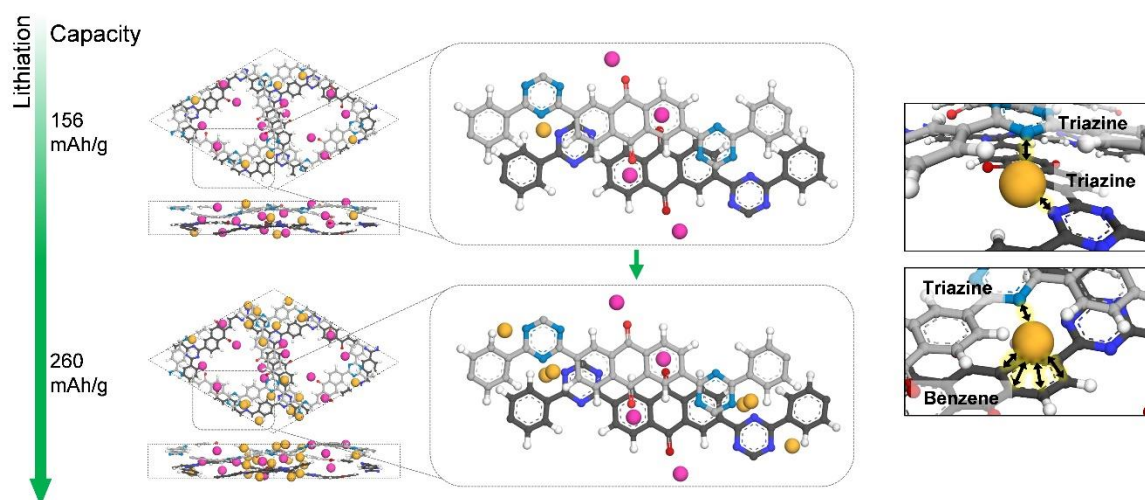


**Figure 4.8** Magnified views of the lithium-inserted rCTF structures at stage 2. The magenta spheres represent lithium interacting with at least more than one C=O group of anthraquinone (AQ) including the lithium interacting simultaneously with AQ and triazine (T). The orange spheres represent lithium interacting with T or interacting simultaneously with T and benzene (B). Reproduced from ref. 1 with permission from WILEY-VCH Verlag GmbH & Co. KGaA, Weinheim, copyright 2020.

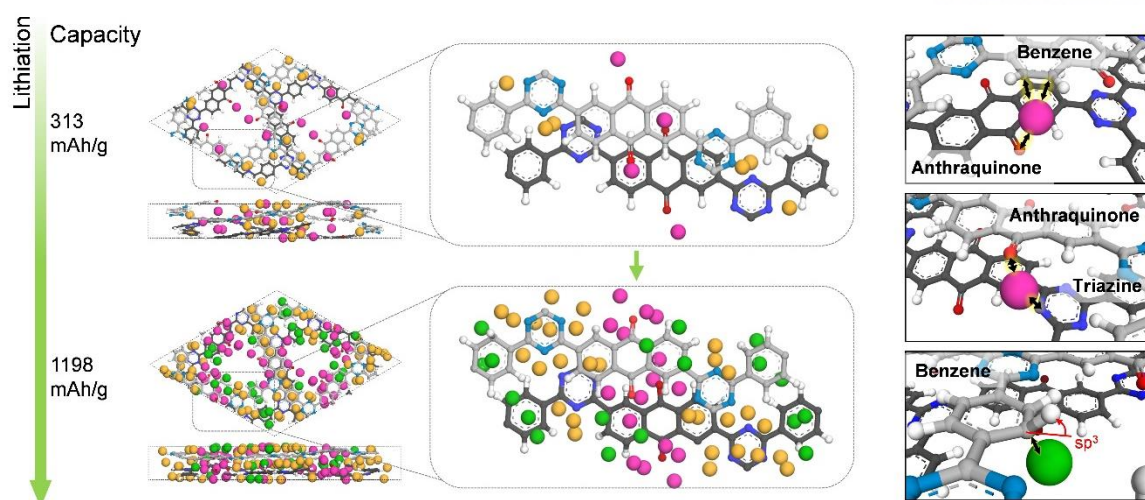


**Figure 4.9** Magnified views of the lithium-inserted rCTF structures at stage 3. The magenta spheres represent lithium interacting with at least more than one C=O group of anthraquinone (AQ) including the lithium interacting simultaneously with AQ and triazine (T), or simultaneously with AQ and benzene (B). The orange spheres represent lithium interacting with T or interacting simultaneously with T and B. The lithium interacting with only benzene is represented by green spheres. Reproduced from ref. 1 with permission from WILEY-VCH Verlag GmbH & Co. KGaA, Weinheim, copyright 2020.

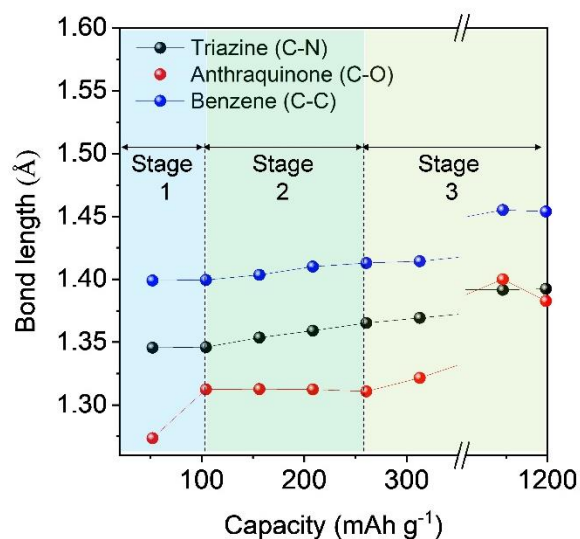


**Figure 4.10** Averaged bond length profile of the functional groups in rCTF. Reproduced from ref. 1 with permission from WILEY-VCH Verlag GmbH & Co. KGaA, Weinheim, copyright 2020.

Consequently, in the fully lithiated state, a total of 138 lithium atoms are stored in our model system consisting of six rCTF repeating units (23 lithium atoms per rCTF unit) (**Figure 4.11**). The number of lithium atoms in close contact with only one functional group is 32 lithium atoms. The rest of the lithium atoms are shared between two or more functional groups. The number of lithium atoms stored in each functional group was estimated by assuming that (for those that are bound to more than one functional group) they are shared equally to each functional group. For example, if a lithium atom simultaneously interacts with a benzene ring and a triazine ring, it is assumed that half of the lithium atom is stored in each functional group. As a result, in the fully lithiated state, per our model C=O groups store 3.9 lithium atoms (2.0 lithium atoms per C=O), triazine rings store 6.7 lithium atoms (3.4 lithium atoms per triazine ring), and benzene rings store  $\approx 12.4$  lithium atoms (3.1 lithium atoms per benzene ring) (**Figure 4.12**).

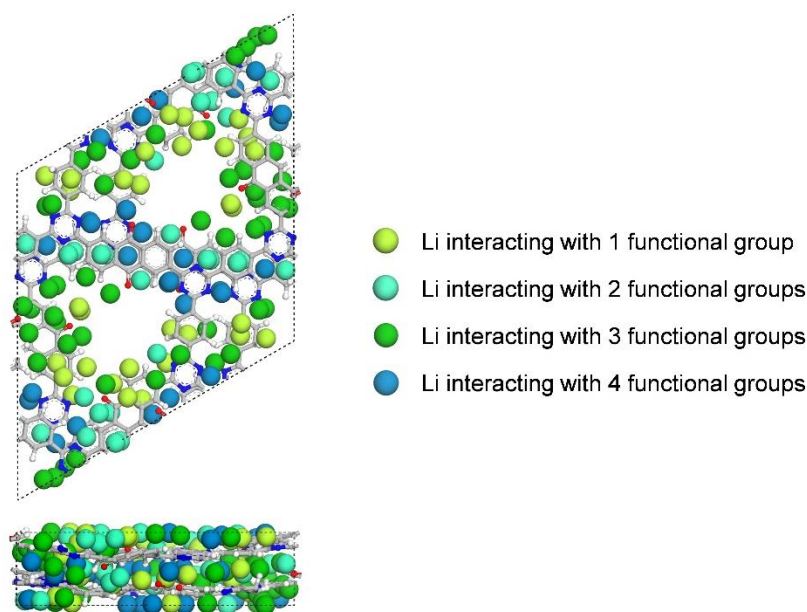


**Figure 4.11** Top and front views of the fully lithiated rCTF structures (specific capacity =  $1198 \text{ mAh g}^{-1}$ ). Carbon, hydrogen, nitrogen, and oxygen are light gray, white, blue, and red, respectively. Lithium is represented in different colors depending on the number of functional groups in close contact with the lithium. The criterion distance for close contact between two atoms was set to 89% of the sum of their van der Waals radii. Reproduced from ref. 1 with permission from WILEY-VCH Verlag GmbH & Co. KGaA, Weinheim, copyright 2020.

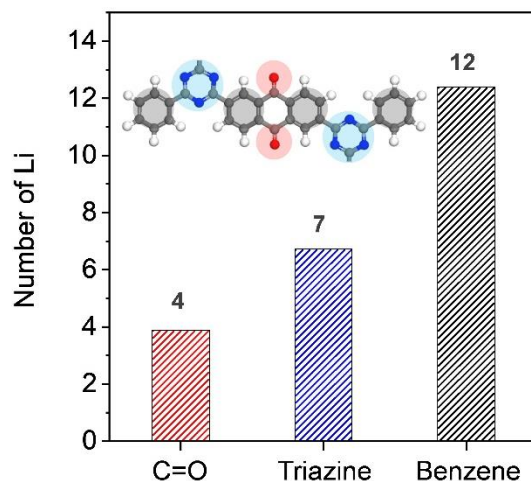


**Figure 4.12** The number of lithium atoms stored in each functional group per rCTF unit, per the model used here. Reproduced from ref. 1 with permission from WILEY-VCH Verlag GmbH & Co. KGaA, Weinheim, copyright 2020.

The calculated voltage profile shows that lithium ions are infiltrated into the rCTF to produce an energy density of up to 1198 mAh g<sup>-1</sup> in the electrochemical potential range above the lithium plating/stripping potential, which is consistent with the experimental (saturated) capacity of  $\approx 1200$  mAh g<sup>-1</sup> at a current density of 0.5C (**Figure 4.13**). This calculated result also agrees well with the experimental CV analysis with respect to the multiple redox reactions. The multiple reductions at above the 0.5 V can be ascribed to the redox reaction of the quinone and triazine groups in stages 1 and 2, respectively, from matching our calculations with the experimental CV analysis. The sloping region below 0.5 V corresponds to stage 3, where the benzene groups become activated, contributing to a large fraction of the capacity together with the quinone and triazine rings. During the overall lithiation steps, we note from the calculation that the gradual deformation of the pore network structure causes more redox-active sites to be accessible for lithium atoms, for example fused carbon rings, which were originally “concealed” because of the original stacked structure (**Figure 4.14**). This deformed structure, which remains stable even after delithiation (**Figure 4.15**), is expected to retain the activated accessible sites contributing to the increased specific capacity. To investigate the volume change of rCTF, we also calculated the volume of the rCTF before and after lithiation, based on the model systems obtained from the simulation of lithiation. The volume change was calculated to be negligibly small ( $\Delta V/V_0 \times 100 = -0.2\%$ ). This may be attributed to the porous structure of the rCTF with large free volume; lithium atoms are mainly stored at the surface of the pore channels and also the deformation of the rCTF structure induced by lithiation occurs toward the large pore. This makes the change of the total volume negligible.



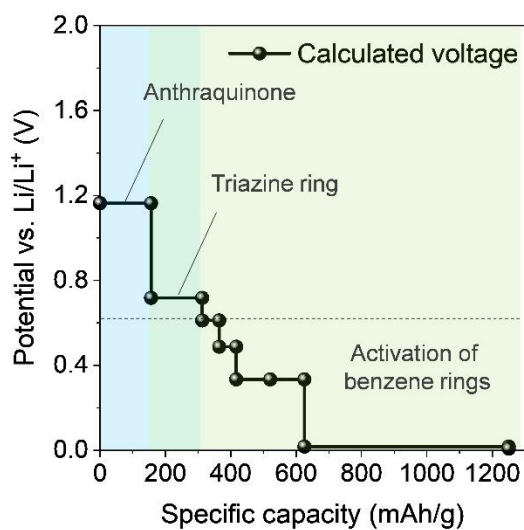


**Figure 4.13** Calculated voltage profile of the rCTF lithiation process. Reproduced from ref. 1 with permission from WILEY-VCH Verlag GmbH & Co. KGaA, Weinheim, copyright 2020.

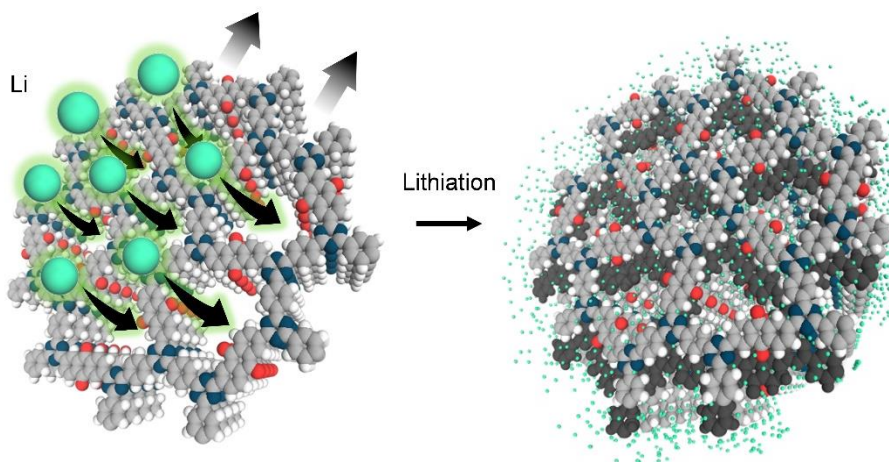


**Figure 4.14** Schematic of the rCTF lithiation process. The gray arrows indicate the rCTF layer translation. Carbon, hydrogen, nitrogen, and oxygen are light gray, white, blue, and red, respectively. Reproduced from ref. 1 with permission from WILEY-VCH Verlag GmbH & Co. KGaA, Weinheim, copyright 2020.

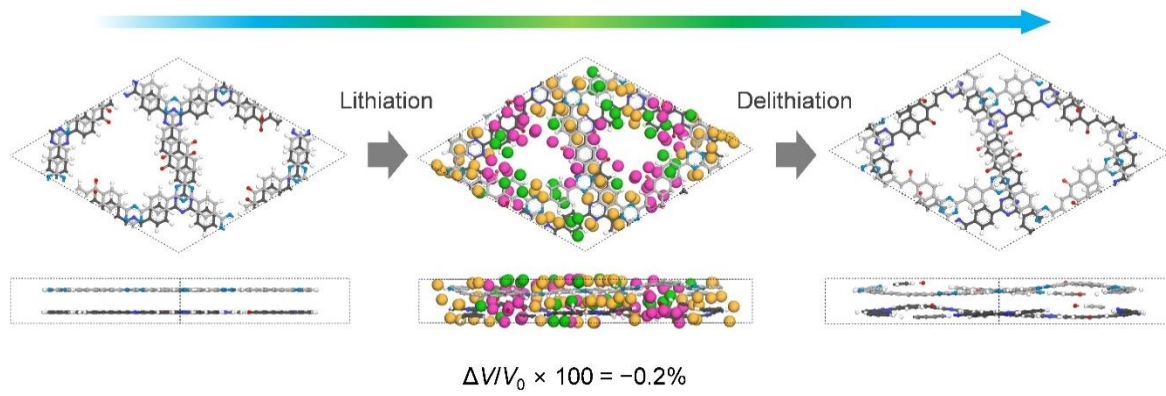


**Figure 4.15** Relaxed structure of rCTF after lithiation and delithiation. Reproduced from ref. 1 with permission from WILEY-VCH Verlag GmbH & Co. KGaA, Weinheim, copyright 2020.

### 4.3.3 Electronic Structure of rCTF

To understand the intrinsic electronic structure of rCTF and the effect of extrinsic perturbation due to charge transport during lithiation, we performed density functional theory calculations and analyzed the projected density of states (PDOS) according to the state-of-charge (**Figure 4.16**). From the PDOS plots, we examined the electronic states near the Fermi level, especially the unoccupied states; The “unoccupied states” are filled with electrons transferred from lithium when the rCTF is reduced during lithiation. In the pristine rCTF, the unoccupied states near the conduction band minimum (CBM) are mainly contributed by the anthraquinone (**Figure 4.16a**). At the energy level above those states, one finds the unoccupied states of the triazine ring and the benzene ring. Thus, per this analysis, during lithiation the anthraquinone is reduced first, followed by the triazine ring and then the benzene ring. Indeed, in stage 1 of the lithiation process, electrons are filled in the unoccupied states of anthraquinone (**Figure 4.16b**). In stage 2, electrons are primarily filled in the unoccupied states of the triazine ring (**Figure 4.16c**). In stage 3, electrons are filled in the unoccupied states of anthraquinone, triazine ring and benzene ring; the energy levels of those states are not clearly separated (**Figure 4.16d**). Our DFT results indicate that the electronic structure of rCTF is consistent with the experimentally observed mechanism of lithium storage. We note that the lithiation results in a transition from semiconductor to metal: The pristine rCTF is a semiconductor with a band gap of 1.44 eV. As lithiation progresses, the Fermi level is shifted upward and crosses the conduction bands, indicative of metallic character. This transition is expected to improve electronic conductivity and thus minimize the resistance.



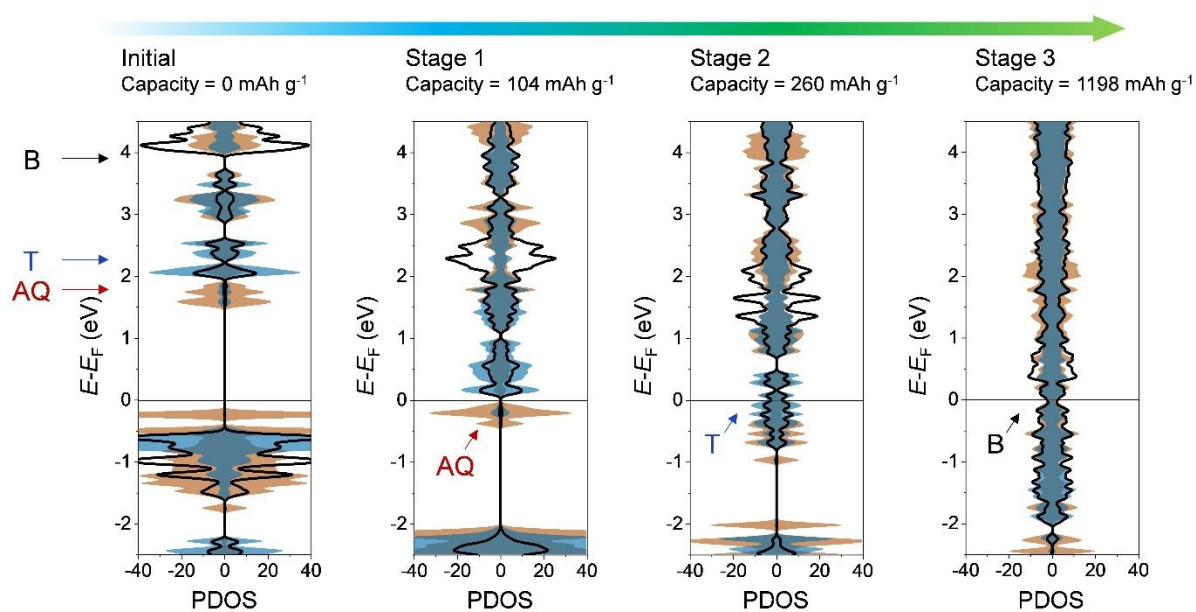


**Figure 4.16** PDOS plots of lithiated rCTF in initial state, the end of stage 1, the end of stage 2 and the end of stage 3. Benzene in the plots refers to the 6 carbon ring located between the two triazine rings in rCTF. Reproduced from ref. 1 with permission from WILEY-VCH Verlag GmbH & Co. KGaA, Weinheim, copyright 2020.

## 4.4 Conclusion

We have demonstrated the new rCTF as a promising anode material for Li-ion batteries. The strong triazine linkages of rCTF provide not only a stable polymeric framework with significant electrochemical stability but also contribute to the conductivity and charge transport by the formation of a conjugated framework. According to theoretical calculations, the progressive structural deformation of rCTF during activation provides more accessible redox-active sites. The utilization of quinone, triazine, and especially benzene rings as redox-active sites provides a large specific capacity of up to  $\approx 1200 \text{ mAh g}^{-1}$ . The open channels and small particles and possible molecular deformation and decreased crystallinity that allows access to additional binding sites during/after activation, significantly improves the lithium-ion diffusion and electrolyte infiltration, which provides a remarkable rate capability without sacrificing the specific capacity. These findings demonstrate the potential of using polymeric frameworks as high-performance electrode materials for lithium-ion batteries and also pave the way for perhaps achieving a fundamental understanding of the mechanism and provide a possibility for the rational “chemical design” of energy storage systems.

## 4.5 References

1. Buyukcakir, O.; Ryu, J.; Joo, S. H.; Kang, J.; Yuksel, R.; Lee, J.; Jiang, Y.; Choi, S.; Lee, S. H.; Kwak, S. K.; Park, S.; Ruoff, R. S., Lithium Accommodation in a Redox-Active Covalent Triazine Framework for High Areal Capacity and Fast-Charging Lithium-Ion Batteries. *Advanced Functional Materials* **2020**, *30* (36), 2003761.
2. Zeng, X.; Li, M.; Abd El-Hady, D.; Alshitari, W.; Al-Bogami, A. S.; Lu, J.; Amine, K., Commercialization of Lithium Battery Technologies for Electric Vehicles. *Advanced Energy Materials* **2019**, *9* (27), 1900161.
3. Martin, C., Driving change in the battery industry. *Nature Nanotechnology* **2014**, *9* (5), 327-328.
4. Goodenough, J. B.; Park, K.-S., The Li-Ion Rechargeable Battery: A Perspective. *Journal of the American Chemical Society* **2013**, *135* (4), 1167-1176.
5. Li, M.; Lu, J.; Chen, Z.; Amine, K., 30 Years of Lithium-Ion Batteries. *Advanced Materials* **2018**, *30* (33), 1800561.
6. Armand, M.; Tarascon, J. M., Building better batteries. *Nature* **2008**, *451* (7179), 652-657.
7. Liu, Y.; Zhu, Y.; Cui, Y., Challenges and opportunities towards fast-charging battery materials. *Nature Energy* **2019**, *4* (7), 540-550.
8. Ryu, J.; Chen, T.; Bok, T.; Song, G.; Ma, J.; Hwang, C.; Luo, L.; Song, H.-K.; Cho, J.; Wang, C.; Zhang, S.; Park, S., Mechanical mismatch-driven rippling in carbon-coated silicon sheets for stress-resilient battery anodes. *Nature Communications* **2018**, *9* (1), 2924.
9. Wang, B.; Ryu, J.; Choi, S.; Zhang, X.; Pribat, D.; Li, X.; Zhi, L.; Park, S.; Ruoff, R. S., Ultrafast-Charging Silicon-Based Coral-Like Network Anodes for Lithium-Ion Batteries with High Energy and Power Densities. *ACS Nano* **2019**, *13* (2), 2307-2315.
10. Ryu, J.; Song, W.-J.; Lee, S.; Choi, S.; Park, S., A Game Changer: Functional Nano/Micromaterials for Smart Rechargeable Batteries. *Advanced Functional Materials* **2020**, *30* (2), 1902499.
11. Lee, S.; Kwon, G.; Ku, K.; Yoon, K.; Jung, S.-K.; Lim, H.-D.; Kang, K., Recent Progress in Organic Electrodes for Li and Na Rechargeable Batteries. *Advanced Materials* **2018**, *30* (42), 1704682.
12. Liang, Y.; Tao, Z.; Chen, J., Organic Electrode Materials for Rechargeable Lithium Batteries. *Advanced Energy Materials* **2012**, *2* (7), 742-769.
13. Luo, C.; Borodin, O.; Ji, X.; Hou, S.; Gaskell, K. J.; Fan, X.; Chen, J.; Deng, T.; Wang, R.; Jiang, J.; Wang, C., Azo compounds as a family of organic electrode materials for alkali-ion batteries. *Proceedings of the National Academy of Sciences* **2018**, *115* (9), 2004.

14. Peng, C.; Ning, G.-H.; Su, J.; Zhong, G.; Tang, W.; Tian, B.; Su, C.; Yu, D.; Zu, L.; Yang, J.; Ng, M.-F.; Hu, Y.-S.; Yang, Y.; Armand, M.; Loh, K. P., Reversible multi-electron redox chemistry of  $\pi$ -conjugated N-containing heteroaromatic molecule-based organic cathodes. *Nature Energy* **2017**, *2* (7), 17074.
15. Bhosale, M. E.; Chae, S.; Kim, J. M.; Choi, J.-Y., Organic small molecules and polymers as an electrode material for rechargeable lithium ion batteries. *Journal of Materials Chemistry A* **2018**, *6* (41), 19885-19911.
16. Kim, J.; Kim, J. H.; Ariga, K., Redox-Active Polymers for Energy Storage Nanoarchitectonics. *Joule* **2017**, *1* (4), 739-768.
17. Muench, S.; Wild, A.; Friebe, C.; Häupler, B.; Janoschka, T.; Schubert, U. S., Polymer-Based Organic Batteries. *Chemical Reviews* **2016**, *116* (16), 9438-9484.
18. Das, S.; Heasman, P.; Ben, T.; Qiu, S., Porous Organic Materials: Strategic Design and Structure–Function Correlation. *Chemical Reviews* **2017**, *117* (3), 1515-1563.
19. Wu, D.; Xu, F.; Sun, B.; Fu, R.; He, H.; Matyjaszewski, K., Design and Preparation of Porous Polymers. *Chemical Reviews* **2012**, *112* (7), 3959-4015.
20. Chaoui, N.; Trunk, M.; Dawson, R.; Schmidt, J.; Thomas, A., Trends and challenges for microporous polymers. *Chemical Society Reviews* **2017**, *46* (11), 3302-3321.
21. Slater, A. G.; Cooper, A. I., Function-led design of new porous materials. *Science* **2015**, *348* (6238), aaa8075.
22. Buyukcakir, O.; Je, S. H.; Park, J.; Patel, H. A.; Jung, Y.; Yavuz, C. T.; Coskun, A., Systematic Investigation of the Effect of Polymerization Routes on the Gas-Sorption Properties of Nanoporous Azobenzene Polymers. *Chemistry – A European Journal* **2015**, *21* (43), 15320-15327.
23. Kaur, P.; Hupp, J. T.; Nguyen, S. T., Porous Organic Polymers in Catalysis: Opportunities and Challenges. *ACS Catalysis* **2011**, *1* (7), 819-835.
24. Alsbaiee, A.; Smith, B. J.; Xiao, L.; Ling, Y.; Helbling, D. E.; Dichtel, W. R., Rapid removal of organic micropollutants from water by a porous  $\beta$ -cyclodextrin polymer. *Nature* **2016**, *529* (7585), 190-194.
25. Dey, K.; Pal, M.; Rout, K. C.; Kunjattu H, S.; Das, A.; Mukherjee, R.; Kharul, U. K.; Banerjee, R., Selective Molecular Separation by Interfacially Crystallized Covalent Organic Framework Thin Films. *Journal of the American Chemical Society* **2017**, *139* (37), 13083-13091.
26. Kang, H.; Liu, H.; Li, C.; Sun, L.; Zhang, C.; Gao, H.; Yin, J.; Yang, B.; You, Y.; Jiang, K.-C.; Long, H.; Xin, S., Polyanthraquinone-Triazine—A Promising Anode Material for High-Energy Lithium-Ion Batteries. *ACS Applied Materials & Interfaces* **2018**, *10* (43), 37023-

- 37030.
27. Wang, J.; Chen, C. S.; Zhang, Y., Hexaazatrinaphthylene-Based Porous Organic Polymers as Organic Cathode Materials for Lithium-Ion Batteries. *ACS Sustainable Chemistry & Engineering* **2018**, *6* (2), 1772-1779.
  28. Xu, F.; Chen, X.; Tang, Z.; Wu, D.; Fu, R.; Jiang, D., Redox-active conjugated microporous polymers: a new organic platform for highly efficient energy storage. *Chemical Communications* **2014**, *50* (37), 4788-4790.
  29. Wei, W.; Chang, G.; Xu, Y.; Yang, L., An indole-based conjugated microporous polymer: a new and stable lithium storage anode with high capacity and long life induced by cation- $\pi$  interactions and a N-rich aromatic structure. *Journal of Materials Chemistry A* **2018**, *6* (39), 18794-18798.
  30. Zhang, C.; He, Y.; Mu, P.; Wang, X.; He, Q.; Chen, Y.; Zeng, J.; Wang, F.; Xu, Y.; Jiang, J.-X., Toward High Performance Thiophene-Containing Conjugated Microporous Polymer Anodes for Lithium-Ion Batteries through Structure Design. *Advanced Functional Materials* **2018**, *28* (4), 1705432.
  31. Zhang, S.; Huang, W.; Hu, P.; Huang, C.; Shang, C.; Zhang, C.; Yang, R.; Cui, G., Conjugated microporous polymers with excellent electrochemical performance for lithium and sodium storage. *Journal of Materials Chemistry A* **2015**, *3* (5), 1896-1901.
  32. Gu, S.; Wu, S.; Cao, L.; Li, M.; Qin, N.; Zhu, J.; Wang, Z.; Li, Y.; Li, Z.; Chen, J.; Lu, Z., Tunable Redox Chemistry and Stability of Radical Intermediates in 2D Covalent Organic Frameworks for High Performance Sodium Ion Batteries. *Journal of the American Chemical Society* **2019**, *141* (24), 9623-9628.
  33. Song, Y.; Sun, Q.; Aguila, B.; Ma, S., Opportunities of Covalent Organic Frameworks for Advanced Applications. *Advanced Science* **2019**, *6* (2), 1801410.
  34. Halder, A.; Ghosh, M.; Khayum M, A.; Bera, S.; Addicoat, M.; Sasmal, H. S.; Karak, S.; Kurungot, S.; Banerjee, R., Interlayer Hydrogen-Bonded Covalent Organic Frameworks as High-Performance Supercapacitors. *Journal of the American Chemical Society* **2018**, *140* (35), 10941-10945.
  35. Xu, S.; Wang, G.; Biswal, B. P.; Addicoat, M.; Paasch, S.; Sheng, W.; Zhuang, X.; Brunner, E.; Heine, T.; Berger, R.; Feng, X., A Nitrogen-Rich 2D  $sp^2$ -Carbon-Linked Conjugated Polymer Framework as a High-Performance Cathode for Lithium-Ion Batteries. *Angewandte Chemie International Edition* **2019**, *58* (3), 849-853.
  36. Lei, Z.; Yang, Q.; Xu, Y.; Guo, S.; Sun, W.; Liu, H.; Lv, L.-P.; Zhang, Y.; Wang, Y., Boosting lithium storage in covalent organic framework via activation of 14-electron redox

- chemistry. *Nature Communications* **2018**, *9* (1), 576.
37. Lei, Z.; Chen, X.; Sun, W.; Zhang, Y.; Wang, Y., Exfoliated Triazine-Based Covalent Organic Nanosheets with Multielectron Redox for High-Performance Lithium Organic Batteries. *Advanced Energy Materials* **2019**, *9* (3), 1801010.
  38. Wang, S.; Wang, Q.; Shao, P.; Han, Y.; Gao, X.; Ma, L.; Yuan, S.; Ma, X.; Zhou, J.; Feng, X.; Wang, B., Exfoliation of Covalent Organic Frameworks into Few-Layer Redox-Active Nanosheets as Cathode Materials for Lithium-Ion Batteries. *Journal of the American Chemical Society* **2017**, *139* (12), 4258-4261.
  39. Wang, Z.; Li, Y.; Liu, P.; Qi, Q.; Zhang, F.; Lu, G.; Zhao, X.; Huang, X., Few layer covalent organic frameworks with graphene sheets as cathode materials for lithium-ion batteries. *Nanoscale* **2019**, *11* (12), 5330-5335.
  40. Yang, H.; Zhang, S.; Han, L.; Zhang, Z.; Xue, Z.; Gao, J.; Li, Y.; Huang, C.; Yi, Y.; Liu, H.; Li, Y., High Conductive Two-Dimensional Covalent Organic Framework for Lithium Storage with Large Capacity. *ACS Applied Materials & Interfaces* **2016**, *8* (8), 5366-5375.
  41. Bai, L.; Gao, Q.; Zhao, Y., Two fully conjugated covalent organic frameworks as anode materials for lithium ion batteries. *Journal of Materials Chemistry A* **2016**, *4* (37), 14106-14110.
  42. Haldar, S.; Roy, K.; Nandi, S.; Chakraborty, D.; Puthusseri, D.; Gawli, Y.; Ogale, S.; Vaidhyanathan, R., High and Reversible Lithium Ion Storage in Self-Exfoliated Triazole-Triformyl Phloroglucinol-Based Covalent Organic Nanosheets. *Advanced Energy Materials* **2018**, *8* (8), 1702170.
  43. Liu, M.; Guo, L.; Jin, S.; Tan, B., Covalent triazine frameworks: synthesis and applications. *Journal of Materials Chemistry A* **2019**, *7* (10), 5153-5172.
  44. Sakaushi, K.; Nickerl, G.; Wisser, F. M.; Nishio-Hamane, D.; Hosono, E.; Zhou, H.; Kaskel, S.; Eckert, J., An Energy Storage Principle using Bipolar Porous Polymeric Frameworks. *Angewandte Chemie International Edition* **2012**, *51* (31), 7850-7854.
  45. Su, Y.; Liu, Y.; Liu, P.; Wu, D.; Zhuang, X.; Zhang, F.; Feng, X., Compact Coupled Graphene and Porous Polyaryltriazine-Derived Frameworks as High Performance Cathodes for Lithium-Ion Batteries. *Angewandte Chemie International Edition* **2015**, *54* (6), 1812-1816.
  46. Zhu, Y.; Chen, X.; Cao, Y.; Peng, W.; Li, Y.; Zhang, G.; Zhang, F.; Fan, X., Reversible intercalation and exfoliation of layered covalent triazine frameworks for enhanced lithium ion storage. *Chemical Communications* **2019**, *55* (10), 1434-1437.
  47. See, K. A.; Hug, S.; Schwinghammer, K.; Lumley, M. A.; Zheng, Y.; Nolt, J. M.; Stucky, G. D.; Wudl, F.; Lotsch, B. V.; Seshadri, R., Lithium Charge Storage Mechanisms of

- Cross-Linked Triazine Networks and Their Porous Carbon Derivatives. *Chemistry of Materials* **2015**, 27 (11), 3821-3829.
48. Zhu, J.; Zhuang, X.; Yang, J.; Feng, X.; Hirano, S.-i., Graphene-coupled nitrogen-enriched porous carbon nanosheets for energy storage. *Journal of Materials Chemistry A* **2017**, 5 (32), 16732-16739.
  49. Zhang, H.; Sun, W.; Chen, X.; Wang, Y., Few-Layered Fluorinated Triazine-Based Covalent Organic Nanosheets for High-Performance Alkali Organic Batteries. *ACS Nano* **2019**, 13 (12), 14252-14261.
  50. Wang, H.; Zeng, Z.; Xu, P.; Li, L.; Zeng, G.; Xiao, R.; Tang, Z.; Huang, D.; Tang, L.; Lai, C.; Jiang, D.; Liu, Y.; Yi, H.; Qin, L.; Ye, S.; Ren, X.; Tang, W., Recent progress in covalent organic framework thin films: fabrications, applications and perspectives. *Chemical Society Reviews* **2019**, 48 (2), 488-516.
  51. Xu, F.; Jin, S.; Zhong, H.; Wu, D.; Yang, X.; Chen, X.; Wei, H.; Fu, R.; Jiang, D., Electrochemically active, crystalline, mesoporous covalent organic frameworks on carbon nanotubes for synergistic lithium-ion battery energy storage. *Scientific Reports* **2015**, 5 (1), 8225.
  52. Luo, Z.; Liu, L.; Ning, J.; Lei, K.; Lu, Y.; Li, F.; Chen, J., A Microporous Covalent–Organic Framework with Abundant Accessible Carbonyl Groups for Lithium-Ion Batteries. *Angewandte Chemie International Edition* **2018**, 57 (30), 9443-9446.
  53. Bunck, D. N.; Dichtel, W. R., Bulk Synthesis of Exfoliated Two-Dimensional Polymers Using Hydrazone-Linked Covalent Organic Frameworks. *Journal of the American Chemical Society* **2013**, 135 (40), 14952-14955.
  54. Kuhn, P.; Antonietti, M.; Thomas, A., Porous, Covalent Triazine-Based Frameworks Prepared by Ionothermal Synthesis. *Angewandte Chemie International Edition* **2008**, 47 (18), 3450-3453.
  55. Bojdys, M. J.; Jeromenok, J.; Thomas, A.; Antonietti, M., Rational Extension of the Family of Layered, Covalent, Triazine-Based Frameworks with Regular Porosity. *Advanced Materials* **2010**, 22 (19), 2202-2205.
  56. Hug, S.; Tauchert, M. E.; Li, S.; Pachmayr, U. E.; Lotsch, B. V., A functional triazine framework based on N-heterocyclic building blocks. *Journal of Materials Chemistry* **2012**, 22 (28), 13956-13964.
  57. Kuecken, S.; Schmidt, J.; Zhi, L.; Thomas, A., Conversion of amorphous polymer networks to covalent organic frameworks under ionothermal conditions: a facile synthesis route for covalent triazine frameworks. *Journal of Materials Chemistry A* **2015**, 3 (48), 24422-24427.
  58. Kuhn, P.; Forget, A.; Su, D.; Thomas, A.; Antonietti, M., From Microporous Regular Frameworks to Mesoporous Materials with Ultrahigh Surface Area: Dynamic Reorganization of



- Porous Polymer Networks. *Journal of the American Chemical Society* **2008**, *130* (40), 13333-13337.
59. Ren, S.; Bojdys, M. J.; Dawson, R.; Laybourn, A.; Khimyak, Y. Z.; Adams, D. J.; Cooper, A. I., Porous, Fluorescent, Covalent Triazine-Based Frameworks Via Room-Temperature and Microwave-Assisted Synthesis. *Advanced Materials* **2012**, *24* (17), 2357-2361.
  60. Talapaneni, S. N.; Hwang, T. H.; Je, S. H.; Buyukcakir, O.; Choi, J. W.; Coskun, A., Elemental-Sulfur-Mediated Facile Synthesis of a Covalent Triazine Framework for High-Performance Lithium–Sulfur Batteries. *Angewandte Chemie International Edition* **2016**, *55* (9), 3106-3111.
  61. Yu, S.-Y.; Mahmood, J.; Noh, H.-J.; Seo, J.-M.; Jung, S.-M.; Shin, S.-H.; Im, Y.-K.; Jeon, I.-Y.; Baek, J.-B., Direct Synthesis of a Covalent Triazine-Based Framework from Aromatic Amides. *Angewandte Chemie International Edition* **2018**, *57* (28), 8438-8442.
  62. Wang, K.; Yang, L.-M.; Wang, X.; Guo, L.; Cheng, G.; Zhang, C.; Jin, S.; Tan, B.; Cooper, A., Covalent Triazine Frameworks via a Low-Temperature Polycondensation Approach. *Angewandte Chemie International Edition* **2017**, *56* (45), 14149-14153.
  63. Liu, M.; Jiang, K.; Ding, X.; Wang, S.; Zhang, C.; Liu, J.; Zhan, Z.; Cheng, G.; Li, B.; Chen, H.; Jin, S.; Tan, B., Controlling Monomer Feeding Rate to Achieve Highly Crystalline Covalent Triazine Frameworks. *Advanced Materials* **2019**, *31* (19), 1807865.
  64. *Materials Studio 2019*, Dassault Systèmes BIOVIA: San Diego, 2019.
  65. Gaus, M.; Goetz, A.; Elstner, M., Parametrization and Benchmark of DFTB3 for Organic Molecules. *Journal of Chemical Theory and Computation* **2013**, *9* (1), 338-354.
  66. Monkhorst, H. J.; Pack, J. D., Special points for Brillouin-zone integrations. *Physical Review B* **1976**, *13* (12), 5188-5192.
  67. Kresse, G.; Furthmüller, J., Efficiency of ab-initio total energy calculations for metals and semiconductors using a plane-wave basis set. *Computational Materials Science* **1996**, *6* (1), 15-50.
  68. Kresse, G.; Furthmüller, J., Efficient iterative schemes for ab initio total-energy calculations using a plane-wave basis set. *Physical Review B* **1996**, *54* (16), 11169-11186.
  69. Perdew, J. P.; Burke, K.; Ernzerhof, M., Generalized Gradient Approximation Made Simple. *Physical Review Letters* **1996**, *77* (18), 3865-3868.
  70. Kresse, G.; Joubert, D., From ultrasoft pseudopotentials to the projector augmented-wave method. *Physical Review B* **1999**, *59* (3), 1758-1775.
  71. Grimme, S.; Antony, J.; Ehrlich, S.; Krieg, H., A consistent and accurate ab initio parametrization of density functional dispersion correction (DFT-D) for the 94 elements H-Pu.

- The Journal of Chemical Physics* **2010**, 132 (15), 154104.
72. Urban, A.; Seo, D.-H.; Ceder, G., Computational understanding of Li-ion batteries. *npj Computational Materials* **2016**, 2 (1), 16002.
  73. Sun, H.; Jin, Z.; Yang, C.; Akkermans, R. L. C.; Robertson, S. H.; Spenley, N. A.; Miller, S.; Todd, S. M., COMPASS II: extended coverage for polymer and drug-like molecule databases. *Journal of Molecular Modeling* **2016**, 22 (2), 47.
  74. Henkelman, G.; Arnaldsson, A.; Jónsson, H., A fast and robust algorithm for Bader decomposition of charge density. *Computational Materials Science* **2006**, 36 (3), 354-360.
  75. Ewald, P. P., Die Berechnung optischer und elektrostatischer Gitterpotentiale. *Annalen der Physik* **1921**, 369 (3), 253-287.
  76. Tosi, M. P., Cohesion of Ionic Solids in the Born Model\*\*Based on work performed under the auspices of the U.S. Atomic Energy Commission. In *Solid State Physics*, Seitz, F.; Turnbull, D., Eds. Academic Press: 1964; Vol. 16, pp 1-120.

## Chapter 5. Polymorphism of Poly(vinylidene fluoride) Binder Material

*This chapter includes the following contents:*

Song, W.-J.<sup>†</sup>; Joo, S. H.<sup>†</sup>; Kim, D. H.<sup>†</sup>; Hwang, C.; Jung, G. Y.; Bae, S.; Son, Y.; Cho, J.; Song, H.-K.; Kwak, S. K.\*; Park, S.\*; Kang, S. J.\*, Significance of ferroelectric polarization in poly (vinylidene difluoride) binder for high-rate Li-ion diffusion. *Nano Energy* **2017**, *32*, 255-262. (†: **equally contributed**). Reproduced with permission from Elsevier Ltd., copyright 2016.<sup>1</sup>

---

### 5.1 Introduction

High-rate, high-capacity rechargeable batteries have great potential for direct applications in the exponentially growing battery powered transportation system.<sup>2,3</sup> Compared with the classic combustion engine, electric motors offer several technical and environmental advantages such as quiet, vibration free, and eco-friendly performance, which can open up a rapid growth electric vehicle (EV) market and lead the way for a large mega trend in personal electric transportation devices.<sup>4,5</sup> However, electric motor-based EVs rely strongly upon a secondary battery system, more precisely, a Li-ion battery (LIB) of which the range and charging speed are usually set by the performance of the active electrode materials.<sup>6-8</sup> Although recent LIB technology gives an approximate 100-mile range with overnight charging speed, there is a strong need for improving battery performance, particularly for capacity and rate of charging. Consequently, significant efforts have been devoted to improving high-performance LIBs by obtaining new LIB materials such as cathodes, anodes, electrolytes and separators as well as controlling the Li-ion and electron diffusion properties during the charging and discharging process.<sup>9-12</sup> For example, various innovative cathode and anode materials, which include newly developed nanostructures,<sup>13-15</sup> electrode surface modifications,<sup>16-18</sup> hybrid-composites,<sup>19-21</sup> and unique electrode architectures,<sup>22-25</sup> have been successfully formed in last decade, from many different research groups, that show excellent properties; however, the proposed ideas and smart materials exhibit decreased capacity at high current rates, which is, in general, an undesirable property for high-rate LIBs. One of the vexing problems is that lack of Li-ion concentration inevitably occurs at high current rates mainly owing to the concentration difference in the consumed and supplied Li-ions on the active material surface.<sup>9</sup> Recently, Xia et al. successfully demonstrated the new strategy for high-rate LIBs with lower Li-ion diffusion resistance by using surface-amorphized TiO<sub>2</sub> nanocrystals.<sup>26</sup> The key mechanism behind this research is that amorphized TiO<sub>2</sub> nanocrystals effectively generate a built-in potential in the vicinity of the electrode, enabling a reduction in the Li-ion resistance (lithium charge transfer resistance)

during the discharge and charge process. This result also suggests that suitable surface polarization on the active material is another key parameter for making high-performance LIBs.

Considering surface polarization, fluorine-containing organic polymers such as poly(vinylidene fluoride) (PVDF) and its derivatives have been commonly used for binder materials in commercial LIBs because of their inertness to organic solvents and good physical/chemical stability at high operating voltages.<sup>27</sup> Although they have only been used for binding nano- or micrometer-scale active electrode materials in LIBs, major applications for PVDF and its derivatives are functional dielectric materials for capacitor and field effect transistor devices owing to the permanent dipole between fluorine and hydrogen atoms in the chain backbone.<sup>28-30</sup> Although it is rarely considered in the battery field, PVDF is a semicrystalline polymer exhibiting polymorphism and is known to form at least four different polymorphs, referred to as  $\alpha$ ,  $\beta$ ,  $\gamma$ ,  $\delta$ , depending on its chain conformation and chain packing in a crystal (**Figure 5.1**).<sup>30-32</sup> Specifically, it has been observed that there are three chain conformations as a combination of trans (*t*) form with torsion angle of  $180^\circ$  and gauche (*g* $\pm$ ) form with torsion angle of  $\pm 120^\circ$  and two chain packing modes: *tttt*, *tg<sup>+</sup>tg<sup>-</sup>*, and *tttg<sup>+</sup>tttg<sup>-</sup>* conformations, and parallel and antiparallel packing modes. Different polymorphs exhibit different strength of polarization, and thus different behaviors such as ferroelectric or paraelectric properties. Although the ferroelectric property can be similarly utilized by the built-in potential in the LIB field, controlling the phase of the PVDF binder is rarely demonstrated.

In this contribution, we investigated the effect of the crystalline phase of the PVDF binder in the anode and cathode electrodes, particularly for two abundant polymorphs  $\alpha$ - and  $\beta$ -phases. The ferroelectric PVDF, known in the  $\beta$ -phase, binder is developed by an appropriate thermal annealing process that allows us to apply it to various active battery electrode materials without changing the ratio of the binder content. The active electrodes containing the ferroelectric PVDF binder exhibit greatly improved capacity performance at high current rates in both half- and full-cell architectures. To understand the origin of this promising battery performance, we theoretically studied the ferroelectric contribution of PVDF binder in the battery system by using density functional theory (DFT) calculations. The results imply that surface polarization can effectively reduce resistance during battery operation, suggesting that the polarization characteristics of binder material are a viable design strategy to enhance the battery performance.

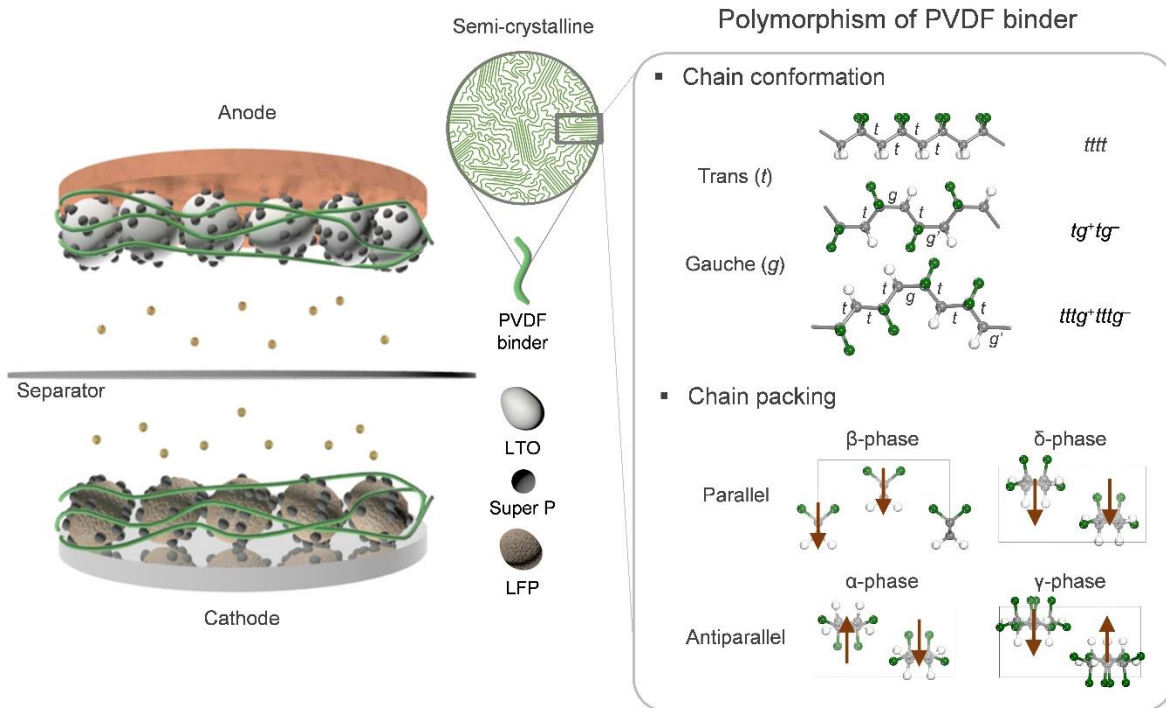


**Figure 5.1** Schematic representation of a full-cell LIB containing semicrystalline PVDF binder that can form various polymorphs depending on chain conformation and chain packing mode. Reproduced from ref. 1 with permission from Elsevier Ltd., copyright 2016.

## 5.2 Computational Methods

### 5.2.1 Density Functional Theory Calculations

Density functional theory (DFT) calculations were performed using CASTEP in Materials Studio 2016.<sup>33,34</sup> Generalized gradient approximation parameterized by Perdew-Burke-Ernzerhof (GGA-PBE) was used to describe the exchange-correlation energy of electrons.<sup>35</sup> On-the-fly generation ultrasoft pseudopotential was used to describe the interaction between electron and ion. Semi-empirical dispersion-correction using Tkatchenko and Scheffler's scheme and spin polarization were taken into account in all calculations.<sup>36</sup> The electronic wavefunctions were expanded in terms of a plane-wave basis set with energy cutoff of 600.0 eV. With Monkhorst-Pack scheme,<sup>37</sup>  $k$ -point separations less than  $0.07 \text{ \AA}^{-1}$  and  $0.04 \text{ \AA}^{-1}$  in reciprocal space were employed for geometry optimization and calculation of electronic properties, respectively. The convergence criterion for self-consistent field calculation was set to  $5.0 \times 10^{-7}$  eV/atom. The convergence criteria for geometry optimization were set to  $5.0 \times 10^{-6}$  eV/atom for the maximum energy change,  $0.01 \text{ eV/\AA}$  for the maximum force,  $0.02 \text{ GPa}$  for the maximum stress, and  $5.0 \times 10^{-6} \text{ \AA}$  for the maximum displacement. Smearing was introduced with the value of  $0.1 \text{ eV}$  and self-consistent dipole correction was applied along  $z$ -axis. The atomic charges of PVDF were estimated using Mulliken population analysis.<sup>38-40</sup>

The crystal structures of  $\alpha$ -PVDF unit cell and  $2 \times 1 \times 1$  supercell of  $\beta$ -PVDF were optimized by relaxing both the cell parameters and atomic positions. Using the optimized crystal structures, PVDF surface was modeled as a periodic slab consisting of 8 molecular layers of PVDF. For  $\beta$ -PVDF, slab models consisting of 1, 2, 4, 8, and 16 molecular layers were also constructed. For both  $\alpha$ - and  $\beta$ -PVDF surfaces, two types of termination are possible along the direction of the electric dipole moment: F-terminated and H-terminated surfaces. Considering the crystal structures and surface terminations, four different types of slab models were constructed for F-terminated and H-terminated surfaces of  $\alpha$ - and  $\beta$ -PVDF. It is noteworthy that  $\alpha$ -PVDF slab models have same terminations at top and bottom surfaces, while  $\beta$ -PVDF slab models have both F-terminated and H-terminated surfaces. In each model, the atomic positions of bottom 4 molecular layers were fixed to describe bulk-like structure. To minimize the interactions between periodic slabs along  $z$ -axis, the cell parameter  $c$  was adjusted to  $40 \text{ \AA}$ ; exceptionally, it is adjusted to  $80 \text{ \AA}$  for the slab model consisting of 16 molecular layers.

For PVDF surface, work function  $W$ , the energy needed to remove an electron from surface to vacuum level, was calculated by the difference between the potential energy of an electron in the vacuum and the Fermi level,

$$W = -e\phi - E_F$$

where  $-e$ ,  $\phi$ , and  $E_F$  represent the charge of an electron, the electrostatic potential, and the Fermi level, respectively.

The adsorption energy of Li on PVDF surface was calculated by following equation,

$$\Delta E_{ads} = E_{PVDF+Li} - E_{PVDF} - E_{Li}$$

where  $E_{PVDF+Li}$ , is the total energy of Li-adsorbed PVDF surface;  $E_{PVDF}$  and  $E_{Li}$  are energies of bare PVDF surface and Li atom in gas phase, respectively.

## 5.2.2 Molecular Dynamics Simulation

To find energetically preferable polarization orientation of ferroelectric  $\beta$ -PVDF on  $\text{LiFePO}_4$  (LFP) surface, molecular dynamics (MD) simulations were performed using Materials Studio 2016.<sup>33</sup> Universal force field with Mulliken charges obtained from DFT calculations was used to describe the interactions between the PVDF and LFP surface.<sup>41</sup> Short-range van der Waals interactions were calculated with cutoff distance of 12.5 Å and long-range electrostatic interactions were evaluated by Ewald summation method.<sup>42, 43</sup> Newton's equations of motion were integrated by velocity Verlet algorithm with a time step of 1 fs.<sup>44</sup> MD simulations were performed under canonical ensemble. The temperature was controlled by Berendsen thermostat with a decay constant of 0.1 ps.<sup>45</sup> Periodic boundary conditions were applied in all three directions. For constructing model system, the 35-mer PVDF chain with all-trans (*tttt*) conformation and the  $22 \times 10 \times 2$  stoichiometric LFP (010) surface slab were employed. To minimize the interactions between periodic images along  $z$ -direction, the height of the simulation box was adjusted to 150 Å. The PVDF chain was placed above the LFP (010) surface with the initial polarization direction vertical to the substrate. Two different polarization directions perpendicular to the substrate, namely upward and downward directions, were considered. The PVDF chain was equilibrated at 298 K for 500 ps, while the atomic positions of the LFP were kept fixed. To further investigate the origin of preferable orientation of the PVDF chain on the LFP surface, we calculated the interaction energy profile with respect to the rotation angle between the polarization direction and the surface normal vector. The 5-mer PVDF chain with *tttt* conformation and the  $5 \times 2 \times 2$  stoichiometric LFP (010) surface slab were employed for the calculations.



## 5.3 Results and Discussion

### 5.3.1 Crystal Structure of $\alpha$ - and $\beta$ -PVDF

The crystal structures of  $\alpha$ - and  $\beta$ -PVDF, two most abundant polymorphs of PVDF, are markedly different in terms of chain conformation and chain packing (**Figure 5.2**). The  $\alpha$ -PVDF consists of chains with the  $tg^+tg^-$  conformation in the antiparallel manner. Therefore, there is no net dipole moment in the resulting crystal. On the other hand, the  $\beta$ -PVDF consists of chains with the  $tttt$  conformation in the parallel manner, which leads to the strong spontaneous polarization. To investigate the effect of these differences, especially the difference in polarization characteristics, on battery performance, we investigated the electronic properties of  $\alpha$ - and  $\beta$ -PVDF and their interactions with Li-ion, which is closely related to the electron and ion transport, respectively.

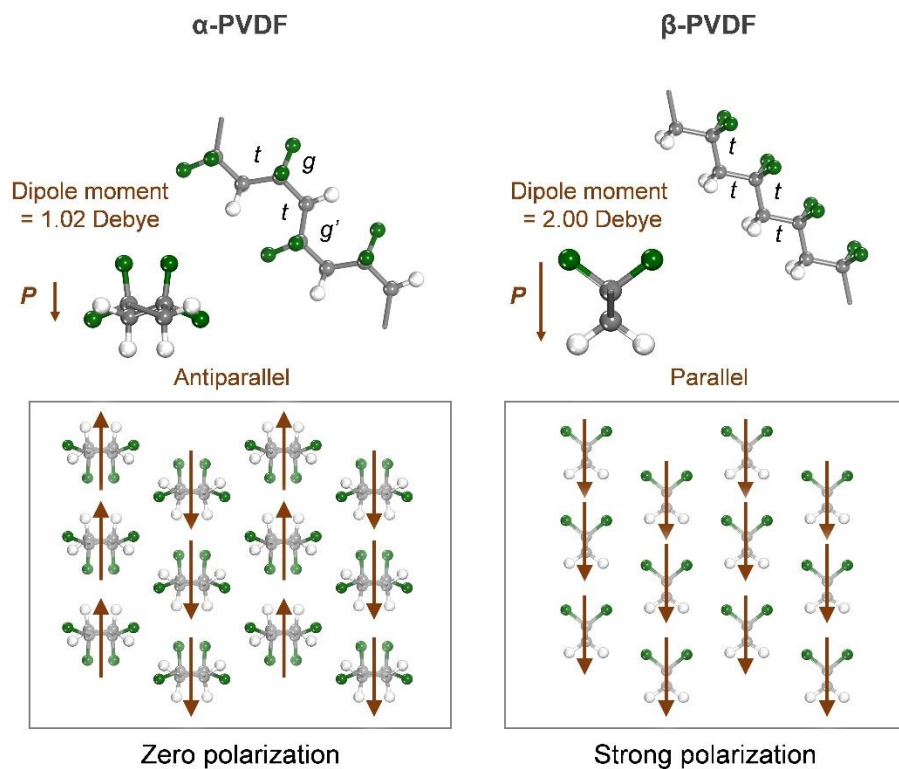


**Figure 5.2** Crystal structure, chain conformation, chain packing, and polarization characteristic of  $\alpha$ - and  $\beta$ -PVDF. Carbon, fluorine, and hydrogen are grey, green, and white, respectively. The brown arrows indicate the dipole direction of each chain.

### 5.3.2 Electronic Structure of $\alpha$ - and $\beta$ -PVDF

In order to investigate the effect of the ferroelectric polarization on the electronic properties, we investigated the molecular layer-projected electronic density of states (DOS) for both paraelectric  $\alpha$ -PVDF and ferroelectric  $\beta$ -PVDF. **Figure 5.3** shows the DOS of slab models for F-terminated  $\alpha$ - and  $\beta$ -PVDF surfaces. For the paraelectric  $\alpha$ -PVDF, we observed no shift in local bands in the total DOS (**Figure 5.3a**). For the ferroelectric  $\beta$ -PVDF, however, spontaneous polarization was generated in the direction of the electronegative fluorine ( $-q$ ) to the electropositive hydrogen ( $+q$ ) and local bands of each PVDF layer were downshifted along the polarization direction (**Figure 5.3b**). Resultingly, the valence band of topmost layer in F-terminated surface and the conduction band of bottommost layer in the H-terminated surface crossed the Fermi level, leading to the surface metallization and zero band gap in the total DOS.<sup>46</sup> The same phenomenon was observed with the H-terminated surface. **Figure 5.4** shows the DOS of slab models for H-terminated  $\alpha$ - and  $\beta$ -PVDF surfaces. Overall, for both  $\alpha$ - and  $\beta$ -PVDF, the electronic properties of slab models for H-terminated surfaces were similar to those for F-terminated surfaces. It is worth noting that as the  $\beta$ -PVDF slab model for H-terminated surface has the upturned structure of that for F-terminated surface, the energy shifts of local bands occur in the opposite direction.

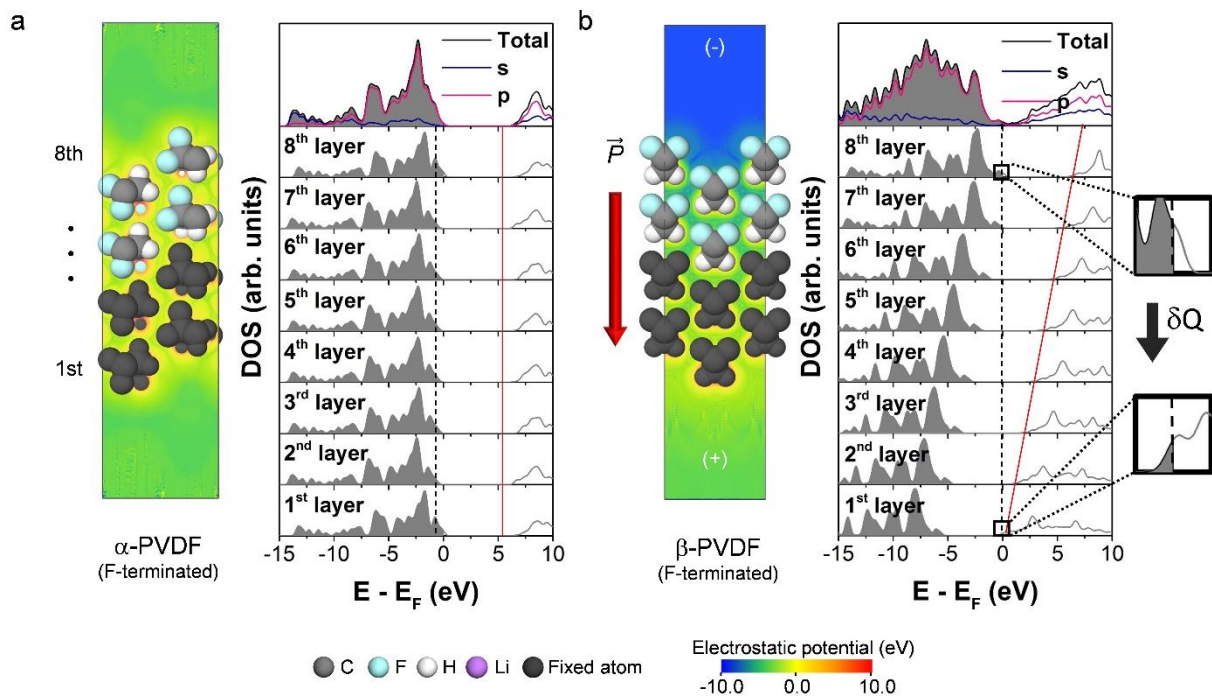


**Figure 5.3** The electrostatic potential map (left panel) and the total and layer-projected DOS (right panel) of (a)  $\alpha$ -PVDF and (b)  $\beta$ -PVDF slab models with F-terminated surfaces, respectively. Reproduced from ref. 1 with permission from Elsevier Ltd., copyright 2016.

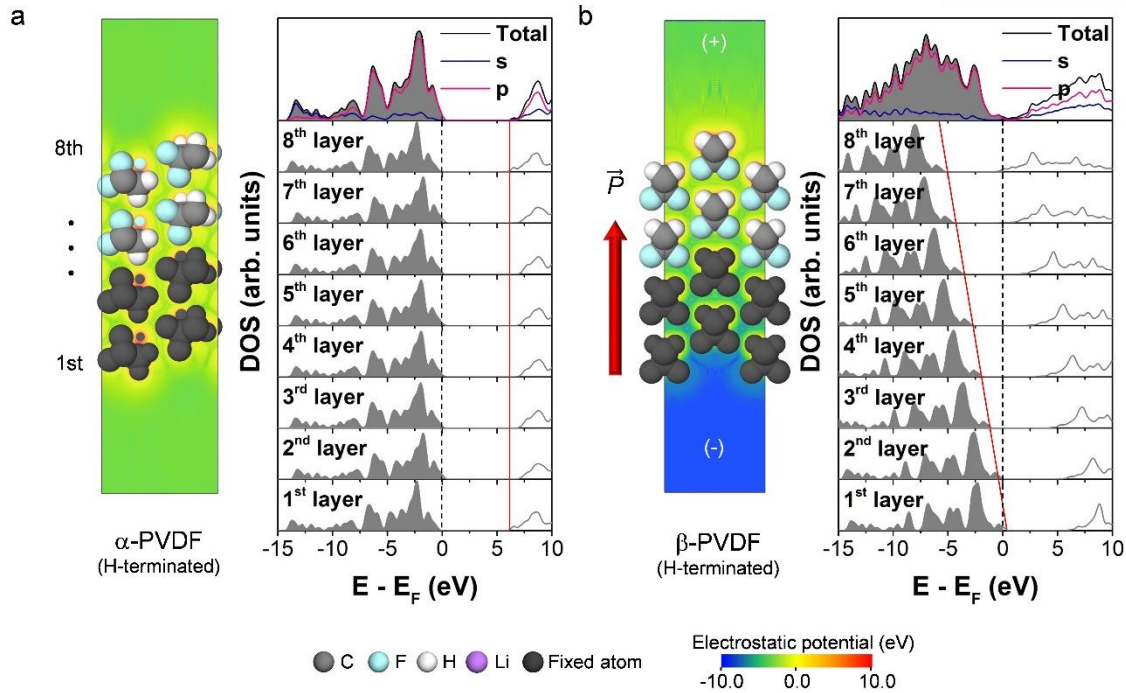


**Figure 5.4** The electrostatic potential map (left panel), the total and layer-projected DOS (right panel) of (a)  $\alpha$ -PVDF and (b)  $\beta$ -PVDF slab models with H-terminated surfaces, respectively. Reproduced from ref. 1 with permission from Elsevier Ltd., copyright 2016.

The electronic properties of PVDF can be influenced by the thickness of PVDF molecular films.<sup>47</sup> To demonstrate the dependency of polarization effect and the electronic properties of  $\beta$ -PVDF on the number of molecular layers, we analyzed the electronic DOS with increasing the number of molecular layers up to 16 without any relaxation (**Figure 5.5a**). As shown in **Figure 5.5b**, the band gap of  $\beta$ -PVDF becomes zero with increasing number of molecular layers. After the gap is closed when the number of molecular layers is more than 4, the shape of total DOS becomes smooth without any dramatic change near Fermi-level. Considering that the electronic states near Fermi-level are mainly contributed from both outermost surfaces, the molecular layer-projected DOS of H- and F-terminated surfaces were also analyzed (blue and red dashed circles in **Figure 5.5a**). As shown in **Figure 5.5c**, the local bands of F-terminated surface did not show any shift with increasing the number of molecular layers. On the other hand, the local bands of H-terminated surface were shifted downward, resulting in the overlap of conduction band and Fermi-level (**Figure 5.5d**). As the energy shifts of DOS are converged from the 4 molecular layers, PVDF consisting of more than 4 molecular layers is expected to show the similar electronic properties as those of bulk system. In other words, the surface metallicity of the ferroelectric  $\beta$ -PVDF phase began to appear over four molecular layers. The results imply that the surface metallicity, driven by ferroelectric polarization of  $\beta$ -PVDF, plays a crucial role in reducing charge transfer resistance.

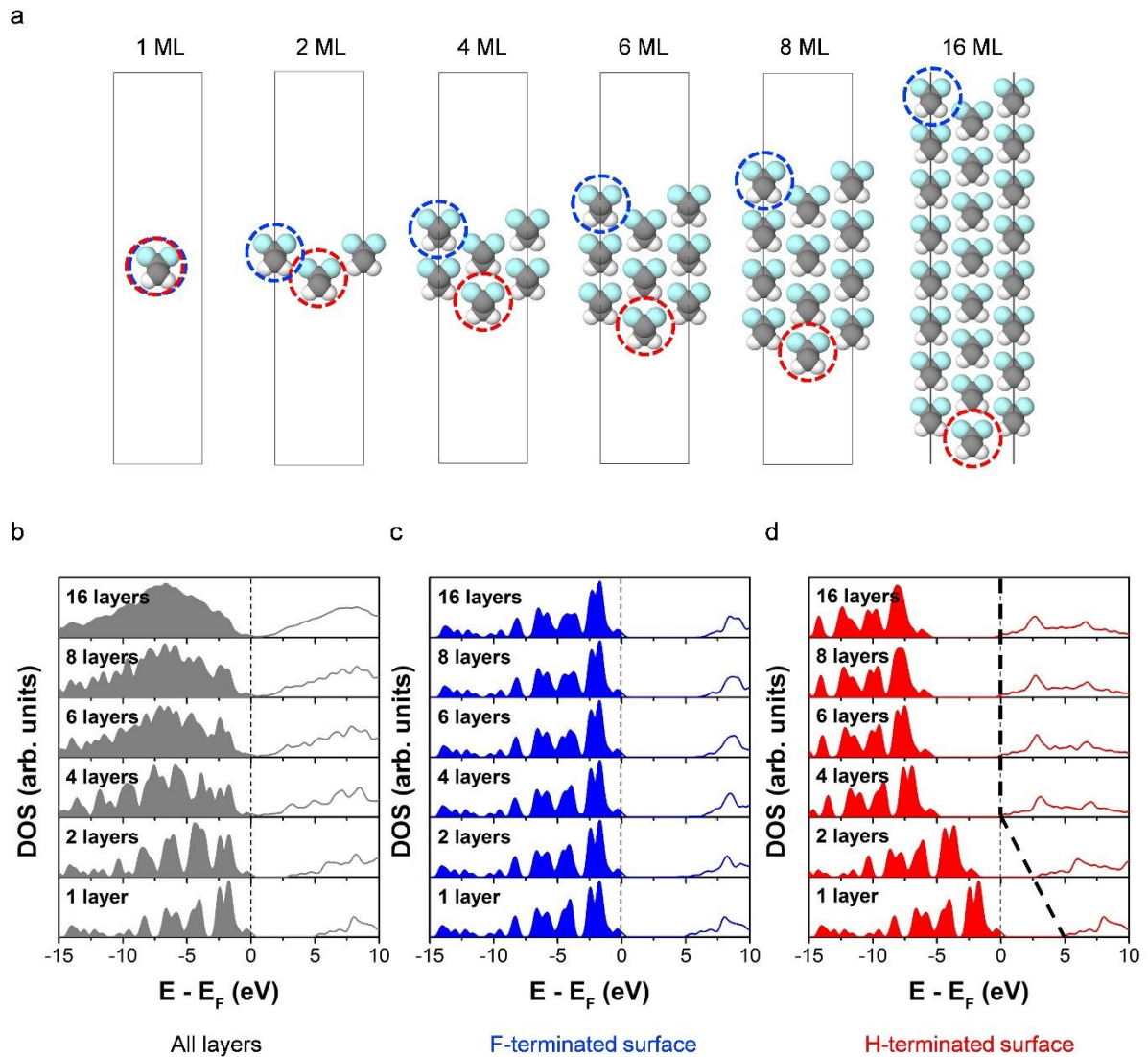


**Figure 5.5** (a) The slab models of  $\beta$ -PVDF with different number of molecular layers (ML) from 1 to 16. Blue and red dashed circles depict F-terminated surface and H-terminated surfaces, respectively. Carbon, fluorine, hydrogen, and fixed atoms are grey, cyan, white, and dark grey colors, respectively. (b) Total DOS for all layers. Layer-projected DOS for (c) F-terminated and (d) H-terminated surfaces, respectively. Reproduced from ref. 1 with permission from Elsevier Ltd., copyright 2016.

### 5.3.3 Internal Electron Transfer of $\alpha$ - and $\beta$ -PVDF

More specifically, to explore the electron transfer mechanism seen in PVDF, we investigated molecular layer-resolved electron transfer of  $\alpha$ - and  $\beta$ -PVDF surfaces (**Figure 5.6**). The amount of electron transfer between each layer in  $\alpha$ -PVDF was negligible (**Figure 5.6a,c**), whereas that in  $\beta$ -PVDF surface was significantly increased (**Figure 5.6b,d**). This phenomenon likely occurs because a portion of states in the valence band of the topmost layer (i.e., the 8th layer), which exceeds the Fermi level, helps electrons to transfer to the conduction band of the bottommost layer (i.e., the 1st layer) (**Figure 5.7**); electrons are depleted on the F-terminated surface but excessed on the H-terminated surface. Thus, good charge transfer is expected to occur internally within  $\beta$ -PVDF along the polarization direction.

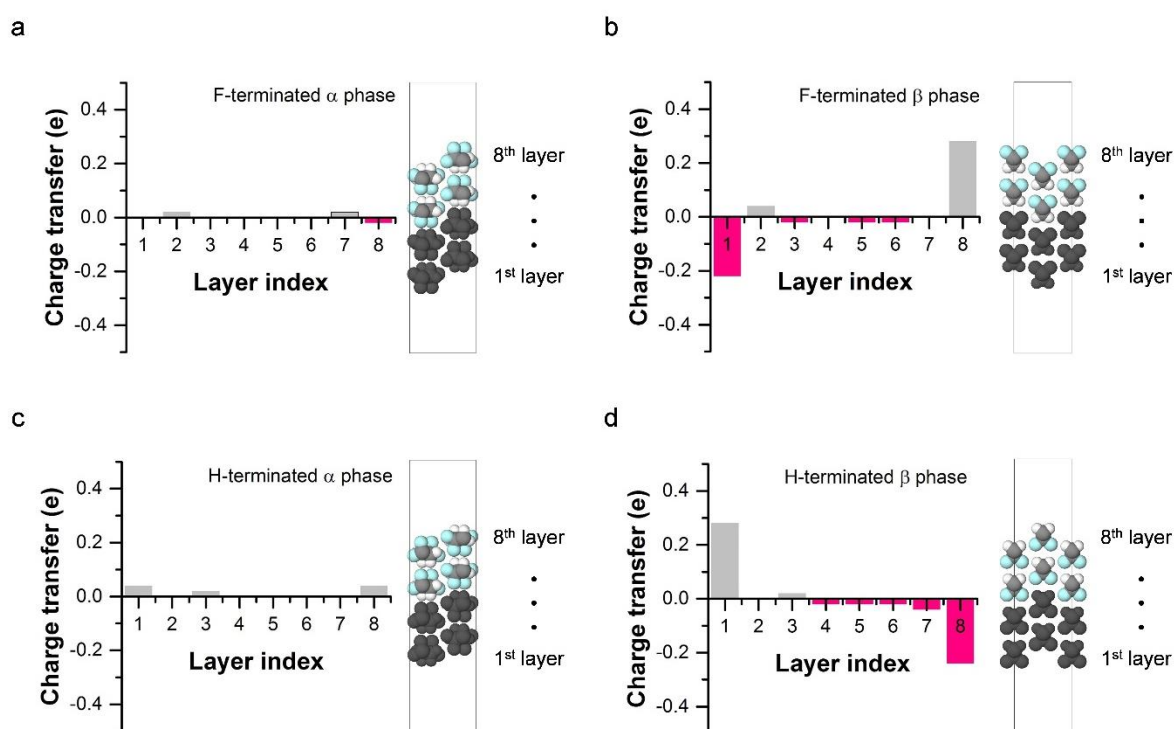


**Figure 5.6** Charge transfer in the slab models for (a) F-terminated  $\alpha$ -PVDF surface, (b) F-terminated  $\beta$ -PVDF surface, (c) H-terminated  $\alpha$ -PVDF surface, and (d) H-terminated  $\beta$ -PVDF surface. Carbon, fluorine, hydrogen, and fixed atoms are grey, cyan, white, and dark grey, respectively. Reproduced from ref. 1 with permission from Elsevier Ltd., copyright 2016.



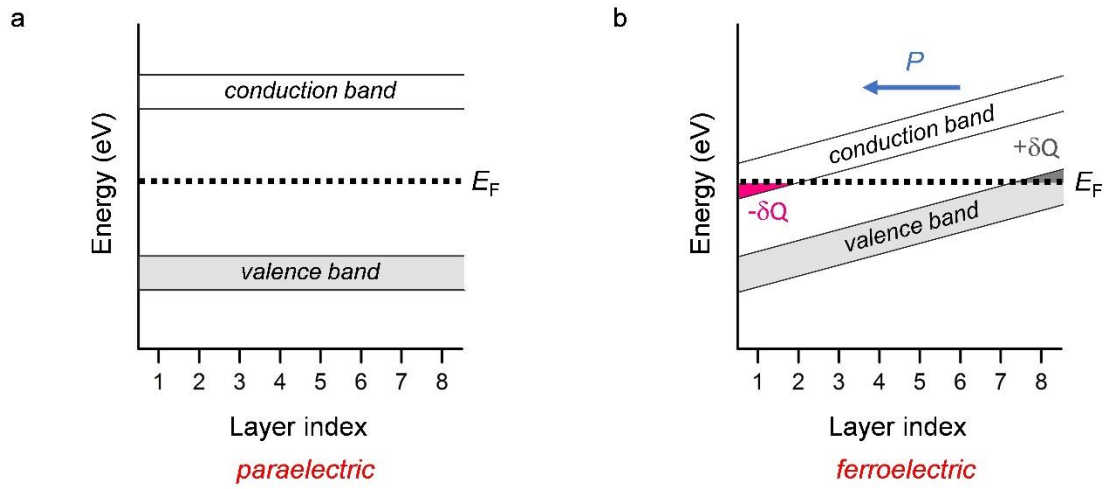


**Figure 5.7** Schematic diagram of charge transfer in (a)  $\alpha$ -PVDF and (b)  $\beta$ -PVDF. Reproduced from ref. 1 with permission from Elsevier Ltd., copyright 2016.

### 5.3.4 Work Function of $\alpha$ - and $\beta$ -PVDF

Furthermore, in order to elucidate overall electron transfer mode through electronic channels consisting of each layer, the work function ( $W$ ), which allows predicting a degree of electron affinity with external environment, was estimated by electrostatic potential calculations (**Figure 5.8**). For  $\alpha$ -PVDFs with F- and H-terminated surfaces, the constant levels of the electrostatic potentials for each layer led to similar values of the work functions (**Figure 5.8a,c**). On the other hand, for  $\beta$ -PVDF, the electrostatic potentials gradually varied along the polarization direction, resulting in the variation of work function to a large extent. As a result, the work function is  $W = 8.3$  eV for F-terminated surface and  $W = 1.6$  eV for H-terminated surface (**Figure 5.8b,d**). Thus, for  $\beta$ -PVDF, externally delivered electrons preferably bind to the electron-depleted F-terminated surface and exit from the H-terminated surface.

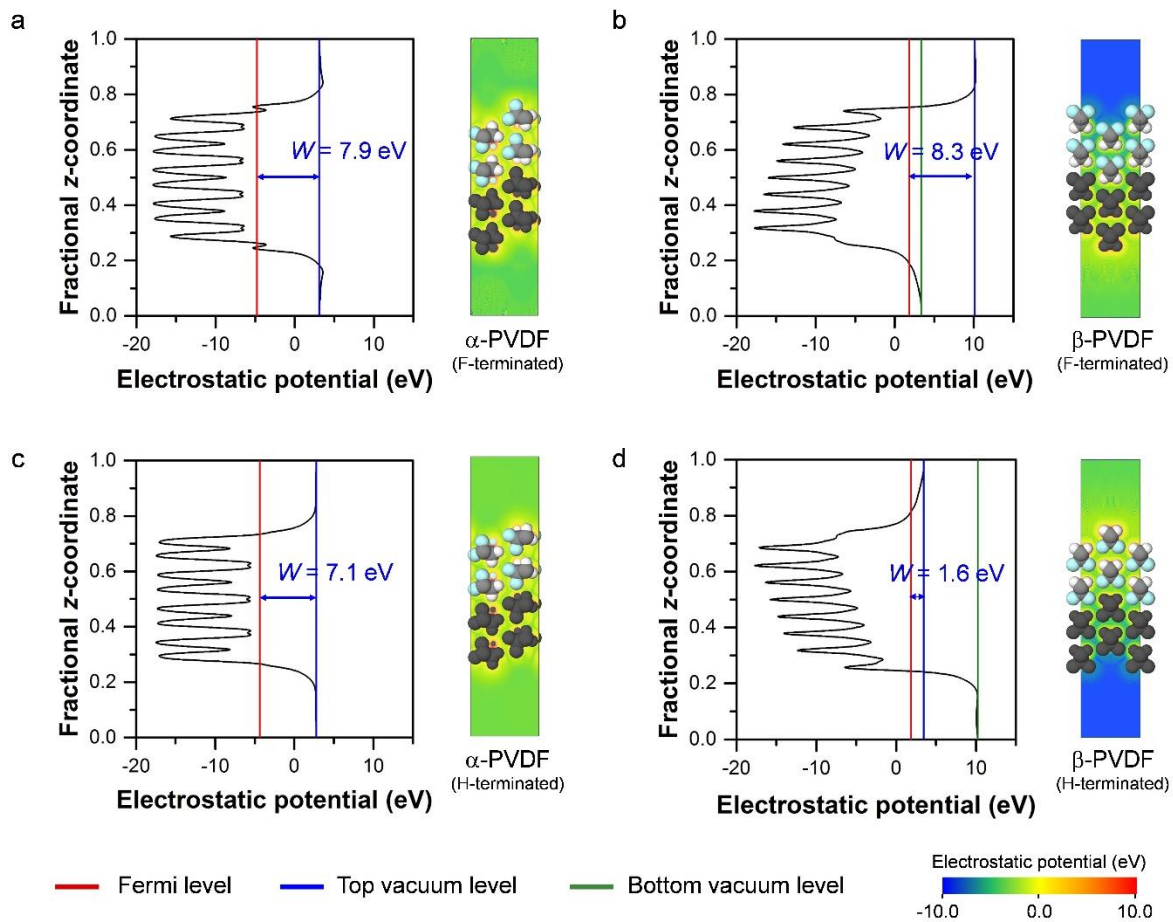


**Figure 5.8** Profiles of  $xy$ -plane averaged electrostatic potential along the  $z$ -axis of slab models for (a) F-terminated  $\alpha$ -PVDF surface, (b) F-terminated  $\beta$ -PVDF surface, (c) H-terminated  $\alpha$ -PVDF surface, and (d) H-terminated  $\beta$ -PVDF surface.  $W$  denotes the work function of each surface. Reproduced from ref. 1 with permission from Elsevier Ltd., copyright 2016.



### 5.3.5 Li Binding Affinity of $\alpha$ - and $\beta$ -PVDF

Also, the binding affinity of Li-ion was estimated by calculating its adsorption energy ( $\Delta E_{\text{ads}}$ ) on each PVDF surface (**Figure 5.9**). Overall, the adsorption energies on H-terminated surfaces were lower than those on F-terminated surfaces for both  $\alpha$ - and  $\beta$ -PVDF. More importantly,  $\Delta E_{\text{ads}}$ 's on  $\beta$ -PVDF surfaces were larger than those on  $\alpha$ -PVDF surfaces regardless of surface terminations. In particular, the F-terminated  $\beta$ -PVDF surface ( $\Delta E_{\text{ads}} = -3.04$  eV) exhibited much higher binding affinity than the F-terminated  $\alpha$ -PVDF surface ( $\Delta E_{\text{ads}} = -0.72$  eV). Although the adsorption energy difference between  $\alpha$ - and  $\beta$ -PVDF for H-terminated surfaces was smaller than that for F-terminated surfaces,  $\beta$ -PVDF still exhibited higher binding affinity to Li-ion than  $\alpha$ -PVDF ( $\Delta E_{\text{ads}} = -0.61$  eV for  $\alpha$ -PVDF and  $\Delta E_{\text{ads}} = -0.89$  eV for  $\beta$ -PVDF). The result indicates that the ferroelectric polarization in  $\beta$ -PVDF, which enhances the binding affinity of Li-ions, promotes the access to Li-ion toward the electrode surface (**Figure 5.10**).

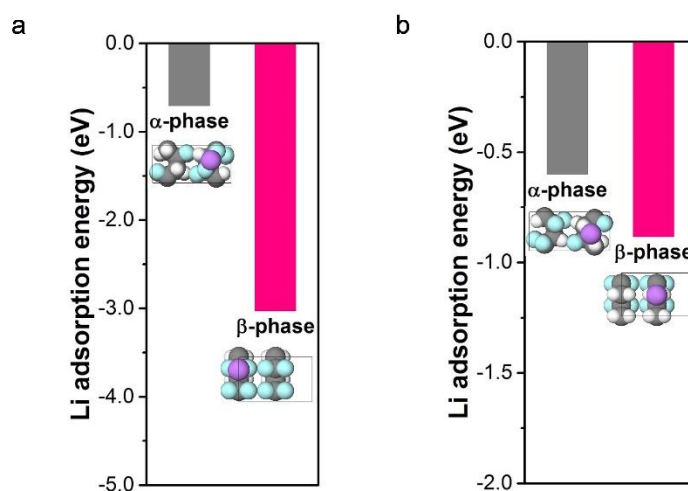


**Figure 5.9** (a) Adsorption energy of Li-ion on F-terminated  $\alpha$ - and  $\beta$ -PVDF surfaces. (b) Adsorption energy of Li-ion on H-terminated  $\alpha$ - and  $\beta$ -PVDF surfaces. Carbon, fluorine, hydrogen, lithium and fixed atoms are grey, cyan, white, purple and dark grey, respectively. Reproduced from ref. 1 with permission from Elsevier Ltd., copyright 2016.

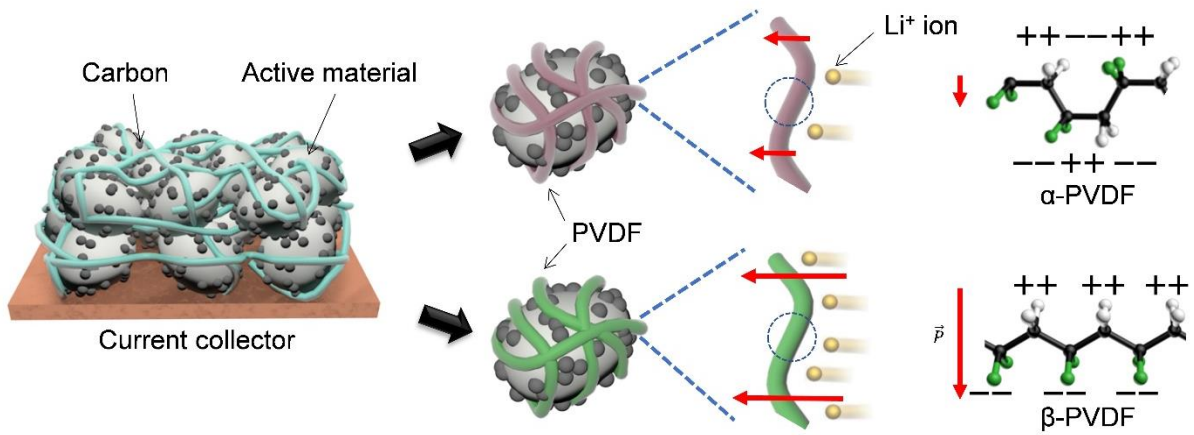


**Figure 5.10** Schematic illustration of a LIB electrode using ferroelectric and paraelectric PVDF binder. Reproduced from ref. 1 with permission from Elsevier Ltd., copyright 2016.

### 5.3.6 Polarization Direction of $\beta$ -PVDF on LFP

However, if the polarization direction is perpendicular to the substrate, one of the Li-ion transport direction during the battery operation can be hindered by the repulsive force from PVDF dipoles. In order to resolve this contradictory issue, we performed additional molecular dynamics (MD) simulation with  $\beta$ -PVDF conformation on the active electrode as a function of rotation angle of PVDF chain backbone. During the MD simulations, the PVDF chain changed its orientation so that the dipole moment of each  $\text{CF}_2\text{-CH}_2$  repeat unit became parallel to the LFP surface as shown in **Figure 5.11**. The result demonstrated that the interaction energy between PVDF and LFP surface became stronger only when the polarization axis is parallel to the substrate (**Figure 5.12**). Thus, the parallel orientation is considered thermodynamically favored and applicable for facilitating Li-ion transport for both discharge and charge process.

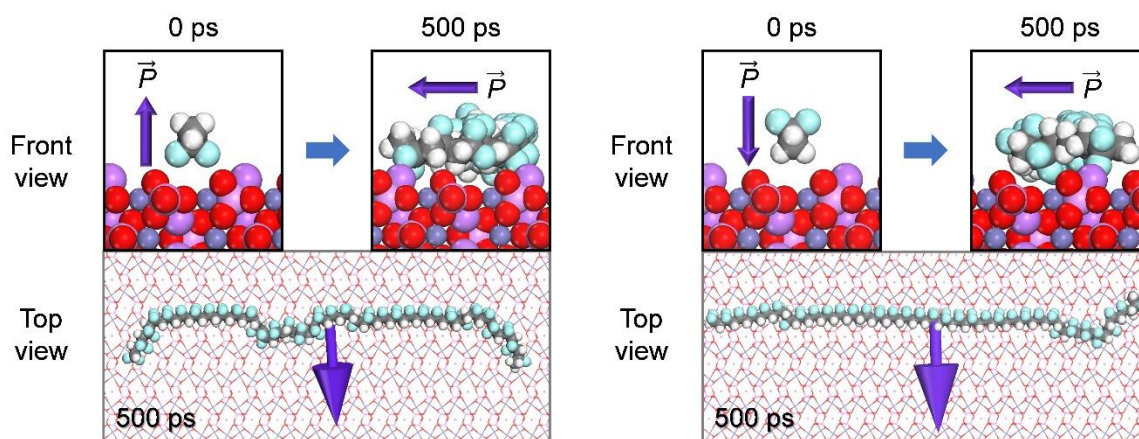


**Figure 5.11** MD simulation snapshots of a 35-mer PVDF chain on LFP (010) surface. Two different polarization directions, which were vertical to the surface, were considered (upward (left) and downward (right) directions). Purple arrow represents the direction of net dipole moment of PVDF. Carbon, fluorine, hydrogen, lithium, iron, and oxygen atoms are grey, cyan, white, dark blue, light pink, and red, respectively. Reproduced from ref. 1 with permission from Elsevier Ltd., copyright 2016.

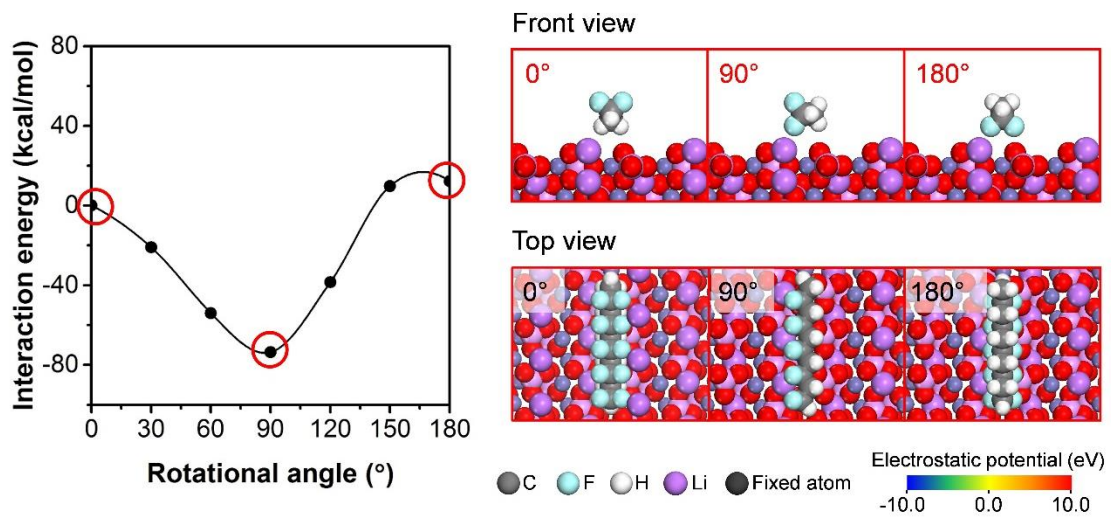


**Figure 5.12** Interaction energy profile with respect to the rotation angle of a 5-mer PVDF chain on the LFP (010) surface. Carbon, fluorine, hydrogen, lithium, iron, oxygen and fixed atoms are grey, cyan, white, dark blue, light pink, red, and dark grey, respectively. Reproduced from ref. 1 with permission from Elsevier Ltd., copyright 2016.

## 5.4 Conclusion

In conclusion, we hypothesized and tested the idea that a ferroelectric  $\beta$ -PVDF binder can effectively transport electrons and Li-ions in a LIB system. Our systematic theoretical study clearly revealed that strong polarization on the active electrodes induced by a ferroelectric binder directly affects diffusion of electron and Li-ion during battery operation. The ferroelectric polarization induced surface metallization, internal electron transfer, and the variation of work function, which can expedite electron diffusion and reduce charge transfer resistance. Moreover, the interaction between a polarized  $\beta$ -PVDF surface and Li-ions was over four times higher than in a paraelectric  $\alpha$ -PVDF binder, which can facilitate Li-ion diffusion. The promotion of the access of Li-ions toward electrode surface reduces charge transfer resistance by alleviating lack of Li-ion concentration, which inevitably occurs a high current rate. Overall,  $\beta$ -PVDF is expected to result in greatly improved capacity with lower cell resistance, compared to a paraelectric  $\alpha$ -PVDF binder-containing cell. We believe that our results open a new strategy for the design of binders for high-rate secondary batteries.

## 5.5 References

1. Song, W.-J.; Joo, S. H.; Kim, D. H.; Hwang, C.; Jung, G. Y.; Bae, S.; Son, Y.; Cho, J.; Song, H.-K.; Kwak, S. K.; Park, S.; Kang, S. J., Significance of ferroelectric polarization in poly (vinylidene difluoride) binder for high-rate Li-ion diffusion. *Nano Energy* **2017**, *32*, 255-262.
2. Chu, S.; Majumdar, A., Opportunities and challenges for a sustainable energy future. *Nature* **2012**, *488* (7411), 294-303.
3. Dunn, B.; Kamath, H.; Tarascon, J.-M., Electrical Energy Storage for the Grid: A Battery of Choices. *Science* **2011**, *334* (6058), 928.
4. Thackeray, M. M.; Wolverton, C.; Isaacs, E. D., Electrical energy storage for transportation—approaching the limits of, and going beyond, lithium-ion batteries. *Energy & Environmental Science* **2012**, *5* (7), 7854-7863.
5. Etacheri, V.; Marom, R.; Elazari, R.; Salitra, G.; Aurbach, D., Challenges in the development of advanced Li-ion batteries: a review. *Energy & Environmental Science* **2011**, *4* (9), 3243-3262.
6. Goodenough, J. B.; Park, K.-S., The Li-Ion Rechargeable Battery: A Perspective. *Journal of the American Chemical Society* **2013**, *135* (4), 1167-1176.
7. Kang, B.; Ceder, G., Battery materials for ultrafast charging and discharging. *Nature* **2009**, *458* (7235), 190-193.
8. Choi, N.-S.; Chen, Z.; Freunberger, S. A.; Ji, X.; Sun, Y.-K.; Amine, K.; Yushin, G.; Nazar, L. F.; Cho, J.; Bruce, P. G., Challenges Facing Lithium Batteries and Electrical Double-Layer Capacitors. *Angewandte Chemie International Edition* **2012**, *51* (40), 9994-10024.
9. Tang, Y.; Zhang, Y.; Li, W.; Ma, B.; Chen, X., Rational material design for ultrafast rechargeable lithium-ion batteries. *Chemical Society Reviews* **2015**, *44* (17), 5926-5940.
10. Zhu, Y.; Wang, F.; Liu, L.; Xiao, S.; Yang, Y.; Wu, Y., Cheap glass fiber mats as a matrix of gel polymer electrolytes for lithium ion batteries. *Scientific Reports* **2013**, *3* (1), 3187.
11. Prasanth, R.; Shubha, N.; Hng, H. H.; Srinivasan, M., Effect of poly(ethylene oxide) on ionic conductivity and electrochemical properties of poly(vinylidene fluoride) based polymer gel electrolytes prepared by electrospinning for lithium ion batteries. *Journal of Power Sources* **2014**, *245*, 283-291.
12. Zhu, Y.; Wang, F.; Liu, L.; Xiao, S.; Chang, Z.; Wu, Y., Composite of a nonwoven fabric with poly(vinylidene fluoride) as a gel membrane of high safety for lithium ion battery. *Energy & Environmental Science* **2013**, *6* (2), 618-624.

13. Bruce, P. G.; Scrosati, B.; Tarascon, J.-M., Nanomaterials for Rechargeable Lithium Batteries. *Angewandte Chemie International Edition* **2008**, *47* (16), 2930-2946.
14. Poizot, P.; Laruelle, S.; Grugeon, S.; Dupont, L.; Tarascon, J. M., Nano-sized transition-metal oxides as negative-electrode materials for lithium-ion batteries. *Nature* **2000**, *407* (6803), 496-499.
15. Wang, Y.; Cao, G., Developments in Nanostructured Cathode Materials for High-Performance Lithium-Ion Batteries. *Advanced Materials* **2008**, *20* (12), 2251-2269.
16. Wang, Y.-Q.; Gu, L.; Guo, Y.-G.; Li, H.; He, X.-Q.; Tsukimoto, S.; Ikuhara, Y.; Wan, L.-J., Rutile-TiO<sub>2</sub> Nanocoating for a High-Rate Li<sub>4</sub>Ti<sub>5</sub>O<sub>12</sub> Anode of a Lithium-Ion Battery. *Journal of the American Chemical Society* **2012**, *134* (18), 7874-7879.
17. Shin, J.-Y.; Joo, J. H.; Samuelis, D.; Maier, J., Oxygen-Deficient TiO<sub>2-δ</sub> Nanoparticles via Hydrogen Reduction for High Rate Capability Lithium Batteries. *Chemistry of Materials* **2012**, *24* (3), 543-551.
18. Li, C.; Zhang, H. P.; Fu, L. J.; Liu, H.; Wu, Y. P.; Rahm, E.; Holze, R.; Wu, H. Q., Cathode materials modified by surface coating for lithium ion batteries. *Electrochimica Acta* **2006**, *51* (19), 3872-3883.
19. Li, F.-S.; Wu, Y.-S.; Chou, J.; Winter, M.; Wu, N.-L., A Mechanically Robust and Highly Ion-Conductive Polymer-Blend Coating for High-Power and Long-Life Lithium-Ion Battery Anodes. *Advanced Materials* **2015**, *27* (1), 130-137.
20. Wang, H.; Cui, L.-F.; Yang, Y.; Sanchez Casalongue, H.; Robinson, J. T.; Liang, Y.; Cui, Y.; Dai, H., Mn<sub>3</sub>O<sub>4</sub>-Graphene Hybrid as a High-Capacity Anode Material for Lithium Ion Batteries. *Journal of the American Chemical Society* **2010**, *132* (40), 13978-13980.
21. Cui, L.-F.; Yang, Y.; Hsu, C.-M.; Cui, Y., Carbon-Silicon Core-Shell Nanowires as High Capacity Electrode for Lithium Ion Batteries. *Nano Letters* **2009**, *9* (9), 3370-3374.
22. Li, S.; Niu, J.; Zhao, Y. C.; So, K. P.; Wang, C.; Wang, C. A.; Li, J., High-rate aluminium yolk-shell nanoparticle anode for Li-ion battery with long cycle life and ultrahigh capacity. *Nature Communications* **2015**, *6* (1), 7872.
23. Yoo, H.; Lee, J.-I.; Kim, H.; Lee, J.-P.; Cho, J.; Park, S., Helical Silicon/Silicon Oxide Core-Shell Anodes Grown onto the Surface of Bulk Silicon. *Nano Letters* **2011**, *11* (10), 4324-4328.
24. Yao, Y.; McDowell, M. T.; Ryu, I.; Wu, H.; Liu, N.; Hu, L.; Nix, W. D.; Cui, Y., Interconnected Silicon Hollow Nanospheres for Lithium-Ion Battery Anodes with Long Cycle Life. *Nano Letters* **2011**, *11* (7), 2949-2954.
25. Wu, H.; Chan, G.; Choi, J. W.; Ryu, I.; Yao, Y.; McDowell, M. T.; Lee, S. W.;



- Jackson, A.; Yang, Y.; Hu, L.; Cui, Y., Stable cycling of double-walled silicon nanotube battery anodes through solid–electrolyte interphase control. *Nature Nanotechnology* **2012**, *7* (5), 310-315.
26. Xia, T.; Zhang, W.; Murowchick, J.; Liu, G.; Chen, X., Built-in Electric Field-Assisted Surface-Amorphized Nanocrystals for High-Rate Lithium-Ion Battery. *Nano Letters* **2013**, *13* (11), 5289-5296.
27. Winter, M.; Moeller, K.; Besenhard, J.; Nazri, G.; Pistoia, G., Lithium Batteries: Science and Technology. *Nazri, G.-A* **2004**, *148*.
28. Naber, R. C. G.; Tanase, C.; Blom, P. W. M.; Gelinck, G. H.; Marsman, A. W.; Touwslager, F. J.; Setayesh, S.; de Leeuw, D. M., High-performance solution-processed polymer ferroelectric field-effect transistors. *Nature Materials* **2005**, *4* (3), 243-248.
29. Kang, S. J.; Bae, I.; Shin, Y. J.; Park, Y. J.; Huh, J.; Park, S.-M.; Kim, H.-C.; Park, C., Nonvolatile Polymer Memory with Nanoconfinement of Ferroelectric Crystals. *Nano Letters* **2011**, *11* (1), 138-144.
30. Lovinger, A. J., Ferroelectric Polymers. *Science* **1983**, *220* (4602), 1115.
31. Hasegawa, R.; Takahashi, Y.; Chatani, Y.; Tadokoro, H., Crystal Structures of Three Crystalline Forms of Poly(vinylidene fluoride). *Polymer Journal* **1972**, *3* (5), 600-610.
32. Li, M.; Wondergem, H. J.; Spijkman, M.-J.; Asadi, K.; Katsouras, I.; Blom, P. W. M.; de Leeuw, D. M., Revisiting the  $\delta$ -phase of poly(vinylidene fluoride) for solution-processed ferroelectric thin films. *Nature Materials* **2013**, *12* (5), 433-438.
33. *Materials Studio 2016*, BIOVIA Inc.: San Diego, CA.
34. Clark, S. J.; Segall, M. D.; Pickard, C. J.; Hasnip, P. J.; Probert, M. I. J.; Refson, K.; Payne, M. C., First principles methods using CASTEP. *Zeitschrift für Kristallographie - Crystalline Materials* **2005**, *220* (5-6), 567-570.
35. Perdew, J. P.; Burke, K.; Ernzerhof, M., Generalized Gradient Approximation Made Simple. *Physical Review Letters* **1996**, *77* (18), 3865-3868.
36. Tkatchenko, A.; Scheffler, M., Accurate Molecular Van Der Waals Interactions from Ground-State Electron Density and Free-Atom Reference Data. *Physical Review Letters* **2009**, *102* (7), 073005.
37. Monkhorst, H. J.; Pack, J. D., Special points for Brillouin-zone integrations. *Physical Review B* **1976**, *13* (12), 5188-5192.
38. Mulliken, R. S., Electronic Population Analysis on LCAO–MO Molecular Wave Functions. I. *The Journal of Chemical Physics* **1955**, *23* (10), 1833-1840.
39. Segall, M. D.; Pickard, C. J.; Shah, R.; Payne, M. C., Population analysis in plane wave

- electronic structure calculations. *Molecular Physics* **1996**, *89* (2), 571-577.
40. Segall, M. D.; Shah, R.; Pickard, C. J.; Payne, M. C., Population analysis of plane-wave electronic structure calculations of bulk materials. *Physical Review B* **1996**, *54* (23), 16317-16320.
  41. Rappe, A. K.; Casewit, C. J.; Colwell, K. S.; Goddard, W. A.; Skiff, W. M., UFF, a full periodic table force field for molecular mechanics and molecular dynamics simulations. *Journal of the American Chemical Society* **1992**, *114* (25), 10024-10035.
  42. Ewald, P. P., Die Berechnung optischer und elektrostatischer Gitterpotentiale. *Annalen der Physik* **1921**, *369* (3), 253-287.
  43. Tosi, M. P., Cohesion of Ionic Solids in the Born Model\*\*Based on work performed under the auspices of the U.S. Atomic Energy Commission. In *Solid State Physics*, Seitz, F.; Turnbull, D., Eds. Academic Press: 1964; Vol. 16, pp 1-120.
  44. Swope, W. C.; Andersen, H. C.; Berens, P. H.; Wilson, K. R., A computer simulation method for the calculation of equilibrium constants for the formation of physical clusters of molecules: Application to small water clusters. *The Journal of Chemical Physics* **1982**, *76* (1), 637-649.
  45. Berendsen, H. J. C.; Postma, J. P. M.; Gunsteren, W. F. v.; DiNola, A.; Haak, J. R., Molecular dynamics with coupling to an external bath. *The Journal of Chemical Physics* **1984**, *81* (8), 3684-3690.
  46. Chen, P.; Xu, Y.; Wang, N.; Oganov, A. R.; Duan, W., Effects of ferroelectric polarization on surface phase diagram: Evolutionary algorithm study of the BaTiO<sub>3</sub>(001) surface. *Physical Review B* **2015**, *92* (8), 085432.
  47. Li, J. C.; Zhang, R. Q.; Wang, C. L.; Wong, N. B., Effect of thickness on the electronic structure of poly(vinylidene fluoride) molecular films from first-principles calculations. *Physical Review B* **2007**, *75* (15), 155408.

## Chapter 6. Polymorphism of Chitin Separator Material

*This chapter includes the following contents:*

Kim, J.-K.<sup>†</sup>; Kim, D. H.<sup>†</sup>; Joo, S. H.<sup>†</sup>; Choi, B.; Cha, A.; Kim, K. M.; Kwon, T.-H.; Kwak, S. K.\*; Kang, S. J.\*; Jin, J.\*, Hierarchical Chitin Fibers with Aligned Nanofibrillar Architectures: A Nonwoven-Mat Separator for Lithium Metal Batteries. *ACS Nano* **2017**, *11* (6), 6114-6121. (†: **equally contributed**). Reproduced with permission from American Chemical Society, copyright 2017.<sup>1</sup>

Kim, K.<sup>†</sup>; Ha, M.<sup>†</sup>; Choi, B.<sup>†</sup>; Joo, S. H.; Kang, H. S.; Park, J. H.; Gu, B.; Park, C.; Park, C.; Kim, J.; Kwak, S. K.; Ko, H.; Jin, J.; Kang, S. J., Biodegradable, electro-active chitin nanofiber films for flexible piezoelectric transducers. *Nano Energy* **2018**, *48*, 275-283. (†: **equally contributed**). Reproduced from ref. 2 with permission from Elsevier Ltd., copyright 2018.<sup>2</sup>

---

### 6.1 Introduction

Fibers derived from natural polymers are an indispensable class of material that has versatility for a wide range of structural and functional applications.<sup>3</sup> For example, cellulose (polysaccharide) and silk (protein) have been key ingredients of fibers not only in the classic textile industry but also for state-of-the-art biomedical uses, such as sutures and tissue scaffolds.<sup>4-6</sup> Although these biogenic macromolecules naturally occur as fibers that are as serviceable, their semisynthetic versions, i.e., regenerated fibers (RFs), and the material technologies associated with the fiber spinning have led the successful commercialization and elicited scientific interests as well. Viscose rayon and lyocell fibers are good examples of regenerated cellulose fibers.<sup>7</sup> In addition, studies on RFs spun from silk fibroin have been numerous as well,<sup>8-10</sup> some of which are also in their commercialization stage.<sup>11,12</sup> As such, it is of great significance to produce advanced RFs from other natural polymers using simple fiber-spinning processes, and the RFs can offer valuable material options for many engineering applications in diverse fields.<sup>13-18</sup> Herein, we introduce a hierarchical RFs made of chitin [poly( $\beta$ -(1,4)-N-acetyl-d-glucosamine)], the second most abundant natural polysaccharide only after cellulose,<sup>19</sup> and suggest its usage as a nonwoven fiber separator for lithium (Li) metal rechargeable batteries (LMBs) through exploiting both the strong affinity to Li-ions and the inertness to the aprotic electrolytes.<sup>20</sup>

The recent LMBs based on Li-S or Li-O<sub>2</sub> system are considered one of the promising next-generation energy storage devices because of their unrivalled energy capacity (~3500 Wh/kg) in

comparison to the present Li-ion batteries (LIBs).<sup>21, 22</sup> Nevertheless, LMBs have one common yet crucial drawback that originates from using the bulk-metallic Li anode: the uncontrollable growth of Li dendrites, which significantly limits the lifecycle of LMBs and causes serious safety issues due to the internal short circuits.<sup>23-26</sup> These protruding Li dendrites arise from an inhomogeneous distribution of Li-ions at the electrolyte–electrode interface, which inevitably occurs during battery operation.<sup>27</sup>

A key idea to resolve this issue is alleviating the concentration gradient of Li-ions to mitigate the growth of Li dendrites by, as examples, introducing separators with regular nanopore arrays or creating micropatterns on the Li anode.<sup>26, 28-32</sup> Meanwhile, other technical strategies have been also intensively developed over the last two decades, such as introducing solid electrolytes, chemical additives, and barrier layers that chemically and physically restrain the dendrite growth.<sup>33-36</sup> However, these methods still present a difficulty of fabrication and mass synthesis. Thus, there is a strong demand for controlling the Li metal in a more practical way.

Here, we report on the nonwoven mat-type separator of a regenerated chitin fiber (Chiber), which is capable of effectively suppressing the growth of Li dendrites that occurs in typical LMBs and improving their Li cycling efficiency (LCE). As a probing study, we perform density functional theory (DFT) calculation and molecular dynamics (MD) simulation, which predict that chitin has a high level of physicochemical affinity to Li cations. The computation result specifically confers an excellent electrolyte-uptaking property on the Chiber separator, which works as one of the key requirements of separators for LMBs. Following the investigations on the Chiber's basic structural and functional characteristics, we finally validate the performance of Chiber separator, which is introduced in a Li–O<sub>2</sub> battery cell.

## 6.2 Computational Methods

### 6.2.1 Density Functional Theory Calculation

Density functional theory (DFT) calculations were performed using Dmol3 program.<sup>37, 38</sup> The generalized gradient approximation with Perdew–Burke–Ernzerhof (GGA-PBE) exchange–correlation functional was used,<sup>39</sup> and the core electrons were treated as all electrons with relativistic effects. The long-range van der Waals interactions were corrected using Tkatchenko–Scheffler’s method.<sup>40</sup> Spin polarization was taken into account in all calculations. The molecular orbitals were expanded by the DNP 4.4 basis set with the global orbital cutoff of 5.1 Å. The solvent environment was described using conductor-like screening model (COSMO) method with the dielectric constant of 7.2 for dimethoxyethane (DME).<sup>41</sup> The convergence criterion for self-consistent calculation was set to  $10^{-6}$  Ha, and the electron smearing of 0.005 Ha was used. The convergence criteria for geometry optimization was set to  $10^{-5}$  Ha for energy, 0.002 Ha/Å for force, and 0.005 Å for displacement, respectively. To calculate the binding energies of Li-ions, we modeled  $[\text{Li}(\text{DME})_2(\text{PP})]^+$ ,  $[\text{Li}(\text{DME})_2(\text{chitin})]^+$ , and  $[\text{Li}(\text{DME})_3]^+$  complexes, where chitin 2-mer and PP 10-mer were modeled for the calculations. The binding energy of Li-ion to surrounding molecules was calculated as follows:

$$E_{\text{binding}} = E_{[\text{Li}(\text{surr})]^+} - E_{\text{Li}^+} - E_{\text{surr}}$$

where  $E_{[\text{Li}(\text{surr})]^+}$ ,  $E_{\text{Li}^+}$ , and  $E_{\text{surr}}$  are the energy of the complexes, Li-ion, and surrounding molecules, respectively.

### 6.2.2 Molecular Dynamics Simulation

All-atom molecular dynamics (MD) simulations were performed using the Forcite program. The interactions between the nanofiber and the electrolyte solution were described by the COMPASSII force field.<sup>42</sup> The short-range van der Waals interactions were calculated within the cutoff distance of 12.5 Å, and the long-range electrostatic interactions were treated by the particle-particle particle-mesh (PPPM) summation method.<sup>43</sup> To explore the behavior of Li-ions around the nanofiber, we constructed model systems of electrolyte solution-soaked crystalline nanofiber, which consists of isotactic Polypropylene (PP),  $\alpha$ -chitin, or  $\beta$ -chitin. The crystalline nanofiber was modeled following a cylindrical shape with a diameter of  $\sim 5$  nm in a three-dimensional periodic simulation box, where the principal axis of the fiber is along the y-direction. The self-interactions were avoided by adjusting the length of the simulation

box to  $\sim 7$  nm in the  $x$ - and  $z$ -directions. The solvent molecules and the dissociated ions constituting the electrolyte solution (i.e., 1 M LiTFSI in DME) were then randomly packed into the vacuum space around the nanofiber with a density of  $1.08 \text{ g/cm}^3$ . The information on each model system is summarized in **Table 6.1**. The initial model systems were relaxed by performing geometry optimization until the convergence criteria of  $0.001 \text{ kcal/mol}$  for energy and  $0.5 \text{ kcal/mol/\AA}$  for force were satisfied. After that, the MD simulations were carried out for 10 ns at 298 K and 1 atm with the isothermal–isobaric ensemble (i.e., NPT). The temperature and the pressure of each system were controlled by Berendsen thermostat and barostat, respectively.<sup>44</sup> The Newton’s equations of motion were integrated using velocity Verlet algorithm with the time step of 1 fs.<sup>45</sup> The radial distribution function (RDF) was analyzed with MD trajectories of the last 100 ps, and the adhesion energy ( $E_{\text{ad}}$ ) between the nanofiber and the electrolyte solution was calculated throughout the MD simulation using the following equation:

$$E_{\text{ad}} = E_{\text{total}} - E_{\text{nanofiber}} - E_{\text{solution}}$$

where  $E_{\text{total}}$ ,  $E_{\text{nanofiber}}$ , and  $E_{\text{solution}}$  are the energies of the total system, nanofiber, and electrolyte solution, respectively.

**Table 6.1** The information of the model systems.  $N_{\text{chains}}$ ,  $N_{\text{DME}}$ ,  $N_{\text{Li}^+}$ , and  $N_{\text{TFSI}^-}$  are the number of chains constituting the nanofiber, DME molecules, Li ions, and TFSI ions contained in each model system, respectively.

System	Box size $X \times Y \times Z$ (nm)	$N_{\text{chains}}$	$N_{\text{DME}}$	$N_{\text{Li}^+}$	$N_{\text{TFSI}^-}$
PP	$7.0 \times 4.0 \times 7.1$	44	736	76	76
$\alpha$ -chitin	$7.0 \times 4.2 \times 7.0$	37	772	80	80
$\beta$ -chitin	$7.0 \times 4.2 \times 7.0$	37	779	81	81

## 6.3 Results and Discussion

### 6.3.1 Polymorphism of Chitin

The biphasic structure of the regenerated chitin fiber (Chiber) was confirmed by experimental analysis of the crystal structure. In nature, the chitin occurs as supramolecular semicrystalline and exists in two major distinct polymorphs:  $\alpha$ -chitin (orthorhombic) and  $\beta$ -chitin (monoclinic). These chitin crystals have different molecular conformations with dissimilar hydrogen-bond densities. The  $\alpha$ -chitin is characterized by chitin molecules being arranged in the antiparallel manner whereby the intramolecular C=O $\cdots$ HO hydrogen bonds are simultaneously engaged with the intersheet C=O $\cdots$ HN hydrogen bonds (**Figure 6.1a,b**). Meanwhile, in  $\beta$ -chitin, chitin molecules are stacked in the parallel arrangement and have intramolecular C=O $\cdots$ HO hydrogen bonds (**Figure 6.1c**).

Density functional theory calculations on the two polymorphs revealed that their structural differences lead to different polarization characteristics.<sup>2</sup> Owing to the polar functional groups (i.e., amide, hydroxyl, and ether) and the  $2_1$  helical conformation, a chitin molecule exhibits strong uniaxial polarization along the chain backbone. Therefore, the antiparallel arrangement of chitin molecules in the  $\alpha$ -chitin leads to the cancellation of electric dipole moments, resulting in almost zero polarization. In contrast, the parallel arrangement of chitin molecules in the  $\beta$ -chitin leads to the strong uniaxial net-polarization along the [001] direction, conferring excellent piezoelectricity (**Figure 6.2**).



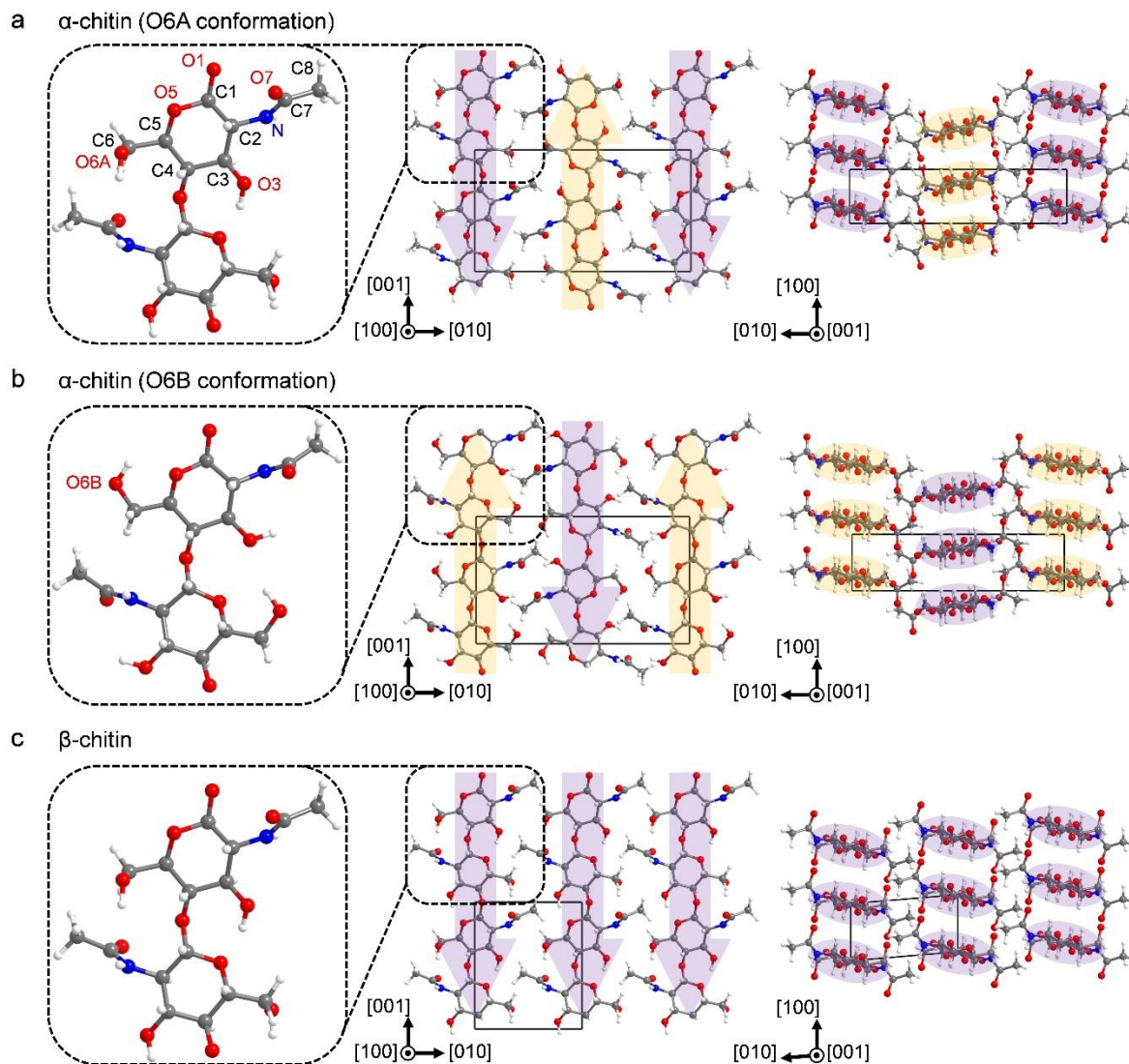


**Figure 6.1** Projection views along the  $[100]$  and  $[001]$  directions of the optimized crystal structures of (a)  $\alpha$ -chitin with O6A conformation, (b)  $\alpha$ -chitin with O6B conformation, and (c)  $\beta$ -chitin. Magnified images show the molecular structure of  $\beta$ -(1,4)-N-acetyl-D-glucosamine in each crystal structure. Orange and purple arrows indicate the polarization direction of each chitin molecule along  $[001]$  and  $[00\bar{1}]$ , respectively. The C, H, N, and O atoms are colored gray, white, blue, and red, respectively. Reproduced from ref. 2 with permission from Elsevier Ltd., copyright 2018.

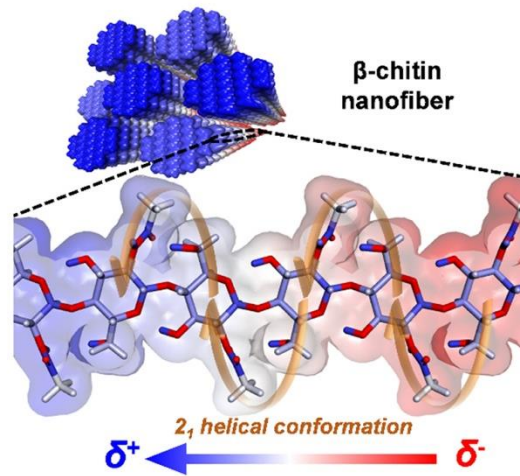


**Figure 6.2** Spontaneous polarization of  $\beta$ -chitin nanofibers. The arrow pointing from red to blue represents the polarization direction. The positively and negatively charged atoms are blue and red, respectively. Reproduced from ref. 2 with permission from Elsevier Ltd., copyright 2018.

### 6.3.2 Chitin-Electrolyte Interaction

To check the usage of chitin as a nonwoven fiber separator for Li metal batteries, we explored the behavior of Li-ions around the chitin fiber and the chitin–electrolyte interactions by performing MD simulations and DFT calculations. **Figure 6.3** shows the MD snapshots of polypropylene (PP) (Celgard, a conventional separator material),  $\alpha$ -chitin, and  $\beta$ -chitin nanofibers immersed in the electrolyte solution at 0 and 10 ns. While the PP nanofiber does not hold Li-ions at its surface, the chitin nanofiber of both polymorphs exhibits a high affinity to Li-ions at the surface-exposed hydroxyl and acetylamino groups (**Figure 6.4**). Statistically, it is also seen from the radial distribution function (RDF) between the nanofibers and Li-ions (**Figure 6.5**), where the chitin nanofibers of both polymorphs show higher intensities than the PP nanofiber and notably exhibit sharp peaks at  $r = \sim 2$  Å. We find that the peaks represent the Li-ions coordinated to hydroxyl and amide functional groups of chitin molecule forming a pocket-like structure (the inset of **Figure 6.5**). Thus, the functional groups of chitin molecule significantly contribute to the high Li-ion affinity. Furthermore, we estimate the binding energy of Li-ions in  $[\text{Li}(\text{DME})_2(\text{PP})]^+$ ,  $[\text{Li}(\text{DME})_2(\text{chitin})]^+$ , and  $[\text{Li}(\text{DME})_3]^+$  complexes. The binding strength of Li-ions with chitin (i.e.,  $E_{\text{binding}} = -3.49$  eV) is found to be larger than that with PP (i.e.,  $E_{\text{binding}} = -1.91$  eV) but similar to that with DME molecules (i.e.,  $E_{\text{binding}} = -3.46$  eV) (**Figure 6.6**). This binding characteristic implies that Li-ions can be bound to chitin nanofiber reversibly. Consequently, the functional groups of chitin molecule play a significant role in the high Li-ion affinity with reversible binding, and thus a low charge transfer resistance of chitin separator is expected. Separately, we notify that the adhesion energy of the  $\alpha$ -chitin or  $\beta$ -chitin nanofiber to the electrolyte solution is estimated to be approximately 3 times larger than that of the PP nanofiber from our MD simulation (**Figure 6.7**). This strong adhesion energy of chitin nanofiber is a telltale signature for the high uptake of electrolyte solution of Chiber separator.

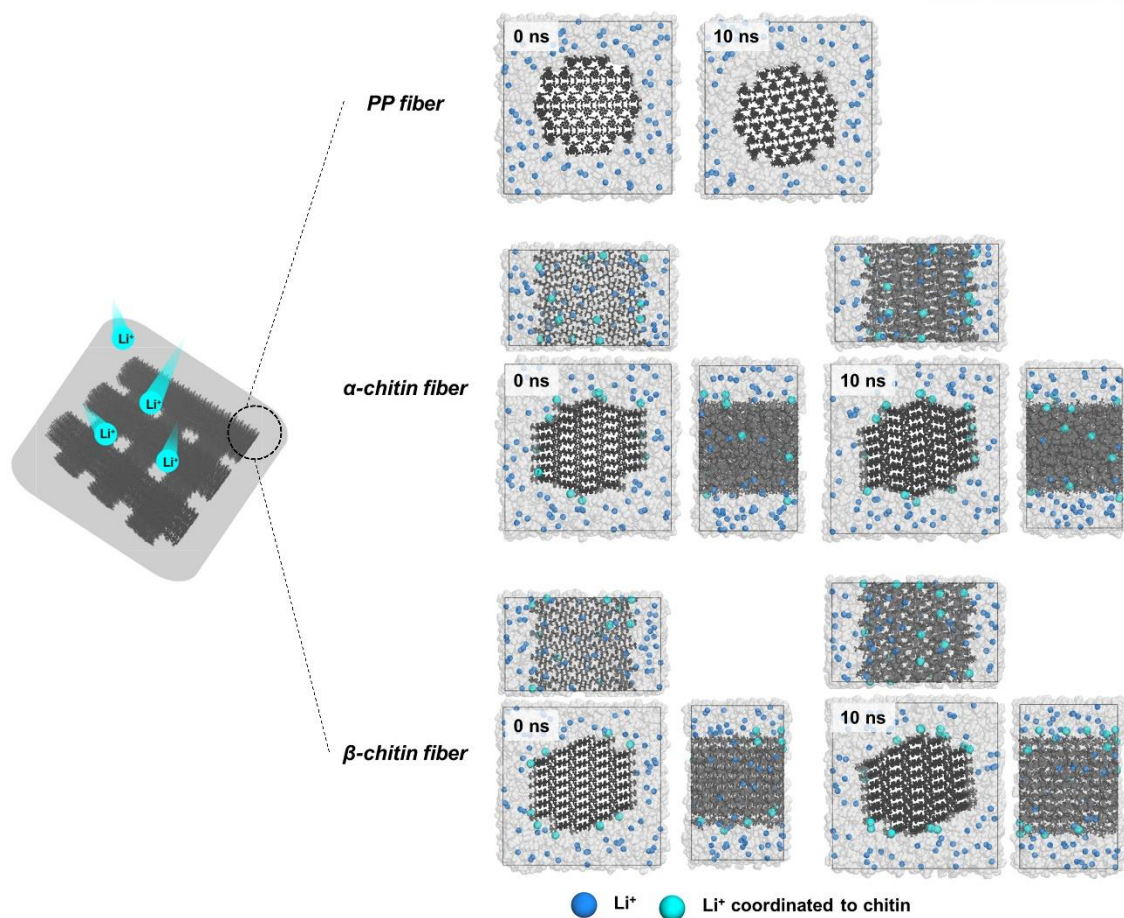


**Figure 6.3** MD snapshots showing the degree of physicochemical affinity to Li cation with PP(Celgard), α-chitin, and β-chitin. Reproduced from ref. 1 with permission from American Chemical Society, copyright 2017.

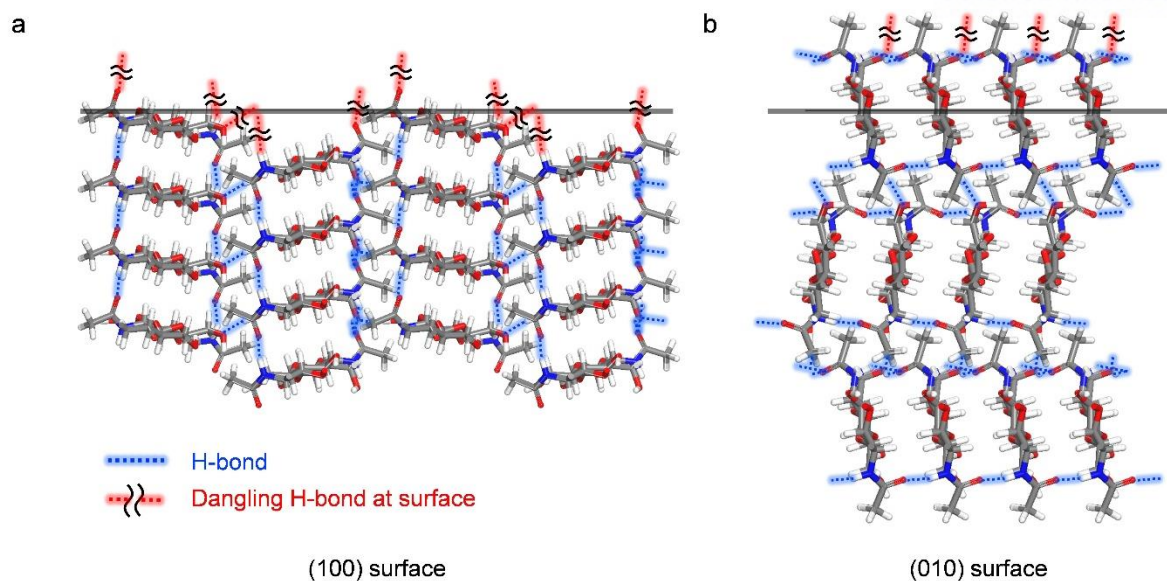


**Figure 6.4** The atomic configuration of (a) (100) and (b) (010) planes of  $\alpha$ -chitin fibers. The blue dotted lines represent the hydrogen bonds inside the alpha chitin fibers and the red dotted lines represent the dangling hydrogen bonds of the polar amid and hydroxyl groups exposed on the chitin fiber surface. Carbon, hydrogen, nitrogen, and oxygen are gray, white, blue, and red colors, respectively. Reproduced from ref. 1 with permission from American Chemical Society, copyright 2017.

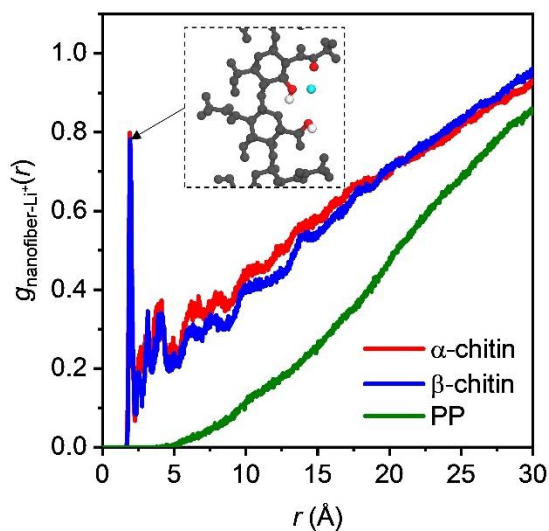


**Figure 6.5** The RDFs of  $\alpha$ -chitin,  $\beta$ -chitin, and PP with Li-ions. Reproduced from ref. 1 with permission from American Chemical Society, copyright 2017.



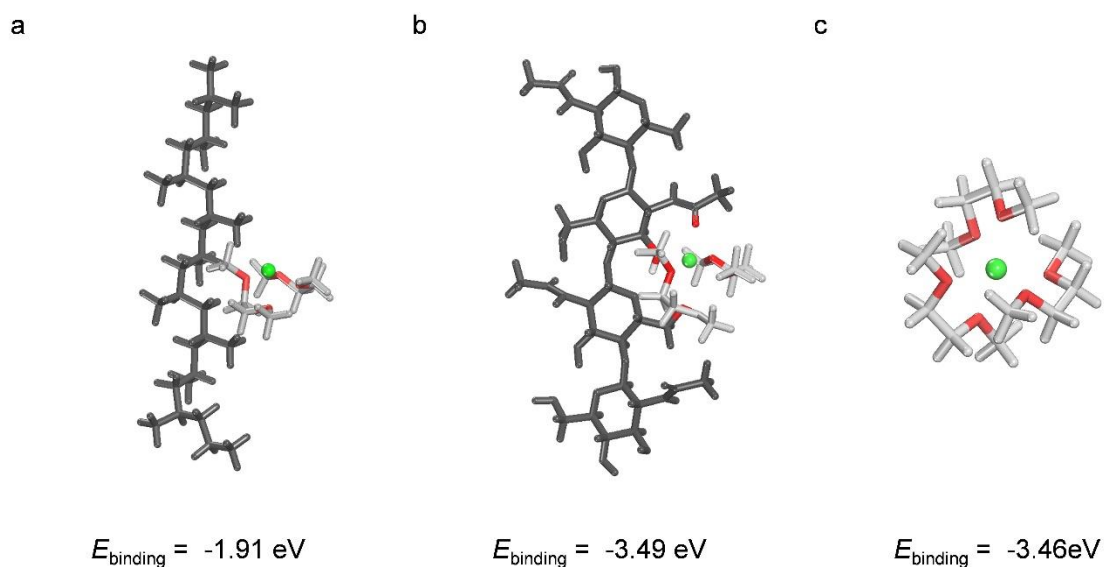


**Figure 6.6** The optimized geometries of (a)  $[\text{Li}(\text{DME})_2(\text{PP})]^+$ , (b)  $[\text{Li}(\text{DME})_2(\text{chitin})]^+$ , and (c)  $[\text{Li}(\text{DME})_3]^+$  complexes with the calculated binding energies of  $\text{Li}^+$  to surrounding molecules. The polymer, DME molecule, and oxygen atom are dark gray, light gray and red colors, respectively. Reproduced from ref. 1 with permission from American Chemical Society, copyright 2017.

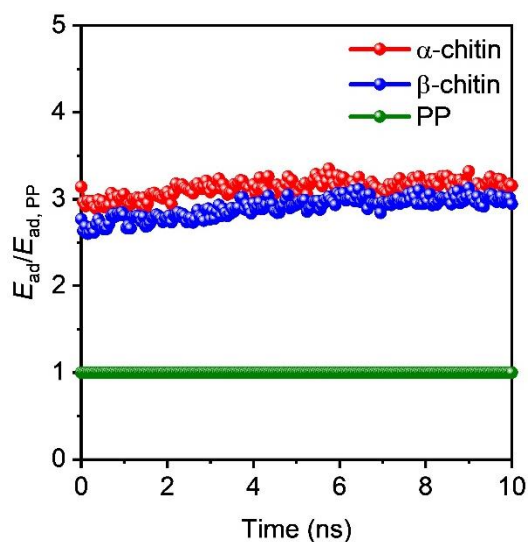


**Figure 6.7** The normalized adhesion energy of  $\alpha$ -chitin and  $\beta$ -chitin to PP in the electrolyte solution. Reproduced from ref. 1 with permission from American Chemical Society, copyright 2017.

## 6.4 Conclusion

In conclusion, we have successfully demonstrated a hierarchical regenerated chitin fiber (Chiber), working as a nonwoven mat-type Chiber separator that is capable of effectively mitigating Li dendrites in LMBs. Based on computational support and electrolyte uptake measurement, we found that the Chitin molecule has a stronger Li-ion affinity than conventional battery separators due to unique coordinations with functional groups. In particular, this Li-ion affinity arose from Chiber separators with the binding reversibility allowed to exhibit greatly improved Columbic efficiency with Li metal mitigation not only in the Li/Li symmetry cell but also in the realistic LMBs such as Li-O<sub>2</sub> and Na-O<sub>2</sub> batteries.



## 6.5 References

1. Kim, J.-K.; Kim, D. H.; Joo, S. H.; Choi, B.; Cha, A.; Kim, K. M.; Kwon, T.-H.; Kwak, S. K.; Kang, S. J.; Jin, J., Hierarchical Chitin Fibers with Aligned Nanofibrillar Architectures: A Nonwoven-Mat Separator for Lithium Metal Batteries. *ACS Nano* **2017**, *11* (6), 6114-6121.
2. Kim, K.; Ha, M.; Choi, B.; Joo, S. H.; Kang, H. S.; Park, J. H.; Gu, B.; Park, C.; Park, C.; Kim, J.; Kwak, S. K.; Ko, H.; Jin, J.; Kang, S. J., Biodegradable, electro-active chitin nanofiber films for flexible piezoelectric transducers. *Nano Energy* **2018**, *48*, 275-283.
3. Yonenaga, A., Future man-made fiber. In *High-performance and specialty fibers*, Springer: 2016; pp 435-451.
4. Thilagavathi, G.; Viju, S., 11 - Silk as a suture material. In *Advances in Silk Science and Technology*, Basu, A., Ed. Woodhead Publishing: 2015; pp 219-232.
5. NARAT, J. K.; CIPOLLA, A. F.; CANGELOSI, J. P., FORTISAN® (REGENERATED CELLULOSE YARN), A NEW SUTURE MATERIAL. *Archives of Surgery* **1950**, *60* (6), 1218-1230.
6. Mandal, B. B.; Grinberg, A.; Seok Gil, E.; Panilaitis, B.; Kaplan, D. L., High-strength silk protein scaffolds for bone repair. *Proceedings of the National Academy of Sciences* **2012**, *109* (20), 7699-7704.
7. Qi, H., Novel Regenerated Cellulosic Materials. In *Novel Functional Materials Based on Cellulose*, Springer: 2017; pp 25-43.
8. Cheng, J.; Park, D.; Jun, Y.; Lee, J.; Hyun, J.; Lee, S.-H., Biomimetic spinning of silk fibers and in situ cell encapsulation. *Lab on a Chip* **2016**, *16* (14), 2654-2661.
9. Fang, G.; Huang, Y.; Tang, Y.; Qi, Z.; Yao, J.; Shao, Z.; Chen, X., Insights into Silk Formation Process: Correlation of Mechanical Properties and Structural Evolution during Artificial Spinning of Silk Fibers. *ACS Biomaterials Science & Engineering* **2016**, *2* (11), 1992-2000.
10. Yan, J.; Zhou, G.; Knight, D. P.; Shao, Z.; Chen, X., Wet-Spinning of Regenerated Silk Fiber from Aqueous Silk Fibroin Solution: Discussion of Spinning Parameters. *Biomacromolecules* **2010**, *11* (1), 1-5.
11. Bourzac, K., Spiders: Web of intrigue. *Nature* **2015**, *519* (7544), S4-S6.
12. Eisenstein, M., Living factories of the future. *Nature* **2016**, *531* (7594), 401-403.
13. Huang, Y.; Zhong, Z.; Duan, B.; Zhang, L.; Yang, Z.; Wang, Y.; Ye, Q., Novel fibers fabricated directly from chitin solution and their application as wound dressing. *Journal of*

- Materials Chemistry B* **2014**, 2 (22), 3427-3432.
14. Cai, J.; Zhang, L.; Zhou, J.; Li, H.; Chen, H.; Jin, H., Novel Fibers Prepared from Cellulose in NaOH/Urea Aqueous Solution. *Macromolecular Rapid Communications* **2004**, 25 (17), 1558-1562.
  15. Guerette, P. A.; Hoon, S.; Seow, Y.; Raida, M.; Masic, A.; Wong, F. T.; Ho, V. H. B.; Kong, K. W.; Demirel, M. C.; Pena-Francesch, A.; Amini, S.; Tay, G. Z.; Ding, D.; Miserez, A., Accelerating the design of biomimetic materials by integrating RNA-seq with proteomics and materials science. *Nature Biotechnology* **2013**, 31 (10), 908-915.
  16. Ma, B.; Qiao, X.; Hou, X.; Yang, Y., Pure keratin membrane and fibers from chicken feather. *International Journal of Biological Macromolecules* **2016**, 89, 614-621.
  17. Mirabedini, A.; Foroughi, J.; Thompson, B.; Wallace, G. G., Fabrication of Coaxial Wet-Spun Graphene–Chitosan Biofibers. *Advanced Engineering Materials* **2016**, 18 (2), 284-293.
  18. Qiu, W.; Teng, W.; Cappello, J.; Wu, X., Wet-Spinning of Recombinant Silk-Elastin-Like Protein Polymer Fibers with High Tensile Strength and High Deformability. *Biomacromolecules* **2009**, 10 (3), 602-608.
  19. Salaberria, A. M.; Labidi, J.; Fernandes, S. C. M., Different routes to turn chitin into stunning nano-objects. *European Polymer Journal* **2015**, 68, 503-515.
  20. Jung, J.-W.; Im, H.-G.; Lee, D.; Yu, S.; Jang, J.-H.; Yoon, K. R.; Kim, Y. H.; Goodenough, J. B.; Jin, J.; Kim, I.-D.; Bae, B.-S., Conducting Nanopaper: A Carbon-Free Cathode Platform for Li–O<sub>2</sub> Batteries. *ACS Energy Letters* **2017**, 2 (3), 673-680.
  21. Bruce, P. G.; Freunberger, S. A.; Hardwick, L. J.; Tarascon, J.-M., Li–O<sub>2</sub> and Li–S batteries with high energy storage. *Nature Materials* **2012**, 11 (1), 19-29.
  22. Cheng, F.; Chen, J., Metal–air batteries: from oxygen reduction electrochemistry to cathode catalysts. *Chemical Society Reviews* **2012**, 41 (6), 2172-2192.
  23. Bai, P.; Li, J.; Brushett, F. R.; Bazant, M. Z., Transition of lithium growth mechanisms in liquid electrolytes. *Energy & Environmental Science* **2016**, 9 (10), 3221-3229.
  24. Lu, Y.; Tu, Z.; Archer, L. A., Stable lithium electrodeposition in liquid and nanoporous solid electrolytes. *Nature Materials* **2014**, 13 (10), 961-969.
  25. Yamaki, J.-i.; Tobishima, S.-i.; Hayashi, K.; Keiichi, S.; Nemoto, Y.; Arakawa, M., A consideration of the morphology of electrochemically deposited lithium in an organic electrolyte. *Journal of Power Sources* **1998**, 74 (2), 219-227.
  26. Zheng, G.; Lee, S. W.; Liang, Z.; Lee, H.-W.; Yan, K.; Yao, H.; Wang, H.; Li, W.; Chu, S.; Cui, Y., Interconnected hollow carbon nanospheres for stable lithium metal anodes. *Nature Nanotechnology* **2014**, 9 (8), 618-623.

27. Xu, W.; Wang, J.; Ding, F.; Chen, X.; Nasybulin, E.; Zhang, Y.; Zhang, J.-G., Lithium metal anodes for rechargeable batteries. *Energy & Environmental Science* **2014**, 7 (2), 513-537.
28. Kang, S. J.; Mori, T.; Suk, J.; Kim, D. W.; Kang, Y.; Wilcke, W.; Kim, H.-C., Improved cycle efficiency of lithium metal electrodes in Li-O<sub>2</sub> batteries by a two-dimensionally ordered nanoporous separator. *Journal of Materials Chemistry A* **2014**, 2 (26), 9970-9974.
29. Tu, Z.; Kambe, Y.; Lu, Y.; Archer, L. A., Nanoporous Polymer-Ceramic Composite Electrolytes for Lithium Metal Batteries. *Advanced Energy Materials* **2014**, 4 (2), 1300654.
30. Liu, W.; Lin, D.; Pei, A.; Cui, Y., Stabilizing Lithium Metal Anodes by Uniform Li-Ion Flux Distribution in Nanochannel Confinement. *Journal of the American Chemical Society* **2016**, 138 (47), 15443-15450.
31. Park, J.; Jeong, J.; Lee, Y.; Oh, M.; Ryou, M.-H.; Lee, Y. M., Micro-Patterned Lithium Metal Anodes with Suppressed Dendrite Formation for Post Lithium-Ion Batteries. *Advanced Materials Interfaces* **2016**, 3 (11), 1600140.
32. Tu, Z.; Zachman, M. J.; Choudhury, S.; Wei, S.; Ma, L.; Yang, Y.; Kourkoutis, L. F.; Archer, L. A., Nanoporous Hybrid Electrolytes for High-Energy Batteries Based on Reactive Metal Anodes. *Advanced Energy Materials* **2017**, 7 (8), 1602367.
33. Murata, K.; Izuchi, S.; Yoshihisa, Y., An overview of the research and development of solid polymer electrolyte batteries. *Electrochimica Acta* **2000**, 45 (8), 1501-1508.
34. Ding, F.; Xu, W.; Graff, G. L.; Zhang, J.; Sushko, M. L.; Chen, X.; Shao, Y.; Engelhard, M. H.; Nie, Z.; Xiao, J.; Liu, X.; Sushko, P. V.; Liu, J.; Zhang, J.-G., Dendrite-Free Lithium Deposition via Self-Healing Electrostatic Shield Mechanism. *Journal of the American Chemical Society* **2013**, 135 (11), 4450-4456.
35. Khurana, R.; Schaefer, J. L.; Archer, L. A.; Coates, G. W., Suppression of Lithium Dendrite Growth Using Cross-Linked Polyethylene/Poly(ethylene oxide) Electrolytes: A New Approach for Practical Lithium-Metal Polymer Batteries. *Journal of the American Chemical Society* **2014**, 136 (20), 7395-7402.
36. Tikekar, M. D.; Choudhury, S.; Tu, Z.; Archer, L. A., Design principles for electrolytes and interfaces for stable lithium-metal batteries. *Nature Energy* **2016**, 1 (9), 16114.
37. Delley, B., An all-electron numerical method for solving the local density functional for polyatomic molecules. *The Journal of Chemical Physics* **1990**, 92 (1), 508-517.
38. Delley, B., From molecules to solids with the DMol3 approach. *The Journal of Chemical Physics* **2000**, 113 (18), 7756-7764.
39. Perdew, J. P.; Burke, K.; Ernzerhof, M., Generalized Gradient Approximation Made Simple. *Physical Review Letters* **1996**, 77 (18), 3865-3868.

40. Tkatchenko, A.; Scheffler, M., Accurate Molecular Van Der Waals Interactions from Ground-State Electron Density and Free-Atom Reference Data. *Physical Review Letters* **2009**, *102* (7), 073005.
41. Klamt, A.; Schüürmann, G., COSMO: a new approach to dielectric screening in solvents with explicit expressions for the screening energy and its gradient. *Journal of the Chemical Society, Perkin Transactions 2* **1993**, (5), 799-805.
42. Sun, H.; Jin, Z.; Yang, C.; Akkermans, R. L. C.; Robertson, S. H.; Spenley, N. A.; Miller, S.; Todd, S. M., COMPASS II: extended coverage for polymer and drug-like molecule databases. *Journal of Molecular Modeling* **2016**, *22* (2), 47.
43. Hockney, R. W.; Eastwood, J. W., *Computer simulation using particles*. crc Press: 1988.
44. Berendsen, H. J. C.; Postma, J. P. M.; Gunsteren, W. F. v.; DiNola, A.; Haak, J. R., Molecular dynamics with coupling to an external bath. *The Journal of Chemical Physics* **1984**, *81* (8), 3684-3690.
45. Swope, W. C.; Andersen, H. C.; Berens, P. H.; Wilson, K. R., A computer simulation method for the calculation of equilibrium constants for the formation of physical clusters of molecules: Application to small water clusters. *The Journal of Chemical Physics* **1982**, *76* (1), 637-649.

## Chapter 7. Summary and Future Perspectives

### 7.1 Summary

In this dissertation, theoretical studies on battery materials were presented. Using the multiscale simulations, the polymorphism and charge storage mechanism of three newly designed electrode materials, a conventional binder material, and a separator material were studied.

In Chapter 1, a brief overview and the challenges of rechargeable batteries were discussed. We then provided a general background of the charge storage mechanism and polymorphism. Finally, we explained the importance of multiscale computational techniques including the density functional theory calculation, density functional tight binding calculation, molecular dynamics simulation, and Monte Carlo simulation.

In Chapter 2, we theoretically studied the polymorphism and charge storage mechanism of c-HBC, as a new type of anode material for Li-ion batteries. The in-silico polymorph screening with the Monte Carlo simulation revealed that the crystal structure of polymorph II' was the metastable  $R\bar{3}$  crystal phase, which was characterized by the c-HBC molecules being arranged in the ABC packing sequence with consistent molecular orientation. The result indicated that c-HBC exhibited packing polymorphism with forms of  $P2_1/c$  and  $R\bar{3}$  crystal phases. On the other hand, the polymorph II was determined to be the  $P3_1$  (or  $P3_2$ ) crystal phase with Pd atoms, which was not a polymorph of c-HBC. Moreover, theoretical investigation on the lithium storage mechanism of c-HBC revealed that the c-HBC anode exhibited a single-stage Li-ion insertion behavior without voltage penalty due to the 3D-ordered empty pores, which originated from the contorted structure of c-HBC.

In Chapter 3, we theoretically examined the polymorphism and charge storage mechanism of F-cHBC as a potential electrochemical organic electrode material. The computational polymorph screening revealed that the crystal structure of polymorph I was the energetically stable  $P2_1/c$  crystal phase. Moreover, our investigation on lithium/sodium storage mechanism showed that Li- and Na-ions could be stored in two distinct sites surrounded by electronegative fluorine atoms and a negatively charged bent edge aromatic ring.

In Chapter 4, we theoretically investigated the polymorphism and charge storage mechanism of the rCTF, as a promising organic anode material for Li-ion batteries. The potential energy analysis clearly showed that rCTF can exhibit packing polymorphism for two energy-minimum packing modes: AB and slipped-parallel packing modes. The most stable was the slipped-packing mode. Based on the

density functional theory calculations and Monte Carlo simulations, it was also revealed that rCTF provided a theoretical capacity of up to 1200 mAh g<sup>-1</sup> using quinone, triazine, and benzene rings as the redox-active sites. Moreover, it was found that the structural deformation of rCTF during activation allowed more redox-active sites to be accessible, especially benzene rings.

In Chapter 5, we theoretically examined the effects of the crystal phases, particularly the  $\alpha$ - and  $\beta$ -phases, of the polymorphic PVDF binder material on the battery performance. Based on the density functional theory calculations and molecular dynamics simulation, it was revealed that the strong polarization generated by the ferroelectric  $\beta$ -PVDF can effectively transport electrons and Li-ions, leading to a reduction in the charge transfer resistance and alleviation of the concentration polarization in the Li-ion battery system.

In Chapter 6, we present a theoretical study on polymorphism of chitin separator material and its interaction with electrolyte. As a semicrystalline biopolymer, chitin can exist in two polymorphs,  $\alpha$ - and  $\beta$ -phase. These crystals have different molecular conformation and arrangement, resulting in different polarization characteristics. Based on density functional theory calculations and molecular dynamics simulations, it was found that both polymorphs of chitin had excellent electrolyte-uptaking property and high physicochemical affinity to Li-ions with binding reversibility.

In conclusion, we investigated the polymorphism and charge storage mechanism of various solid-state battery materials such as polymer, molecular crystal, and two-dimensional covalent organic framework for their application in rechargeable batteries using multiscale computational techniques. We anticipate that our theoretical studies will contribute to a better understanding of polymorphic behavior and charge storage mechanism of battery materials and provide new strategies for the design and discovery of novel battery materials.

## 7.2 Future Perspectives

Herein, we will discuss issues and challenges related to the topics covered in this dissertation and propose future research directions to design and discover novel materials for applications in high-performance rechargeable batteries.

The major challenge in the research field of polymorphism is predicting the polymorphs of a compound. Based on the structure of a molecule or compound, determining whether the compound is polymorphic is difficult. Moreover, it is a formidable task to experimentally construct a polymorphic landscape under varying conditions. In this context, a computer-aided prediction of polymorphs and phase diagrams can accelerate the discovery of new stable and metastable crystalline materials without empirical knowledge. Furthermore, a systematic understanding of the structure-property relationship based on established polymorph databases will provide the insights into the design of new materials with superior properties.

Despite tremendous efforts in crystal structure prediction, predicting which polymorph will emerge still remains a major issue.<sup>1,2</sup> Hence, a fundamental understanding of crystal nucleation and growth can help this problem. Therefore, it is important to study not only the thermodynamic stability, but also the kinetic stability associated with the nucleation and growth of different polymorphs. In this regard, some progress has been made in the estimation of growth rates by calculating attachment energy and surface rugosity.<sup>3,4</sup> The provision of kinetic and thermodynamic properties can be a useful experimental guide in realizing polymorphs with intriguing physicochemical properties.

From a materialistic point of view, organic materials and electrically conductive metal organic frameworks have great potential as electrode materials for next-generation rechargeable batteries.<sup>5-9</sup> Compared to the conventional battery materials, they provide more diversity in material design. Specifically, given that molecules with similar chemical structures show disparate polymorphic behavior with different number of polymorphs, their flexible structure modifications enable fine tuning of properties and significantly expand the scope of energy storage materials. In addition, their redox chemistry such as the overlithiation process has not been fully understood. In this context, it is expected that the machine learning technique and multiscale simulation will help in the in-depth understanding of the structure-property relationships and design principles. As simple model structures, the functionalized c-HBC and MX<sub>4</sub>-type metal organic framework will be studied first in our future works. Our ultimate goal is to computationally design novel battery materials.



### 7.3 References

1. Cruz-Cabeza, A. J.; Feeder, N.; Davey, R. J., Open questions in organic crystal polymorphism. *Communications Chemistry* **2020**, *3* (1), 142.
2. Aykol, M.; Dwaraknath, S. S.; Sun, W.; Persson, K. A., Thermodynamic limit for synthesis of metastable inorganic materials. *Science Advances* **2018**, *4* (4), eaaq0148.
3. Cruz-Cabeza, A. J.; Davey, R. J.; Sachithanathan, S. S.; Smith, R.; Tang, S. K.; Vetter, T.; Xiao, Y., Aromatic stacking – a key step in nucleation. *Chemical Communications* **2017**, *53* (56), 7905-7908.
4. Montis, R.; Davey, R. J.; Wright, S. E.; Woollam, G. R.; Cruz-Cabeza, A. J., Transforming Computed Energy Landscapes into Experimental Realities: The Role of Structural Rugosity. *Angewandte Chemie International Edition* **2020**, *59* (46), 20357-20360.
5. Schon, T. B.; McAllister, B. T.; Li, P.-F.; Seferos, D. S., The rise of organic electrode materials for energy storage. *Chemical Society Reviews* **2016**, *45* (22), 6345-6404.
6. Poizot, P.; Gaubicher, J.; Renault, S.; Dubois, L.; Liang, Y.; Yao, Y., Opportunities and Challenges for Organic Electrodes in Electrochemical Energy Storage. *Chemical Reviews* **2020**, *120* (14), 6490-6557.
7. Feng, D.; Lei, T.; Lukatskaya, M. R.; Park, J.; Huang, Z.; Lee, M.; Shaw, L.; Chen, S.; Yakovenko, A. A.; Kulkarni, A.; Xiao, J.; Fredrickson, K.; Tok, J. B.; Zou, X.; Cui, Y.; Bao, Z., Robust and conductive two-dimensional metal–organic frameworks with exceptionally high volumetric and areal capacitance. *Nature Energy* **2018**, *3* (1), 30-36.
8. Sheberla, D.; Bachman, J. C.; Elias, J. S.; Sun, C.-J.; Shao-Horn, Y.; Dincă, M., Conductive MOF electrodes for stable supercapacitors with high areal capacitance. *Nature Materials* **2017**, *16* (2), 220-224.
9. Xie, L. S.; Skorupskii, G.; Dincă, M., Electrically Conductive Metal–Organic Frameworks. *Chemical Reviews* **2020**, *120* (16), 8536-8580.

## Acknowledgements

It seems like yesterday that I entered UNIST with passion, excitement, and an expectation to achieve my dream, but it has already been almost 10 years and I have finally graduated. It was never easy for me to enter college, study my major, eventually go to graduate school, do my research, and complete my Ph.D. course. With the help of many invaluable relationships and different people, I was able to successfully reach my destination.

First, I would like to express my deepest gratitude to my advisor, Professor Sang Kyu Kwak, for his unwavering support in my academic instruction and research. He was an inspiration to me in that he always worked hard on everything, including research and classes. He paid keen attention to all the students, and the valuable advice he has given me was the driving force behind my growth. Through his guidance, I will study hard and become a great researcher.

Next, I would like to express my sincerest gratitude to the professors who served in the thesis committee for my doctoral thesis. I would like to thank Professors Hyun-Kon Song, Seok Ju Kang, and Soojin Park for providing their guidance and instruction in various joint research works during my Ph. D. course. I would also like to thank Professor Dong-Hwa Seo for his sharp comments and good advice in my doctoral dissertation. Through the professors' guidance and comments, I was able to address my shortcomings and determine future directions.

In addition, I would like to thank my seniors, juniors, and colleagues in the lab who have been working on the study as researchers like myself. I sincerely thank my invaluable colleagues, Su Hwan Kim, Ju Hyun Park, and Eun Min Go, who have helped me in the lab since I was an undergraduate. I would also like to thank the other lab members, Dr. Tae Kyung Lee, Dr. Gwan Yeong Jung, Dr. Dae Yeon Hwang, Dr. Sung O Park, Dr. Woo Cheol Jeon, Dr. Eunhye Shin, Jeong Hyeon Lee, Jin Chul Kim, Kristano Imanuel, Kyung Min Lee, Jiyun Lee, Hyeong Yong Lim, Seonwoo Shin, Yu Jin Kim, Ji Eun Lee, Hyeongjun Kim, Seung Hak Oh, Seong Hyeon Kweon, Seung Min Lee, David Paredes, and Dr. Yuan Jun Gao. With their help, I was successfully able to obtain my Ph. D.

Lastly, I would like to thank my family for always trusting and supporting me. Thanks to their understanding of my doctorate program and constant love despite my adamancy, I was able to complete it by focusing on the research without any distractions. I will do my best to become a son who can repay the love and care given by my family.

In addition, I would like to thank all the collaborators for helping me achieve numerous research outcomes. I will do my best to become a researcher to acknowledge everyone who have encouraged me in my journey. Thank you.

## 감사의 글

꿈을 이루기 위해 열정, 설렘, 기대감을 가득 안고 UNIST에 입학한지가 엊그제 같은데, 어느덧 10년 가까운 시간이 지났습니다. 대학에 들어와서 전공을 공부하고 연구를 경험하며, 결국에 대학원에 진학하여 이렇게 박사 학위를 끝마치기까지의 일련의 과정들은 결코 쉽지 않았습니다. 그 과정에서 만난 수많은 소중한 인연과 고마운 분들의 도움 덕분에, 제가 성공적으로 현재의 목적지까지 도달할 수 있었던 것 같습니다.

먼저, 많은 학문적 가르침을 주시고 연구의 기회를 아낌없이 지원해주신 지도 교수님 곽상규 교수님께 깊은 감사의 마음을 전합니다. 연구, 수업 등 모든 일에 항상 열정을 다해 임하시는 모습은 저에게 큰 귀감이 되었습니다. 언제나 학생들에게 큰 관심을 가지시며 때로는 지도 교수님으로서 때로는 인생 선배님으로서 말씀해 주셨던 귀중한 조언들은 제가 더 크게 성장할 수 있는 원동력이 되었습니다. 교수님의 가르침을 바탕으로 앞으로 열심히 배우고 노력해서 부족함이 없는 연구자로 성장할 수 있도록 하겠습니다.

다음으로, 바쁘신 가운데에도 제 박사 학위 논문의 심사 위원을 맡아 주신 교수님들께 진심으로 감사의 말씀을 드립니다. 지난 학위 과정 동안 여러 공동 연구를 지도해 주시며 많은 가르침을 주신 송현곤 교수님, 강석주 교수님, 박수진 교수님께 감사드립니다. 그리고 비록 공동 연구의 기회는 없었지만, 심사에서 날카로운 코멘트와 좋은 조언을 해 주신 서동화 교수님께 감사드립니다. 교수님들의 지도를 통해, 저의 부족한 점과 앞으로 나아갈 방향에 대해 깊이 고민해 볼 수 있는 기회를 가질 수 있었습니다.

아울러, 저와 같은 연구자의 길을 걸으며 연구에 매진해온 연구실 선배, 후배, 동기들에게 감사의 말씀 전합니다. 학부생 때부터 연구실 생활을 같이 해온 저의 소중한 동기들, 수환이, 주현이, 그리고 은민이에게 진심으로 고맙습니다. 그 동안 저와 직간접적으로 연구를 같이 해왔던, 태경이형, 관영이형, 대연이형, 성오형, 우철이형, 은혜누나, 정현이, 진철이, Kris, 경민이, 지윤이형, 형용이형, 선우, 유진이, 지은이, 형준이, 승학이, 성현이, 승민이, David 그리고 Yuan-Jun Gao 박사님에게 모두 고맙다는 말을 전합니다. 긴 학위 기간 동안 힘이 되어 주고 도와준 덕분에 좋은 연구 성과를 이룰 수 있었습니다.

마지막으로 항상 저를 믿고 응원해 주신 아빠, 엄마, 그리고 누나에게 감사드립니다. 제 고집으로 시작한 박사 과정을 이해해 주시고 한결같이 사랑으로 보살펴 주셔서, 아무런 걱정 없이 연구에만 몰두하며 박사 학위를 잘 마칠 수 있었습니다. 앞으로 열심히 노력해서 가족들의 사랑과 보살핌에 보답할 수 있는 자랑스러운 아들이 되도록 하겠습니다.

이외에도 많은 연구 성과를 이룰 수 있도록 도움을 주신 여러 공동 연구자들과 교수님들께 감사드립니다. 옆에서 격려해주신 모든 분들께 부끄럽지 않도록, 최선을 다해 연구자의 길을 달려나가도록 하겠습니다. 감사합니다.

## List of Publications

### SCI publications (first or co-first author) [†: equal contribution]

1. Jaegeon Ryu†, Taesoo Bok†, **Se Hun Joo†**, Seokkeun Yoo, Gyujin Song, Su Hwan Kim, Sungho Choi, Hu Young Jeong, Min Gyu Kim, Seok Ju Kang, Chongmin Wang\*, Sang Kyu Kwak\*, and Soojin Park\*, "Electrochemical scissoring of disordered silicon-carbon composites for high-performance lithium storage"  
*Energy Storage Materials*, 36, 139-146, 2021
2. Yi Jiang†, Inseon Oh†, **Se Hun Joo†**, Yu-Seong Seo, Sun Hwa Lee, Won Kyung Seong, Yu Jin Kim, Jungseek Hwang\*, Sang Kyu Kwak\*, Jung-Woo Yoo\*, and Rodney S. Ruoff\*, "Synthesis of a Copper 1,3,5-Triamino-2,4,6-benzenetriol Metal–Organic Framework"  
*Journal of the American Chemical Society*, 142(43), 18346-18354, 2020  
[\[News broadcasting\]](#)
3. Yuju Jeon†, Sujin Kang†, **Se Hun Joo†**, Minjae Cho†, Sung O Park, Nian Liu\*, Sang Kyu Kwak\*, Hyun-Wook Lee\*, and Hyun-Kon Song\*, "Pyridinic-to-graphitic conformational change of nitrogen in graphitic carbon nitride by lithium coordination during lithium plating"  
*Energy Storage Materials*, 31, 505-514, 2020
4. Onur Buyukcakir\*†, Jaegeon Ryu†, **Se Hun Joo†**, Jieun Kang, Recep Yuksel, Jiyun Lee, Yi Jiang, Sungho Choi, Sun Hwa Lee, Sang Kyu Kwak\*, Soojin Park\*, and Rodney S. Ruoff\*, "Lithium Accommodation in a Redox-Active Covalent Triazine Framework for High Areal Capacity and Fast-Charging Lithium-Ion Batteries"  
*Advanced Functional Materials*, 30(36), 2003761, 2020
5. Yi Jiang†, Inseon Oh†, **Se Hun Joo†**, Onur Buyukcakir, Xiong Chen, Sun Hwa Lee, Ming Huang, Won Kyung Seong, Sang Kyu Kwak\*, Jung-Woo Yoo\* and Rodney S. Ruoff\*, "Partial Oxidation-Induced Electrical Conductivity and Paramagnetism in a Ni(II) Tetraaza[14]annulene-Linked Metal Organic Framework"  
*Journal of the American Chemical Society*, 141(42), 16884-16893, 2019  
[\[News broadcasting\]](#)
6. Jaehyun Park†, **Se Hun Joo†**, Yoon-Jeong Kim†, Ju Hyun Park, Sang Kyu Kwak\*, Seokhoon Ahn\*, and Seok Ju Kang\*, "Organic Semiconductor Cocystal for Highly Conductive Lithium Host Electrode"  
*Advanced Functional Materials*, 29(32), 1902888, 2019  
[\[News broadcasting\]](#)
7. Yi Jiang†, Inseon Oh†, **Se Hun Joo†**, Onur Buyukcakir, Xiong Chen, Sun Hwa Lee, Ming Huang, Won Kyung Seong, Jin Hoon Kim, Jan-Uwe Rohde, Sang Kyu Kwak\*, Jung-Woo Yoo\*, and Rodney S. Ruoff\*, "Organic Radical-Linked Covalent Triazine Framework with Paramagnetic Behavior"

*ACS Nano*, 13(5), 5251-5258, 2019

8. Min Su Kim†, Seongyeon Cho†, **Se Hun Joo**†, Junsang Lee, Sang Kyu Kwak\*, Moon Il Kim\*, and Jinwoo Lee\*, "N- and B-Codoped Graphene: A Strong Candidate To Replace Natural Peroxidase in Sensitive and Selective Bioassays"

*ACS Nano*, 13(4), 4312-4321, 2019

[\[News broadcasting\]](#)

9. Yoon-Gyo Cho†, Seo-Hyun Jung†, **Se Hun Joo**†, Yuju Jeon, Minsoo Kim, Kyung Min Lee, Seungmin Kim, Jong Mok Park, Hyun Kuk Noh, Young-Soo Kim, Jung-Eui Hong, Sang-Ik Jeon, Taewon Kim, Sang Kyu Kwak\*, Hoyoul Kong\*, and Hyun-Kon Song\*, "A metal-ion-chelating organogel electrolyte for Le Chatelier depression of Mn<sup>3+</sup> disproportionation of lithium manganese oxide spinel"

*Journal of Materials Chemistry A*, 6(45), 22483-22488, 2018

10. Jaehyun Park†, Cheol Woo Lee†, **Se Hun Joo**†, Ju Hyun Park, Chihyun Hwang, Hyun-Kon Song, Young Seok Park, Sang Kyu Kwak\*, Seokhoon Ahn\*, and Seok Ju Kang\*, "Contorted polycyclic aromatic hydrocarbon: promising Li insertion organic anode"

*Journal of Materials Chemistry A*, 6(26), 12589-12597, 2018

11. Joong-Kwon Kim†, Do Hyeong Kim†, **Se Hun Joo**†, Byeongwook Choi, Aming Cha, Kwang Min Kim, Tae-Hyuk Kwon, Sang Kyu Kwak\*, Seok Ju Kang\*, and Jungho Jin\*, "Hierarchical Chitin Fibers with Aligned Nanofibrillar Architectures: A Nonwoven-Mat Separator for Lithium Metal Batteries"

*ACS Nano*, 11(6), 6114-6121, 2017

12. Woo-Jin Song†, **Se Hun Joo**†, Do Hyeong Kim†, Chihyun Hwang, Gwan Yeong Jung, Sohyeon Bae, Yeonguk Son, Jaephil Cho, Hyun-Kon Song, Sang Kyu Kwak\*, Soojin Park\*, and Seok Ju Kang\*, "Significance of ferroelectric polarization in poly (vinylidene difluoride) binder for high-rate Li-ion diffusion"

*Nano Energy*, 32, 255-262, 2017

13. **Se Hun Joo**†, Ji Hye Seong†, Jin Sol Han†, Ju An Yang, and Sang Kyu Kwak\* "Study of Quaternary System of Salicylic Acid, Water, Ozone, and PAL by Molecular Dynamics"

*Fluid Phase Equilibria*, 388, 43-49, 2015

#### SCI publications (co-author)

14. Jaehyun Park†, Ju Hyun Park†, Minseok Yang†, **Se Hun Joo**, Sang Kyu Kwak\*, Seokhoon Ahn\*, and Seok Ju Kang\*, "Solid solution of semiconducting contorted small molecules for high-performance Li/Na-ion host electrodes"

*Energy Storage Materials*, 36, 123-131, 2021

15. Kijoo Eom†, Young-Eun Shin†, Joong-Kwon Kim†, **Se Hun Joo**, Kyungtae Kim, Sang Kyu Kwak, Hyunhyub Ko\*, Jungho Jin\*, and Seok Ju Kang\*, "Tailored Poly(vinylidene fluoride-co-trifluoroethylene) Crystal Orientation for a Triboelectric Nanogenerator through Epitaxial Growth on a Chitin Nanofiber Film"  
*Nano Letters*, 20(9), 6651-6659, 2020
16. Hyeokjung Lee†, Jinseong Lee†, **Se Hun Joo**, Seok Ju Kang, Sang Kyu Kwak, Seunggun Yu\*, and Cheolmin Park\*, "Dual Functionalization of Hexagonal Boron Nitride Nanosheets Using Pyrene-Tethered Poly(4-vinylpyridine) for Stable Dispersion and Facile Device Incorporation"  
*ACS Applied Nano Materials*, 3(8), 7633-7642, 2020
17. Jaeseong Hwang, Seungjun Myeong, Wooyoung Jin, Haeseong Jang, Gyutae Nam, Moonsu Yoon, Su Hwan Kim, **Se Hun Joo**, Sang Kyu Kwak\*, Min Gyu Kim\*, and Jaephil Cho\*, "Excess-Li Localization Triggers Chemical Irreversibility in Li- and Mn-Rich Layered Oxides"  
*Advanced Materials*, 32(34), 2001944, 2020
18. Dahye Baek†, Tae Kyung Lee†, Inkyu Jeon†, **Se Hun Joo**, Subeen Shin, Jaehyun Park, Seok Ju Kang\*, Sang Kyu Kwak\*, and Jiseok Lee\*, "Multi-Color Luminescence Transition of Upconversion Nanocrystals via Crystal Phase Control with SiO<sub>2</sub> for High Temperature Thermal Labels"  
*Advanced Science*, 7(11), 2000104, 2020
19. Won-Woo Park, Kyung Min Lee, Byeong Sung Lee, Young Jae Kim, **Se Hun Joo**, Sang Kyu Kwak\*, Tae Hyeon Yoo\*, and Oh-Hoon Kwon\*, "Hydrogen-Bond Free Energy of Local Biological Water"  
*Angewandte Chemie International Edition*, 132(18), 7155-7162, 2020  
[\[News broadcasting\]](#)
20. Pavel V. Bakharev\*, Ming Huang, Manav Saxena, Suk Woo Lee, **Se Hun Joo**, Sung O Park, Jichen Dong, Dulce Camacho-Mojica, Sunghwan Jin, Youngwoo Kwon, Mandakini Biswal, Feng Ding, Sang Kyu Kwak, Zonghoon Lee, and Rodney S. Ruoff\*, "Chemically induced transformation of chemical vapour deposition grown bilayer graphene into fluorinated single-layer diamond"  
*Nature Nanotechnology*, 15, 59-66, 2020  
[\[News broadcasting\]](#)
21. Yongjoon Cho†, Hae Rang Lee†, Ayoung Jeong, Jungho Lee, Sang Myeon Lee, **Se Hun Joo**, Sang Kyu Kwak, Joon Hak Oh\*, and Changduk Yang\*, "Understanding of Fluorination Dependence on Electron Mobility and Stability of Naphthalenediimide-Based Polymer Transistors in Environment with 100% Relative Humidity"  
*ACS Applied Materials & Interfaces*, 11(43), 40347-40357, 2019
22. Chihyun Hwang†, JongTae Yoo†, Gwan Yeong Jung†, **Se Hun Joo**, Jonghak Kim, Aming Cha, Jung-Gu Han, Nam-Soon Choi, Seok Ju Kang, Sang-Young Lee, Sang Kyu Kwak\*, and Hyun-

- Kon Song\*, "Biomimetic Superoxide Disproportionation Catalyst for Anti-Aging Lithium–Oxygen Batteries"  
*ACS Nano*, 13(8), 9190-9197, 2019  
[\[News broadcasting\]](#)
23. Sanghan Lee†, Wooyoung Jin†, Su Hwan Kim†, **Se Hun Joo**, Gyutae Nam, Pilgun Oh, Young-Ki Kim, Sang Kyu Kwak\*, and Jaephil Cho\*, "Oxygen Vacancy Diffusion and Condensation in Lithium-Ion Battery Cathode Materials"  
*Angewandte Chemie International Edition*, 58(31), 10478-10485, 2019  
[\[VIP paper\]](#)
24. Hemin Zhang, Sung O Park, **Se Hun Joo**, Jin Hyun Kim, Sang Kyu Kwak\*, and Jae Sung Lee\* "Precisely-controlled, a few layers of iron titanate inverse opal structure for enhanced photoelectrochemical water splitting"  
*Nano Energy*, 62, 20-29, 2019
25. Eunhye Shin, **Se Hun Joo**, Min Sun Yeom,\* and Sang Kyu Kwak\*, "Theoretical study on the stability of insulin within poly-isobutyl cyanoacrylate (PIBCA) nanocapsule"  
*Molecular Simulation*, 45(11), 896-903, 2019
26. Yunfei Bu, Haeseong Jang, Ohhun Gwon, Su Hwan Kim, **Se Hun Joo**, Gyutae Nam, Seona Kim, Yong Qin, Qin Zhong, Sang Kyu Kwak\*, Jaephil Cho\*, and Guntae Kim\*, "Synergistic interaction of perovskite oxides and N-doped graphene in versatile electrocatalyst"  
*Journal of Materials Chemistry A*, 7(5), 2048-2054, 2019  
[\[Back Cover\]](#)
27. Taehyung Kim†, Byeongho Park†, Kyung Min Lee, **Se Hun Joo**, Min Seok Kang, Won Cheol Yoo, Sang Kyu Kwak\*, and Byeong-Su Kim\*, "Hydrothermal Synthesis of Composition- and Morphology-Tunable Polyimide-Based Microparticles"  
*ACS Macro Letters*, 7(12), 1480-1485, 2018
28. Jaehyun Park†, Cheol Woo Lee†, Ju Hyun Park†, **Se Hun Joo**, Sang Kyu Kwak\*, Seokhoon Ahn\*, and Seok Ju Kang\*, "Capacitive Organic Anode Based on Fluorinated-Contorted Hexabenzocoronene: Applicable to Lithium-Ion and Sodium-Ion Storage Cells"  
*Advanced Science*, 5(12), 1801365, 2018  
[\[News broadcasting\]](#)
29. Yun-Tae Kim, **Se Hun Joo**, Hyegi Min, Jiyun Lee, Seung Min Moon, Mirang Byeon, Tae Eun Hong, Michael S. Strano, Jae-Hee Han, Sang Kyu Kwak\*, and Chang Young Lee\*, "The Exterior of Single-Walled Carbon Nanotubes as a Millimeter-Long Cation-Preferring Nanochannel"  
*Chemistry of Materials*, 30(15), 5184-5193, 2018
30. Kyungtae Kim†, Minjeong Ha†, Byeongwook Choi†, **Se Hun Joo**, Han Sol Kang, Ju Hyun



- Park, Bongjun Gu, Chanho Park, Cheolmin Park, Jongbok Kim, Sang Kyu Kwak, Hyunhyub Ko\*, Jungho Jin\*, and Seok Ju Kang\*, "Biodegradable, electro-active chitin nanofiber films for flexible piezoelectric transducers"  
*Nano Energy*, 48, 275-283, 2018
31. Yi Jiang, Gyeong Hee Ryu, **Se Hun Joo**, Xiong Chen, Sun Hwa Lee, Xianjue Chen, Ming Huang, Xiaozhong Wu, Da Luo, Yuan Huang, Jeong Hyeon Lee, Bin Wang, Xu Zhang, Sang Kyu Kwak, Zonghoon Lee, and Rodney S. Ruoff\*, "Porous Two-Dimensional Monolayer Metal–Organic Framework Material and Its Use for the Size-Selective Separation of Nanoparticles"  
*ACS Applied Materials & Interfaces*, 9(33), 28107-28116, 2017
32. Ye Chan Kim†, Dong Hyup Kim†, **Se Hun Joo**, Na Kyung Kwon, Tae Joo Shin, Richard A. Register, Sang Kyu Kwak, and So Youn Kim\*, "Log-Rolling Block Copolymer Cylinders"  
*Macromolecules*, 50(9), 3607–3616, 2017
33. Dong-Gyu Lee, Su Hwan Kim, **Se Hun Joo**, Ho-Il Ji, Hadi Tavassol, Yuju Jeon, Sihyuk Choi, Myeong-Hee Lee, Chanseok Kim, Sang Kyu Kwak, Guntae Kim, and Hyun-Kon Song\*, "Polypyrrole-assisted oxygen electrocatalysis on perovskite oxides"  
*Energy & Environmental Science*, 10(2), 523-527, 2017
34. Robert Francis Niescier†, Sang Kyu Kwak†, **Se Hun Joo**, Karen Chang, and Kyung-Tai Min\*, "Dynamics of Mitochondrial Transport in Axons"  
*Frontiers in Cellular Neuroscience*, 10:123, 2016
35. Hyejung Kim†, Sanghan Lee†, Hyeon Cho, Junhyeok Kim, Jieun Lee, **Se Hun Joo**, Su Hwan Kim, Minjoon Park, Sang Kyu Kwak\*, and Jaephil Cho\*, "Enhancing Interfacial Bonding between Anisotropically Oriented Grains Using a Glue-Nanofiller for Advanced Li-Ion Battery Cathode"  
*Advanced Materials*, 28(23), 4705-4712, 2016  
[\[Front Cover\]](#)
36. Kang Lib Kim; Wonho Lee, Sun Kak Hwang, **Se Hun Joo**, Suk Man Cho, Giyoung Song, Sung Hwan Cho, Beomjin Jeong, Ihn Hwang, Jong-Hyun Ahn, Young-Jun Yu, Tae Joo Shin, Sang Kyu Kwak, Seok Ju Kang, Cheolmin Park, "Epitaxial Growth of Thin Ferroelectric Polymer Films on Graphene Layer for Fully Transparent and Flexible Nonvolatile Memory"  
*Nano Letters*, 16(1), 334-340, 2016
37. Chihyun Hwang, **Se Hun Joo**, Na-Ri Kang, Ungju Lee, Tae-Hee Kim, Yuju Jeon, Jieun Kim, Young-Jin Kim, Ju-Young Kim\*, Sang Kyu Kwak\*, and Hyun-Kon Song\*, "Breathing silicon anodes for durable high-power operations"  
*Scientific Reports*, 5:14433, 2015

